

## Micro and Macro Finite Element Analyses of Fretting Fatigue

Qingming Deng

Doctoral dissertation submitted to obtain the academic degree of  
Doctor of Electromechanical Engineering

### Supervisors

Prof. Magd Abdel Wahab, PhD\* - Prof. Xiaochun Yin, PhD\*\*

\* Department of Electromechanical, Systems and Metal Engineering  
Faculty of Engineering and Architecture, Ghent University

\*\* Department of Mechanics  
College of Science, Nanjing University of Science and Technology, China

July 2021





## Micro and Macro Finite Element Analyses of Fretting Fatigue

**Qingming Deng**

Doctoral dissertation submitted to obtain the academic degree of  
Doctor of Electromechanical Engineering

### Supervisors

Prof. Magd Abdel Wahab, PhD\* - Prof. Xiaochun Yin, PhD\*\*

\* Department of Electromechanical, Systems and Metal Engineering  
Faculty of Engineering and Architecture, Ghent University

\*\* Department of Mechanics

College of Science, Nanjing University of Science and Technology, China

July 2021



ISBN 978-94-6355-503-6

NUR 978

Wettelijk depot: D/2021/10.500/51

## **Members of the Examination Board**

### **Chair**

Prof. Patrick De Baets, PhD, Ghent University

### **Other members entitled to vote**

Samir Khatir, PhD, Ghent University

Gregor Kosec, PhD, Institut "Jožef Stefan", Slovenia

Kyvia de Fatima Resende Pereira, PhD, Vanderbilt University, USA

Tongyan Yue, PhD, State Grid Xinyuan, China

Qi Zhao, PhD, Ghent University

### **Supervisors**

Prof. Magd Abdel Wahab, PhD, Ghent University

Prof. Xiaochun Yin, PhD, Nanjing University of Science and Technology, China



# Declaration

I hereby declare that except where specific reference is made to the work of others, the contents of this dissertation are original and have not been submitted in whole or in part for consideration for any other degree or qualification in this, or any other University. This dissertation is the result of my own work and includes nothing which is the outcome of work done in collaboration, except where specifically indicated in the text. This dissertation contains less than 65,000 words including appendices, bibliography, footnotes, tables and equations and has less than 150 figures.

Qingming Deng

2021

# Acknowledgements

Firstly, I would like to express my immense gratitude to my supervisor, prof. dr. ir. Magd Abdel Wahab, for giving me the chance to study in Soete Laboratory and work on a very interesting research topic. His professional and patient guidance helped me finish my PhD research. I gratefully acknowledge the opportunities to exchange at international conferences, it gradually clarifies my research focus and direction. These precious experiences will affect the rest of my life. I am also thankful to Professor Xiaochun Yin in China for supporting me a lot during the research. At the beginning of my doctoral program, he helped me establish a good habit of scientific research and gave me a lot of space and encouragement during my study. Thanks to the examination committee members who reviewed my thesis and gave their respected suggestions to improve the thesis.

I would also like to thank my colleagues from UGent for all their support throughout my PhD. The good academic atmosphere of the Finite Element Research Group and the intense discussions during the group meeting provided me with a platform to share and enhance my knowledge. And often inspired me to generate new ideas. Special thanks to Nadeem Ali Bhatti and Kyvia de Fatima Resende Pereira for all helping with my research when I start study at UGent. In addition to academic discussion, colleagues are also my friends who have always been there to

share good and bad moments in my life in Belgium. This made me feel warm outside my home country.

Also, thanks for all support from the Laboratory Soete staff and professors. All professors are very happy to share their knowledge and insights with us. Their rigorous and serious scientific research attitude has also set a good example for us. Also, thanks to Georgette D'Hondt for your patient care and help. This is a really big assistance for me and makes me feel a great warmth. I'd like to also thank Jie Zhang and Kaveh Samadian for helping in informal discussions. Many thanks to Laboratory Soete for creating such a nice environment to share our different cultures and knowledge.

I would like to thank the China scholarship council and Nanjing University of Science and Technology to provide scholarship for my PhD degree. Thanks to the masks and medicines provided to us during the Covid-19 epidemic.

As a personal note, special thanks to my parents and younger sister, and all my family, for their faithful support and encouragement that support me to overcome all difficulties. Also, thanks to my friends for sharing different lives with me, allowing me to constantly adjust myself in reference to the outside world, so as to gradually understand the meaning of my own life.

Qingming Deng

2021

# Summary

Contact problems are common in industrial applications. The fretting phenomenon occurs when two objects are in contact with each other and have small amplitude relative motion. If fretting occurs in contact fatigue, the service life of components will be greatly reduced. Compared with ordinary tensile fatigue, the stress concentration at the contact edge in fretting fatigue brings great difficulty to the prediction of fatigue life. Especially, the stress distribution caused by the microstructure and macrostructure of the components has a great influence on the fretting fatigue response. When there are inclusions or micro voids in the components, the stress distribution is more complex. The contact surface geometry and the crack capture technique (the stop hole) also affect the total fatigue life. The main purpose of this thesis is to study the influence of several kinds of micro and macro structure of the component on fretting fatigue by numerical methods.

Inclusions are common in alloy materials. In some composite materials, inclusions are also used to improve the overall performance of the material. Using the representative volume element (RVE) technique, the equivalent macroscopic properties of materials with random inclusions with different parameters can be obtained. Then, combined with the finite element technology, the fretting fatigue problem of different types, volume ratios and shape inclusions in the specimen, is simulated. It shows

that the existence of inclusions may cause the peak stress to transfer from the contact surface to the interior of the specimen. The size and the distance from the surface of the inclusion have a more significant effect on the surface stress distribution than the type and shape of inclusion.

Compared with inclusions, porosity in the specimen is a more dangerous defect. Also, because of the randomness of defects, the fatigue life of components is unstable and difficult to predict. And when the micro-voids size in the material exceeds a critical value, the crack mainly originates near the micro-voids. In this thesis, the critical plane method and the critical distance method (TCD) are used to analyse the case of the specimen containing a single critical void with different parameters. Because of stress concentration, the damage parameters decrease rapidly along the depth direction. Three kinds of critical plane parameters used to predict fatigue lifetime and the TCD method is adopted to consider the stress gradient. The prediction obtained by the combination of these two methods has a good agreement with experiment results. In this thesis, the effect of a critical micro void with different positions and sizes on the fatigue crack initiation life is discussed. The results show that the existence of material heterogeneity (critical micro void) has a great influence on the distribution of damage parameters below the contact surface. However, only when the critical void is close to the contact edge, the crack initiation position will shift. Then, when the critical micro-void is located in a region similar to a half-butterfly wing, the crack initiation life will be reduced compared with the homogeneous case. If it is located

at the below left side (under the surface) or on the right side (near the surface) of the contact edge, the life will increase.

The main cause of fretting fatigue is the high stress at the contact edge. In addition to the internal structure of the specimen, the treatment of the contact surface geometry can also effectively change the stress distribution and amplitude in the contact area. Adding a cylindrical pit on the specimen surface can increase the contact radius between pad and specimen. Therefore, the contact stress is dispersed and the peak stress is reduced. However, the relative sliding range between the contact surfaces increases. Thus, the critical plane parameter is used to predict the crack initiation life. Although three different critical plane parameters are used, they are all based on stress, strain or strain energy. The Ruiz parameter is used to consider the effect of relative sliding amplitude. The peak value of the critical plane parameter can be much lower than that of the flat specimen by using the appropriate pit radius. Furthermore, the peak value of Ruiz parameter is also lower. All parameters give a similar prediction of the crack initiation position.

By influencing the stress distribution in the contact area, the crack initiation life can be increased or decreased. In engineering applications, crack initiation is often too late to be detected. Therefore, crack arrest technology for crack propagation stage is widely studied and used. One of the most common and easy to implement method is stop hole technology, which is based on drilling a hole at the crack tip. This can effectively reduce the stress concentration at the crack tip and make the propagating

crack produce a second crack initiation at the lower edge of hole. The conventional FE method with remeshing technique is used to obtain the stress intensity factors (SIF) at the crack tip. The linear elastic fracture mechanics (LEFM) approach, which is based on the combination between Paris' law and J-integral method, can normally be applied to predict the crack propagation life. The maximum  $\Delta K_I^*(\theta)$  criteria is used to predict the crack growth orientation. For the second crack initiation prediction, the critical plane parameter and variable length TCD method are used together. The correctness of crack propagation path and lifetime prediction is verified by fretting fatigue experiment. Then, the applicability of the code to the prediction of the second crack initiation life is verified by a central crack tensile fatigue experiment considering the stop hole. Finally, the influence of different stop holes on the propagation life of fretting fatigue crack is discussed in this thesis. It is found that the stop hole changes the propagation path and initiation starts again from the lower edge of hole. The increase of propagation life mainly comes from the second crack initiation. The increased crack propagation lifetime can be twice as long as that of the homogeneous case.

The main contribution of this thesis is to deeply consider the influence of different macro and micro structure of specimen on fretting fatigue response. The results show that the distribution of stress and strain in the specimen will be changed obviously by micro defects, surface geometry and stop hole. The combination of critical plane parameters and critical distance method can effectively predict the crack initiation life. Proper

design of a structure can not only avoid the decrease of fatigue life but also effectively prolong the fatigue life.

# Samenvatting

Contact problemen komen vaak voor in industriële toepassingen. Het fenomeen van fretting treedt op wanneer twee objecten met elkaar in contact komen en een relatieve beweging met een kleine amplitude hebben. In het geval van fretting vermoeiing treedt er wrijving op, en verkort de levensduur van de componenten aanzienlijk. Vergeleken met gewone trekvermoeiing, levert de spanningsconcentratie aan de contactrand bij fretting vermoeiing grote moeilijkheden op bij het voorspellen van de vermoeiing levensduur. Vooral de door de micro- en macrostructuur veroorzaakte spanningsverdeling van de componenten heeft een grote invloed op fretting vermoeiing. Wanneer er inclusies of microholtes in de componenten zijn, is de spanningsverdeling complexer. De geometrie van het contactoppervlak en de scheuropvangtechniek (de stop-holte) hebben ook een effect op de totale vermoeiing levensduur. Het belangrijkste doel van dit proefschrift is om door middel van numerieke methoden de invloed van verschillende soorten micro- en macrostructuren van de component op fretting vermoeiing te bestuderen.

Inclusies komen vaak voor in legeringsmaterialen. In sommige composietmaterialen worden inclusies ook gebruikt om de algemene prestaties van het materiaal te verbeteren. Met behulp van de representatieve volume-elementtechniek (RVE) kunnen de equivalente

macroscopische eigenschappen van materialen met willekeurige inclusies met verschillende parameters worden verkregen. Vervolgens wordt in combinatie met de finiete-elemententechnologie het probleem van fretting vermoeiing gesimuleerd bij verschillende types, volumeverhoudingen en vorminclusies in het exemplaar. Dit toont aan dat het bestaan van inclusies ertoe kan leiden dat de piekspanning wordt overgedragen van het contactoppervlak naar de binnenkant van het exemplaar. De grootte en de afstand tot het oppervlak van de insluiting hebben een groter effect op de verdeling van de oppervlaktetenspanning dan het type en de vorm van de insluiting.

In vergelijking met inclusies is poreusheid in het exemplaar een gevaarlijker defect. Vanwege de willekeurigheid van de defecten is de vermoeiing levensduur van componenten onstabiel en moeilijk te voorspellen. Wanneer de grootte van de microholtes in het materiaal een kritische waarde overschrijdt, ontstaat de scheur bovendien voornamelijk nabij de microholtes. In dit proefschrift worden de kritische vlakmethode en de kritische afstandsmethode (TCD) gebruikt om een exemplaar te analyseren dat een enkele kritische holte bevat met verschillende parameters. Vanwege de spanningsconcentratie nemen de schadeparameters snel af in de diepterichting. Drie soorten kritische vlakparameters die worden gebruikt om de vermoeiing levensduur te voorspellen en de TCD-methode wordt gebruikt om de spanningsgradiënt te bekijken. De voorspelling vanuit de combinatie van deze twee methoden komt goed overeen met de experimentresultaten.

Dit proefschrift bespreekt het effect van kritische microholtes met verschillende posities en afmetingen op de vermoeiingsscheurinitiatie. De resultaten laten zien dat materiaalheterogeniteit (d.i. kritische microholtes) een grote invloed heeft op de verdeling van schadeparameters onder het contactoppervlak. Alleen wanneer de kritische holte zich dicht bij de contactrand bevindt, zal de positie van de scheurinitiatie verschuiven. Wanneer de kritische microholte zich dan in een gebied bevindt dat vergelijkbaar is met een halve vliedervleugel, zal de levensduur van de scheurinitiatie verkorten in vergelijking met het homogene geval. Als deze zich aan de linkerkant (d.i. onder het oppervlak) of aan de rechterkant (d.i. nabij het oppervlak) van de contactrand bevindt, zal de levensduur toenemen.

De belangrijkste oorzaak van fretting vermoeiing is de hoge spanning aan de contactrand. Naast de interne structuur van het exemplaar, kan de behandeling van de contactoppervlakgeometrie ook effectief de spanningsverdeling en amplitude in het contactgebied veranderen. Het toevoegen van een cilindrische pit op het exemplaaroppervlak kan de contactradius tussen de ondergrond en het exemplaar vergroten. Daarom wordt de contactspanning verspreid en de piekspanning verminderd. Het relatieve glijbereik tussen de contactvlakken neemt echter toe. De kritische vlakparameter wordt dus gebruikt om de levensduur van de scheurinitiatie te voorspellen. Hoewel er drie verschillende kritische vlakparameters worden gebruikt, zijn ze allemaal gebaseerd op spanning-, rek- of vervormingsenergie. De Ruiz-parameter wordt

gebruikt om het effect van relatieve glijdende amplitude te overwegen. De piekwaarde van de kritische vlakparameter kan veel lager zijn dan die van het vlakke exemplaar door de juiste pitstraal te gebruiken. Bovendien is de piekwaarde van de Ruiz-parameter ook lager. Alle parameters geven een vergelijkbare voorspelling van de positie van de scheurinitiatie.

Door de spanningsverdeling in het contactgebied te beïnvloeden, kan de levensduur van scheurinitiatie worden verlengd of verkort. Bij technische toepassingen is het vaak te laat om de scheurinitiatie te detecteren. Daarom wordt scheurstoptechnologie voor de scheurpropagatiefase op grote schaal bestudeerd en gebruikt. Een van de meest gebruikelijke en eenvoudig te implementeren methoden is de stop-holte-technologie, of het boren van een holte aan de scheurtip. Dit kan de spanningsconcentratie aan de scheurtip effectief verminderen en ervoor zorgen dat de zich voortplantende scheur een tweede scheurinitiatie veroorzaakt aan de onderrand van de holte. De conventionele FE-methode met remeshing-techniek wordt gebruikt om de spanningsintensiteitsfactor (SIF) te verkrijgen aan de scheurtip. De lineaire elastische breukmechanicabepaling (LEFM), die is gebaseerd op een combinatie tussen de Parisformule en de J-integraalmethode, kan worden toegepast om de scheurpropagatielevensduur te voorspellen. De maximale  $\Delta K_I^*(\theta)$ -criteria worden gebruikt om de oriëntatie van de scheurpropagatie te voorspellen. Voor de voorspelling van de tweede scheurinitiatie worden de kritische vlakparameter en de TCD-methode met variabele lengte gebruikt. Het correcte scheurpropagatietraject en de

voorspelling van de levensduur worden geverifieerd door een experiment met fretting vermoeiing. Vervolgens wordt de toepasbaarheid van de code op de voorspelling van de levensduur van de tweede scheurinitiatie geverifieerd door een centraal scheur-trekvermoeiingsexperiment waarbij rekening wordt gehouden met de stop-holte. Ten slotte wordt in dit proefschrift de invloed van verschillende stop-holtes op de fretting vermoeiing scheurpropagatielevensduur besproken. De conclusie is dat de stop-holte het scheurpropagatietraject verandert en de initiatie opnieuw begint aan de onderkant van de holte. De verlenging van de scheurpropagatielevensduur komt voornamelijk doordat de tweede scheur begint. De verlengde scheurpropagatielevensduur kan twee keer zo lang zijn als in het geval van de homogene casus.

De belangrijkste bijdrage van dit proefschrift is het diepgaand onderzoeken van de invloed van het verschil tussen macro- en microstructuur van fretting vermoeiing. De resultaten tonen dat de distributie van spanning en rek in het exemplaar duidelijk zal worden veranderd door microdefecten, oppervlakgeometrie en stopholtes. De combinatie van kritische vlakparameters en de kritische afstandsmethode kan effectief de scheurinitiatielevensduur voorspellen. Het correcte ontwerp van een constructie kan niet alleen de afname van de levensduur door vermoeiing voorkomen, maar ook de vermoeiing levensduur verlengen.



# Contents

Declaration.....	i
Acknowledgements .....	ii
Summary .....	iv
Contents .....	xv
List of Figures .....	xix
List of Tables .....	xxvi
Nomenclature.....	xxvii
Chapter 1    Introduction .....	1
1.1    Fretting fatigue.....	2
1.2    Objectives .....	5
1.3    Outline .....	8
Chapter 2    Theoretical background .....	12
2.1    Contact mechanics.....	12
2.1.1    Normal line contact .....	13
2.1.2    Line contact under partial slip.....	16
2.2    Micro- and macro-structure .....	22
2.2.1    Micro inclusion and voids.....	23

2.2.2	Surface pit treatment and stop hole .....	26
2.3	Fretting fatigue and numerical methods .....	30
2.3.1	Introduction .....	30
2.3.2	Finite element analysis.....	33
2.3.3	Crack initiation .....	36
2.3.4	Crack propagation .....	51
2.4	Summary.....	64
Chapter 3	Randomly distributed inclusions.....	66
3.1	Finite Element Model and Validation.....	67
3.2	Completely randomly distributed inclusion.....	78
3.2.1	Stress peak and its position.....	78
3.2.2	Stress peak position characteristic.....	82
3.3	Randomly distributed and manually placed inclusions.....	85
3.3.1	Effect of distance from surface .....	87
3.3.2	Effect of inclusion size.....	89
3.3.3	Effect of inclusion shape .....	90
3.4	Summary.....	91
Chapter 4	The effect of critical micro-void on the crack initiation .....	93
4.1	Experiment data .....	94
4.2	Multiscale numerical model.....	95

4.2.1	Representative volume element (RVE).....	96
4.2.2	Macro-scale finite element model .....	97
4.3	Results and discussion .....	100
4.3.1	Validation of the homogeneous model .....	102
4.3.2	Effect of critical micro-void location.....	113
4.3.3	Effect of micro-void size .....	127
4.4	Summary.....	130
Chapter 5	Fretting fatigue with pit treatment surface .....	133
5.1	Numerical Model.....	134
5.2	Experimental Validation .....	139
5.3	Results and Discussion.....	140
5.3.1	Stress Distribution in the Three Models.....	141
5.3.2	Critical Plane Parameter.....	145
5.3.3	Discussion.....	148
5.4	Summary.....	150
Chapter 6	The effect of stop hole .....	152
6.1	Numerical model and Experimental validation .....	153
6.1.1	Propagation path.....	155
6.1.2	Fatigue lifetime prediction.....	156
6.2	Results and discussion .....	164

6.2.1	Effect of drilling location .....	165
6.2.2	Effect of stop hole size.....	168
6.3	Summary.....	171
Chapter 7	Conclusion and Outlook.....	173
7.1	Conclusion.....	173
7.2	Outlook.....	176
Appendix	.....	179
References	.....	180

# List of Figures

Figure 2.1. Normal line contact with only a normal force. ....	14
Figure 2.2. An example of normal stress distribution of the contact surface. .....	16
Figure 2.3. An example of line contact under partial slip with a tangential loading $Q$ .....	17
Figure 2.4. An example of the shear stress distribution for normal and tangential loads case. ....	19
Figure 2.5. Fretting fatigue contact. ....	20
Figure 2.6. Shear stress distribution at the contact interface.....	21
Figure 2.7. An example of surface cylindrical pit treatment contact. ....	28
Figure 2.8. Three kinds of stop hole. ....	29
Figure 2.9. The influence of relative sliding displacement on fretting wear and fretting fatigue [23]. ....	31
Figure 2.10. Fretting fatigue crack initiation and propagation process...	33
Figure 2.11. Schematic of RVE method.....	35
Figure 2.12. A partition diagram of the specimen with two areas. ....	36
Figure 2.13. The main crack orientation defined by the angle between crack and the axis perpendicular to specimen surface. ....	38

Figure 2.14. Total life estimated according to the initiation length [113].  
.....39

Figure 2.15. Schematic diagram of three critical distance methods. ....47

Figure 2.16. Flowchart of fatigue life prediction based on variable critical distance and FP parameter Susmel and Taylor [165].....50

Figure 2.17. Three modes for crack growth. ....53

Figure 2.18. A typical plot of crack growth rate change with the stress intensity range. ....54

Figure 2.19. The prediction of the crack growth orientation according to the SIFs.....57

Figure 2.20. The stress near the crack tip in polar coordinates.....59

Figure 2.21. The stress intensity factor of branch cracks.....60

Figure 2.22. The flowchart of fatigue crack growth analysis based on fracture mechanics.....63

Figure 3.1. Schematic view of fretting fatigue experimental setup [25]..68

Figure 3.2. Configuration of the fretting fatigue numerical model.....68

Figure 3.3. Four difference size RVEs and corresponding mesh models.  
.....71

Figure 3.4. Convergence of (a) Macro elastic modulus and (b) Poisson's ratio.....72

Figure 3.6. Finite element model of case 3 with artificially placed four inclusions.....75

Figure 3.5. (a) Mesh sensitivity diagram (effect of mesh refinement on shear stress distribution on contact interface), (b) Shear stress distribution near contact interface for a homogenous case with 2 $\mu$ m contact element size. ....77

Figure 3.7. Element size convergence of inclusions. ....78

Figure 3.8. Stress distribution of Case 3 below the contact surface (a) Mises stress (b) Tensile stress and (c) Shear stress. ....80

Figure 3.9. (a) Comparison of stress peaks between heterogeneous materials and homogenous materials and their (b) location of all cases 80

Figure 3.10. The local inclusion alignment of the shear stress peak of (a) case 3 and (b) case 4. ....83

Figure 3.11. Stress distribution of Case 5 below the contact surface (a) Mises stress (b) Tensile stress and (c) Shear stress. ....84

Figure 3.12. (a) Mises stress (b) Tensile stress (c) Normal stress (d) Shear stress distribution on the contact surface for different inclusion materials cases. ....86

Figure 3.13. (a) Mises stress (b) Tensile stress (c) Normal stress (d) Shear stress distribution on the contact surface for different distance cases....88

Figure 3.14. (a) Mises stress (b) Tensile stress (c) Normal stress (d) Shear stress distribution on the contact surface for different inclusion size cases .....89

Figure 3.15.(a) Mises stress (b) Tensile stress (c) Normal stress (d) Shear stress distribution on the contact surface for different inclusion shape cases..... 90

Figure 4.1. The RVE units with three different defect aspect ratios (a) 1, (b) 1.84 and (c) 2.68 with a random distribution of defect size and position..... 97

Figure 4.2. Numerical model configuration of the fretting fatigue..... 98

Figure 4.3. Entire cycle load for test 1 ..... 99

Figure 4.4. (a) Stress distribution at contact surface for maximum load step, (b) Stress distribution at contact surface for minimum load step and (c) dimensionless critical plane parameter distribution at contact surface – Test 1..... 104

Figure 4.5. (a) FP, (b) FS and (c) SWT parameters distribution at contact surface for test 1. .... 105

Figure 4.6. Comparison between prediction and experimental failure life using (a) hot spot method and (b) area average method. .... 108

Figure 4.7. Flow chart for calculation of damage parameters and crack initiation location ..... 109

Figure 4.8. Variation of dimensionless parameter with angle at peak point. .... 110

Figure 4.9. Quadrant method diagram (a) Peak point on the contact surface and (b) Peak point on the void. .... 111

Figure 4.10. (a) FP, (b) FS and (c) SWT parameters distribution for the case with a critical micro-void locate at  $x = 0.4$  mm,  $y = -0.1$  mm. 114

Figure 4.11. The prediction of peak point coordinates of (a) FP, (b) FS and (c) SWT parameters for all cases. .... 116

Figure 4.12. FS parameter distribution of the case with a critical micro-void locate at  $x = 0.4$  mm,  $y = -0.05$  mm..... 117

Figure 4.13. The prediction of critical plane of (a) FP, (b) FS and (c) SWT parameter for all cases..... 119

Figure 4.14. The predicted dimensionless crack initiation life for all cases by (a) FP, (b) FS and (c) SWT parameters..... 121

Figure 4.15. The effect of micro-void location on crack initiation lifetime (2D cloud map)..... 124

Figure 4.16. The comparison between the prediction initiation life of heterogeneous specimen and experimental result: (a) FP, (b) FS and (c) SWT criterion..... 126

Figure 4.17. The prediction of peak point coordinates of (a) FP, (b) FS, (c) SWT parameter for all cases with different micro-void size..... 128

Figure 4.18. The prediction of dimensionless crack initiation life of (a) FP, (b) FS and (c) SWT parameter for all cases with different micro-void size. .... 129

Figure 5.1. The theoretical contact radius change with the pit radius .. 136

Figure 5.2. Pit radius and position..... 137

Figure 5.2. The theoretical normal stress of the contact surface for types 1, 2 and 3..... 138

Figure 5.3. Finite element model of type 2 (pit-specimen) ..... 139

Figure 5.4. The Mises stress distribution in the whole model when peak loading (a) type 1, (b) type 2 and (c) type 3 ..... 142

Figure 5.5. Contact surface stress distribution comparison between each model: (a) tensile stress and (b) shear stress..... 143

Figure 5.6. Dimensionless critical plane parameter distribution along the contact surface: (a) type 1 and (b) type 2 (c) type 3 ..... 146

Figure 5.7. Slip range along the contact surface of both models: (a) type 1, (b) type 2 and (c) type 3..... 148

Figure 5.8. Ruiz F2 parameter along the contact surface..... 150

Figure 6.1. The process of drilling a stop hole and crack growth ..... 153

Figure 6.2. Crack propagation FE model ..... 154

Figure 6.3. Crack propagation path of test 1 (a) experiment observation[45] and (b) prediction by our framework. .... 156

Figure 6.4. Variation of crack length with prediction crack propagation lifetime of Test 1 – Test 9 ..... 158

Figure 6.5. Comparison between the predicted and measured total life. .... 159

Figure 6.6. The FS parameter gradient along the critical plane. .... 160

Figure 6.7. The relationship between TCD and initiation lifetime for Test 1 - Test 9.....161

Figure 6.8. Comparison between the predicted and measured total life. ....162

Figure 6.9. Configuration of crack growth test specimen [52]. .....163

Figure 6.10. Comparison between the predicted and the experimental fatigue life for CCT case 1. ....164

Figure 6.11. A stop hole with radius  $r = 0.16$  mm is added on the crack tip when the crack length  $l = 0.30$  mm. ....165

Figure 6.12. The effect of drilling location of stop hole on the crack propagation path.....166

Figure 6.13. The effect of drilling location of stop hole on the crack propagation lifetime.....167

Figure 6.14. The effect of drilling location of stop hole on the second crack initiation lifetime .....168

Figure 6.15. The effect of hole size on the crack propagation path. ....169

Figure 6.16. The effect of hole size of stop hole on the crack propagation lifetime. ....170

Figure 6.17. The effect of hole size on the second crack initiation.....171

# List of Tables

Table 3.1. The original material properties involved in this paper. ....	70
Table 3.2. All the cases involved in this study. ....	73
Table 4.1. The fretting fatigue experiments load condition and life results [25]. ....	95
Table 4.2. The property of all materials and defect characteristics.....	95
Table 4.3. The fatigue material parameters for aluminum alloy 2024-T3 [152, 154].....	101
Table 4.4. Fretting fatigue experimental results of critical plane direction from literature.....	106
Table 4.5. Predicted peak position (abscissa) and critical plane angle for all test.....	112
Table 4.6. The general range of peak position and the detail of the special case (peak shift) of three kinds of prediction.....	118
Table 4.7. The general range of critical plane angle and the detail of the special case (critical plane shift) of three kinds of prediction. ....	119
Table 5.1: The chemical composition of the Al2024-T3 [45].....	139
Table 5.2: Detail results of the maximum critical plane parameter .....	146

# Nomenclature

## Symbols

$a$	Semi-contact width
$b$	Fatigue strength exponent in tension
$b'$	Fatigue strength exponent in torsion
$c$	Fatigue ductility exponent in tension
$c'$	Fatigue ductility exponent in torsion
$C$	Constant factor of Paris' law
$dl$	Crack length increment
$dN$	Propagation life increment
$d_x$	Slip value
$E$	Elastic modulus
$E^*$	Equivalent elastic modulus
$F$	Normal load
$F_1$	Wear parameter
$F_2$	Initiation parameter
$G$	Shear elastic modulus
$K$	Stress intensity factor
$K_{Ic}$	Plane strain fracture toughness
$K_I^*$	Mode I stress intensity factor of branch crack
$K_{II}^*$	Mode II stress intensity factor of branch crack
$\Delta K$	Stress intensity factor range
$\Delta K_{cr}$	Fracture toughness stress intensity factor range
$\Delta K_{th}$	Long crack threshold stress intensity factor range

$\Delta K_{eff}$	Equivalent stress intensity factor range
$\Delta K_I$	Mode I (opening) stress intensity range
$\Delta K_{II}$	Mode II (sliding) stress intensity range
$l$	Crack length
$l_c$	Critical crack length
$m$	An exponent of Paris' law
$N_f$	Total fatigue life,
$N_i$	Initiation life
$N_{i2}$	Second initiation life
$N_{is}$	Predicted initiation life at $P_s$
$N_{iv}$	Predicted initiation life at $P_v$
$N_p$	Propagation life
$N_{p1}$	First stage propagation life
$N_{p2}$	Second stage propagation life
$p(x)$	Normal stress
$p_{max}$	Peak normal stress
$P_s$	Peak point of contact surface
$P_v$	Peak point of edge of micro-void
$Q$	Tangential force
$q(x)$	Shear stress
$r$	Stop hole radius
$R$	Curvature radius
$R_{pad}$	Pad radius
$R_{pit}$	Pit radius
$R^*$	Equivalent radius
$R_s$	Stress ratio
S12	Shear stress
S11	Tensile stress
S22	Normal stress
$t$	Time
$t_{exp}$	Thickness
$\nu$	Poisson's ratio
$x_{ho}$	The peak point abscissa of homogeneous case
$x_{he}$	The peak point abscissa of heterogeneous case
$\sigma_{0[10^6]}$	Plain specimen fatigue strength
$\sigma_{ref}$	Reference material strength

$\sigma_{UTS}$	Ultimate tensile stress
$\sigma_{axial}$	Axial stress
$\sigma_{f-1}$	Fatigue limit under tension
$\sigma_n^{max}$	Maximum normal stress
$\sigma_{reaction}$	Reaction stress
$\sigma_{x,max}$	Peak tangential stress
$\sigma_y$	Tensile yield strength
$\sigma_{\theta\theta}, \sigma_{rr}$ and $\tau_{r\theta}$	Stress components in the polar system
$\sigma_f'$	Sensile fatigue strength coefficient
$\gamma_f'$	Shear fatigue ductility coefficient
$\varepsilon_f'$	Tensile fatigue ductility coefficient
$\theta_p$	Crack growth orientation
$\theta_{ho}$	Critical plane orientation of homogeneous specimen
$\theta_{he}$	Critical plane orientation of heterogeneous specimen
$\theta_c$	Critical plane orientation
$\tau_f'$	Shear fatigue strength coefficient
$\tau_{f-1}$	Fatigue limit under torsion
$\tau_y$	Shear yield strength
$\Delta\gamma_{max}$	Maximum shear strain amplitude
$\Delta\varepsilon_n$	Normal strain amplitude
$\Delta\tau_{max}$	Maximum shear stress range
$\mu$	Coefficient of friction
$v$	Volume ratio

## Acronyms

2D	Two-dimensional
CCT	Center cracked tension specimen
CP	Critical plane parameter
FEA	Finite element analysis
FP	Findley parameter
FS	Fatemi-Socie parameter

LEFM	The linear elastic fracture mechanics
MERR	Maximum energy release rate
MTS	Maximum tangential stress
MTSN	Maximum tangential strain
RVE	Representative volume element
SED	Minimum strain energy density
SEM	Scanning electron microscopy
SIF	Stress intensity factors
SWT	Smith-Watson-Topper parameter
TCD	Critical distance method
XFEM	Extended Finite Element Method

<b>Chapter 1</b> <b>Introduction</b>
--------------------------------------

# Introduction

## 1.1 Fretting fatigue

The weakening of components due to cyclic loading is fatigue. After a certain amount of load cycles, the microcrack appears from stress concentration geometric features location. And the microcrack continues growing as the effect of the cyclic loading, and finally resulting in complete failure.

And in tribology, the fretting will occur when there is lateral reciprocating vibration between the two contact bodies. Such vibration amplitude can even be at micron level [1]. The presence of fretting will cause high stress gradients near the contact area, which poses a huge challenge to mechanical structure design and fatigue life prediction. As the relative sliding amplitude increases, fretting can be divided into three different regimes: stick, partial sliding, and gross sliding.

Compared with uniaxial fatigue, due to small amplitude oscillatory relative movement between the two contact surfaces, fretting may cause fatigue life to be reduced by half [2, 3]. Fretting fatigue problems are common and have a great impact on engineering applications [4-12]. In the biomedical field, the fatigue of artificial hip joints, bone plates, and intramedullary nails are rarely caused only by plain fatigue. Corrosive effects of body fluids and fretting phenomenon will cause wear and accelerate fatigue failure of the structure [13]. In the automotive industry, by considering fretting fatigue, improvements to suspension components

---

can increase fatigue life without increasing costs [14]. Fretting fatigue failures have also been observed in automotive shock valves [15]. Such failures can also occur in the bolted joints [16], aircraft engine fan dovetail attachments [17], bridge cable wires [18] etc. Fretting fatigue accounts for 1/6 of aircraft engine failures according to the statistics of the United States Air Force [19, 20]. More practical applications of fretting fatigue are summarized in a review article, i.e. Ref. [21]. Most of the materials involved are high-strength steel, various alloys, etc.

In fretting contact, the edge of the contact surface is usually a sliding area, and the middle is a sticky area. The relative sliding near the contact edges converts mechanical energy into heat energy [22]. If the normal load is small, the sliding is a gross slip regime, and the wear of the relative sliding area will be very serious, which is the phenomenon of fretting wear. If the normal load is large, only the part of the contact edge slides, and the effect of wear is almost negligible, which is the phenomenon of fretting fatigue [23]. In fact, the most fundamental reason is that the fretting load causes a huge peak of shear stress near the contact edge [24, 25] as a stress concentration. This shear stress peak will act together with the cyclic tensile load of the component itself, resulting in a shorter fatigue life compared with the pull and compressive fatigue. The failure process is generally characterized by two phases, crack nucleation[26, 27] and crack propagation[11, 28]. For fretting fatigue, the crack initiation stage mainly has shear stress or strain control, and the crack propagation mainly

---

depends on the normal stress at the crack tip [29]. Researchers are concerned with contact forces because it directly affect the initiation of cracks[9]. And the contact stresses are affected by various factors, such as loading magnitude, contact geometry, surface imperfections and slip amplitude, which consequently affect the failure process. In addition to experimental methods, numerical simulation is an effective method to study fatigue problems [9, 10, 30-35]. As Fretting fatigue is a multi-axis and non-proportional stress problem [36], in order to predict the initiation lifetime, various approaches have been developed. The critical plane method is a widely accepted criterion that defines the direction that is most prone to cracking as a critical plane, and then it calculates the damage parameters based on this plane [37] [38] [39].

The crack initiation size is at micro-level, which is close to the grain size of materials [40]. After that, the linear elastic fracture mechanics (LEFM) approach normally is applied to predict the crack propagation life [25]. The well-known Paris' law is used through stress intensity factors (SIF) near the crack tip to calculate the number of fatigue life. The stress intensity factor is the physical quantity used to characterize the displacement and stress fields near the tip of the crack. According to cracking modes, different modes of stress intensity factors are defined. And a variety of equivalent factors have been proposed to predict the cracks propagation of multiaxial fracture [41-44]. Then the J-integral method is needed to achieve the gradual growth of cracks. Therefore,

choosing the appropriate crack propagation trajectory prediction method is important [45]. Maximum tangential stress (MTS) and "local symmetry" orientation criteria give a good accuracy of prediction for proportional loading conditions cases [46-48]. However, an extension of MTS criterion [49] has much better performance for fretting fatigue problem, which can be used in the case of non-proportional load conditions [50].

In general, fretting fatigue is widespread in practical applications and can greatly shorten the lifetime of components. Many studies have attempted to more accurately predict the fatigue life of components with different geometries, loads, and environmental conditions through experiments and numerical methods. The influencing factors and mechanisms of this failure need to be revealed. Finally, exploring ways to reduce adverse effects and extend the total fatigue life is necessary.

## **1.2 Objectives**

The main purpose of this thesis is to study the influence of the micro and macro scales of the component on fretting fatigue. Various techniques are used to prevent damage and improve fatigue life, such as optimizing the smelting process, using laser shot peening [51], using crack arresting technique [52], etc. Many of them are achieved by reducing structural

stress concentration. So, the study at micro and macro scales of the component is necessary and important.

In the literature, homogeneous materials are widely assumed to study fretting fatigue problems [53]. However, as a common consensus, heterogeneity of material has a great influence on the life and stability of the structure [54]. For many engineering components, the required design lifetime may be greatly affected by heterogeneity. Therefore, material heterogeneity has been widely studied in recent years [53, 55-58]. In addition to contact area, the subsurface area can also be affected by the heterogeneity, and in some cases, it is very strongly affected [59]. The heterogeneity usually refers to second phase inclusions [60-62], porosities [63-65], fibres [66-70] and micro-cracks [53, 71]. In this study, by combining the finite element and representative elementary volume (RVE) technology, the two most common inclusions ( $\text{Al}_2\text{CuMg}$  and  $\text{Al}_2\text{O}_3$ ) and the ubiquitous micro-voids in aluminium alloys are introduced into the fretting fatigue specimen. The initiation of cracks from the subsurface often depends on the most dangerous defect called a critical defect [72]. If all micro-voids diameter is below a critical value, i.e.  $25\ \mu\text{m}$ , the heterogeneous and homogeneous Sr-modified A356 alloys will have similar fatigue strength [73]. In this work, a numerical simulation method is established to study the effect of a single critical micro-void on fretting fatigue. Furthermore, the critical plane method and the critical distance (TCD) method are combined to predict the crack initiation

---

lifetime, position and crack plane of the heterogeneous specimen contain a single critical micro-void. All models use the representative volume element (RVE) method to consider the most common defects of inclusions and micro-voids in the specimen material. In addition to the critical micro-void near the contact edge will accelerate the initiation of cracks, the micro-void in the appropriate position will reduce the stress at the crack initiation point and extend the fatigue life. In fretting fatigue, the crack initiation point generally appears on the contact surface near the contact edge. The contact surface geometry will seriously affect the contact stress distribution and relative sliding under the same loading condition, thereby further affecting fatigue and wear results. So, according to the fretting fatigue structure of the cylindrical pad [45, 74] in contact with flat specimen, this study proposes improvements to the standard experimental geometry (flat-specimen) by adding artificial cylindrical pits to the specimen. The influence of different pit schemes on the crack initiation position and life are predicted through the critical plane methods and Ruiz parameters. In the crack propagation stage, stop hole technology is widely used as a crack arrest method. When the crack is introduced into the stop hole, new cracks will be initiation at the edge of the hole, thereby extending the fatigue life. However, the research on the application of this technology to fretting fatigue is still lacking. Different time and location for drilling stop holes will cause different crack propagation paths and lives.

---

In general, the goal of this thesis is to study the effect of micro and macro geometries (artificial cylindrical pits, inclusions, critical micro-void and stop hole) on the initiation of damage and propagation of cracks in fretting fatigue.

### **1.3 Outline**

Including the introduction of this chapter, there are seven chapters in this dissertation, which are organized in the following way. Chapter 2 starts with a literature review of fretting fatigue and micro and macro scales background knowledge. The first section contains an introduction to the classical analytical solution of contact mechanics. Secondly, different types of micro and macro models that affect fatigue life are reviewed. In the third section, the application of the finite element technique to fretting fatigue is introduced. The representative volume element (RVE) method is used when considering inclusions and critical micro void. The crack initiation and propagation processes and behaviours involved in this thesis are discussed. And then, the chapter provides a theoretical background discussion of the numerical methods related to this dissertation. The fatigue crack initiation parameters and the TCD method are introduced. Finally, the LEFM is introduced as a common approach for studying crack propagation.

---

In Chapter 3, the effect of randomly distributed inclusions on stress and strain fields in the specimen are studied in combination with RVE method. The contact surface stress distribution obtained by finite element simulation is verified by comparison with the theoretical solution. The element size near the inclusion is also determined through a convergence study. Finally, ten cases of randomly distributed inclusions with different volume ratio, size and shape are studied.

Chapter 4 presents a discussion on the use of different critical plane parameters combined with TCD method, and the effect of the most dangerous critical void on the fretting fatigue crack initiation. This combination of methods is verified by comparison with the fretting fatigue experiments of homogeneous specimen. Critical micro-voids at different positions relative to the contact edge are considered. The crack initiation location and orientation of fretting fatigue can be predicted. There are two potential crack initiation points, namely the contact edge and the micro-void edge. Therefore, each prediction not only considers the damage parameters of the contact surface but also includes the internal distribution of the specimen below the contact surface. Finally, it is found that the critical micro-void can not only reduce the initiation life but also increase the life with appropriate micro-void.

In Chapter 5, a surface cylindrical pitting treatment method is proposed to reduce the peak value of damage parameters by increasing the contact radius. Adding a cylindrical pit on the specimen surface can change the

contact stress distribution. Three critical plane parameters are used to predict crack initiation location and life. However, the contact slip amplitude of pad with specimen with cylindrical pits is larger. Therefore, Ruiz parameter is used to consider the effect of the contact slip. The results show that the predicted crack initiation positions of all damage parameters are the same. And all the damage parameters are lower than those of flat specimen case when the pit radius is appropriate.

Chapter 6 applies the widely used stop hole technology to the fretting fatigue crack propagation stage in order to extend the lifetime. Here, the fatigue fracture consists of four parts. The first is the crack initiation at the contact edge. Then, there is the first stage of crack propagation. After that, the stop hole is added at the crack tip, so the second crack initiation takes place at the edge of the hole. The last stage is the second crack propagation stage until the final fracture. In this Chapter, the first initiation will not consider, but we only compare the difference of remaining stages. LEFM approach is used to study the crack propagation stage. The Paris' law is applied to predict the crack propagation life. The maximum  $\Delta K_I^*(\theta)$  criteria is used to predict the crack growth orientation. Next, the critical plane parameter and variable length TCD method are used together to predict the second crack initiation lifetime. The above method is verified by the central crack tensile fatigue experiment, which considers the stop hole. Finally, the effects of different drilling positions and different hole radii on the fretting fatigue crack propagation life are discussed.

In Chapter 7, the main conclusions of this dissertation are listed, and the suggestions for future work are elaborated.

## Chapter 2      Theoretical background

Fretting fatigue is a comprehensive and complex failure phenomenon, which involves contact mechanics, materials science, and fracture mechanics. The main purpose of this chapter is to review the classic theories and background knowledge related to this thesis. Therefore, the classical contact mechanics is reviewed firstly. And the theoretical contact stress distribution of fretting fatigue is also presented in detail. Next, the macro and micro models which can affect the fatigue performance of material are discussed. Then, the basic concept of fretting fatigue including initiation and propagation are reviewed. Finally, the numerical method used in this thesis is introduced which includes FEM, critical plane parameters, critical distance method, and linear elastic fracture mechanics.

### 2.1      Contact mechanics

Contact mechanics is the study of the deformation of bodies that touch each other [75]. Due to the complexity of industrial mechanical structures, contact problems appear in many mechanisms. The research of elastomers contact proposed by Hertz opened a new horizon in contact mechanics [76]. The distribution of contact force and its influence on

---

mechanical properties are the focus of this research. In practical applications, most components involve contact issues such as fatigue [45], joints components [77, 78], collision [79-81], conductive [82], seal [83], biological films [84], etc. And in engineering, various mechanical loads are usually applied through contact, which will cause deformation and stress redistribution of the component. The existence of friction and material plasticity makes the problem highly nonlinear and complicated. Predicting structural deformation and failure are inseparable from the study of contact mechanism. Back in the 1880's, the well-known Hertz contact model [85] gives a theoretical approximated solution for the elastic phase of spherical bodies in contact. In the study of practical problems, contact stress has always been the focus of attention. Before we study the fretting fatigue behaviour, a brief review of contact mechanics theoretical solution is presented here.

### **2.1.1 Normal line contact**

The contact between a cylinder and a flat body (or two parallel cylinders) is a line contact. The contact situations covered in this thesis belong to this type of contact.

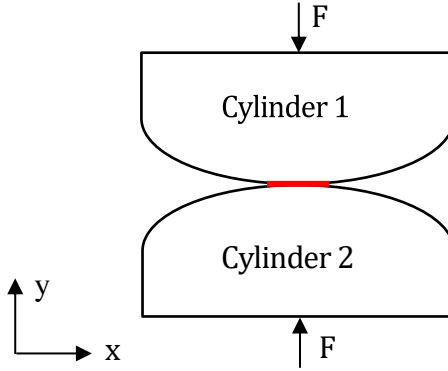


Figure 2.1. Normal line contact with only a normal force.

Firstly, we suppose that the two cylinders in contact are both elastic and isotropic homogeneous materials. Secondly, the contact surface is smooth without any lateral friction and only a normal force  $F$  is to compress the two bodies. Next, the deformation is relatively small compared with the size of cylinders as shown in Figure 2.2. The analytical solution [75] is given to obtain the normal stress distribution on the contact surface:

$$p(x) = -p_{max} \sqrt{1 - \left(\frac{x}{a}\right)^2} \quad (2.1)$$

Where  $p(x)$  represents the normal stress distribution,  $a$  is the semi-contact width and  $p_{max}$  is the peak value of normal contact stress at the contact centre and is given by:

$$p_{max} = \sqrt{\frac{FE^*}{t_{exp}\pi R^*}} \quad (2.2)$$

Where  $t_{exp}$  is the thickness of both contact cylinders. The  $R^*$  is the equivalent radius and  $E^*$  is the equivalent modulus of elasticity, i.e.

$$\frac{1}{R^*} = \frac{1}{R_1} + \frac{1}{R_2} \quad (2.3)$$

$$\frac{1}{E^*} = \frac{1 - \nu_1^2}{E_1} + \frac{1 - \nu_2^2}{E_2} \quad (2.4)$$

$R_1$  and  $R_2$  are the curvature radii of two contact cylinders.  $E_1$  and  $E_2$  are Young's moduli, and  $\nu_1$  and  $\nu_2$  are Poisson's ratios for the two bodies, respectively. And the semi-contact width  $a$  is given by:

$$a = 2 \sqrt{\frac{FR^*}{t\pi E^*}} \quad (2.5)$$

Figure 2.2 shows the normal stress distribution of the contact interface of the specimen. On the whole contact surface (between  $-a$  and  $a$ ), there is a parabolic distribution. The peak value of contact stress appears at the centre.

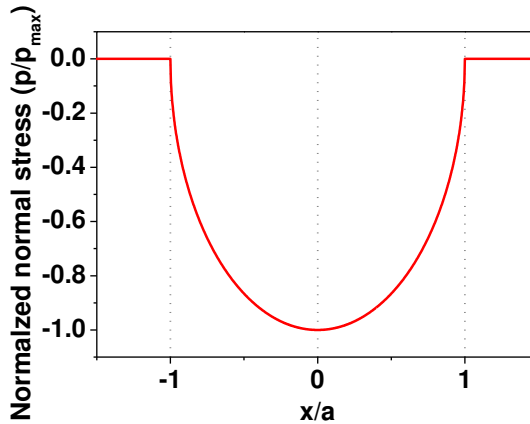


Figure 2.2. An example of normal stress distribution of the contact surface.

### 2.1.2 Line contact under partial slip

Based on pure normal contact, the fretting occurs because of the tangential force  $Q$ . To illustrate the effects of tangential loading  $Q$  a modified formulation is required [86, 87]. As shown in Figure 2.3, the two cylinders are in contact with each other under the combined action of the normal force  $F$  and the tangential force  $Q$ . The red line is the contact region. And near the contact edge,  $c \leq |x| < a$ , these are slip zones and there will be relative sliding between the contact interfaces. Two sliding zones are symmetrical to the contact centre. Therefore, we can express the shear stress  $q(x)$  by Coulomb friction law as  $\mu p(x)$ . The  $\mu$  is the coefficient of friction. Whereas, near the contact center,  $|x| \leq c$ , there is a centrally symmetric stick zone which means that the contact surfaces will

move together. So that in this zone the shear traction  $q(x)$  does not reach the critical value  $\mu p(x)$ .

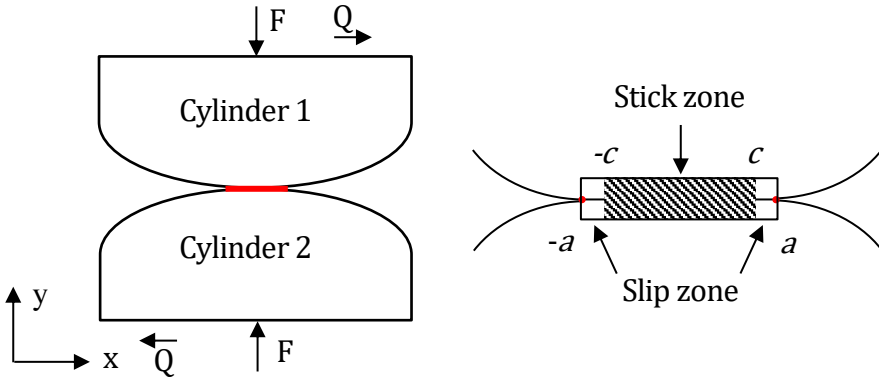


Figure 2.3. An example of line contact under partial slip with a tangential loading  $Q$ .

The contact shear traction can be modeled by the Coulomb friction law[22, 75], which is given by:

$$q(x) = q_1(x) + q_2(x) \tag{2.6}$$

Where  $q_1(x) = \mu p(x)$

$$q_1(x) = -\mu p_{max} \sqrt{1 - \left(\frac{x}{a}\right)^2} \tag{2.7}$$

Moreover, in the slip zones, the perturbation  $q_2(x)$  is zero.

$$q_1(x) = 0, c \leq |x| \leq a \tag{2.8}$$

However, for the stick zones, it is given by:

$$q_2(x) = \mu p_{max} \frac{c}{a} \sqrt{1 - \left(\frac{x}{c}\right)^2}, |x| \leq c \quad (2.9)$$

Where

$$\frac{c}{a} = \sqrt{1 - \frac{Q}{\mu F}} \quad (2.10)$$

Finally, when normal loads  $F$  and tangential loads  $Q$  simultaneously, the shear stress distribution on the contact surface is expressed as:

$$q(x) = \begin{cases} -\mu p_{max} \sqrt{1 - \left(\frac{x}{a}\right)^2}, c < |x| \leq a \\ -\mu p_{max} \left[ \sqrt{1 - \left(\frac{x}{a}\right)^2} - \frac{c}{a} \sqrt{1 - \left(\frac{x}{c}\right)^2} \right], |x| \leq c \end{cases} \quad (2.11)$$

The stress distribution when the normal and tangential loads acting simultaneously is shown in Figure 2.4.

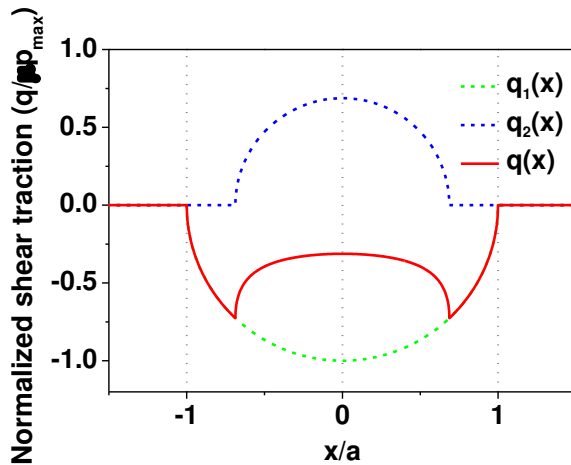


Figure 2.4. An example of the shear stress distribution for normal and tangential loads case.

Further, the structure of the fretting fatigue experiment is shown in Figure 2.5 (a). Two cylindrical pads compress a flat specimen under the action of a normal force  $F$ . And two springs are attached to the fretting pad, which will generate the tangential load  $Q$ . In addition, the coefficient of friction between the contact surfaces is  $\mu$ . The axial load  $\sigma_{axial}$  is acting on the right side of specimen. Under the combined effect of these loads, so that fretting fatigue will occur around the contact area. Compared with the previous example, there is one more effect from the bulk stresses  $\sigma_{axial}$ .

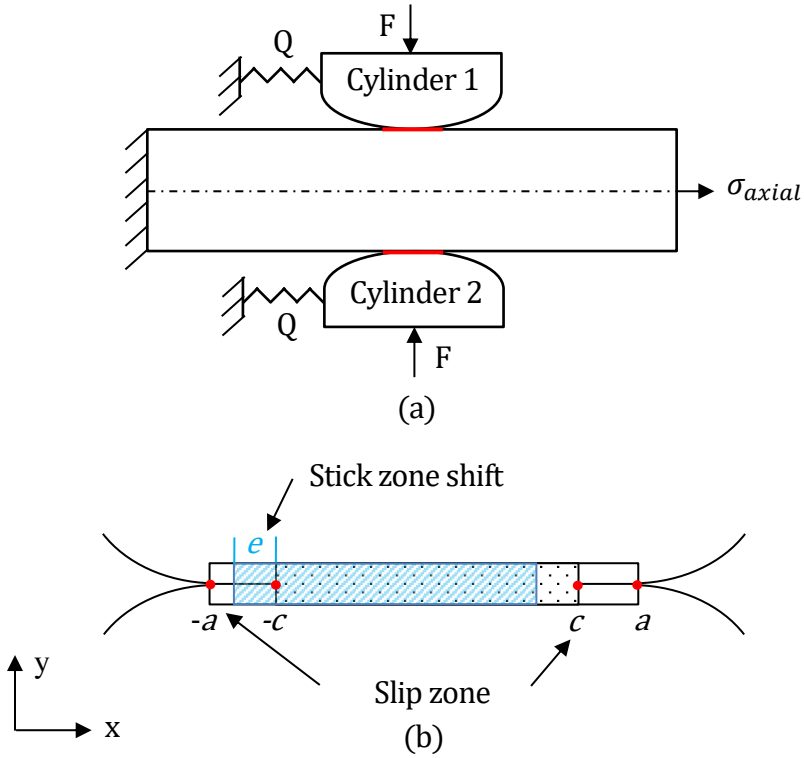


Figure 2.5. Fretting fatigue contact.

And thus the perturbation shear traction  $q_2(x)$  is given by [22]:

$$q_2(x) = \mu p_{max} \frac{c}{a} \sqrt{1 - \left(\frac{x + e}{c}\right)^2}, |x + e| \leq c \quad (2.12)$$

In the above formula, there is an eccentric displacement  $e = \frac{a\sigma_{axial}}{4\mu p_{max}}$  in the stick zones as shown in Figure 2.5 (b). For the slip zone, the shear traction

still follows the Coulomb friction model  $q(x) = \mu p(x)$ . Therefore, the shear stress is given by:

$$q(x) = \begin{cases} -\mu p_{max} \sqrt{1 - \left(\frac{x}{a}\right)^2}, & -a \leq x < -c - e, c - e < x \leq a \\ -\mu p_{max} \left[ \sqrt{1 - \left(\frac{x}{a}\right)^2} - \frac{c}{a} \sqrt{1 - \left(\frac{x+e}{c}\right)^2} \right], & |x+e| \leq c \end{cases} \quad (2.13)$$

An example of the above analytical solutions is shown in Figure 2.6.

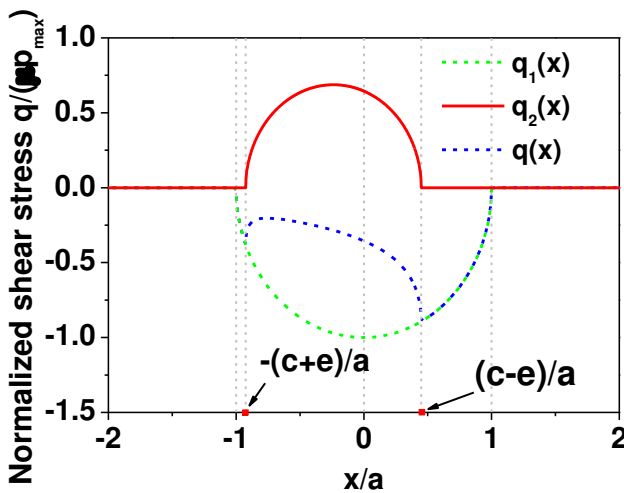


Figure 2.6. Shear stress distribution at the contact interface.

Due to the existence of bulk stresses  $\sigma_{axial}$ , the tangential stress on contact surface will be much greater than the previous two load situation.

For fretting fatigue, the peak tangential stress  $\sigma_{x,max}$  located at the contact edge ( $x = a$ ), where the initial crack is usually found [22, 45, 88-90]. So, as the principal stress, the maximum tangential stress is important for fretting fatigue crack initiation location and lifetime. And McVeigh and Farris [91] proposed an empirical formula to predict the maximum tangential stress:

$$\sigma_{x,max} = 2p_{max} \sqrt{\frac{\mu Q}{F}} + \sigma_{axial} \quad (2.14)$$

Through the above discussion, it can be found that the change of load will obviously affect the contact stress distribution, which will cause different failure behaviours. It is recognized that in addition to the influence of load, the structure of the component is also very important for stress distribution. In the next section, several common micro and macro structures that can reduce or increase the fatigue lifetime are introduced. Then the fretting fatigue behaviour and related numerical research methods are reviewed.

## 2.2 Micro- and macro-structure

The fatigue failure process often starts at the weakest part of the material. At first, there is only a micro crack or micro-hole, and then it gradually grows into a macro crack. In the practical situation, the materials always

have some heterogeneity due to heat treatment process. So, in order to ensure sufficient fatigue life, the effect of discontinuities in the material on fatigue, such as inclusions, micro cracks and micro voids, etc., is great [59, 92]. At the macro level, it is usually assumed that materials are isotropic and continuous. Continuum mechanics is a theory used to solve the properties and responses at macro-scale level. The macrostructure of the contact surface affects the initiation and propagation of crack [93]. And the easiest way to capture cracks in the crack propagation stage that can extend life is by drilling holes near the crack tip, which is named a stop hole [94]. In this section, two micro- (inclusion and micro void) and two macro- (pit treatment surface and stop hole) structures will be introduced separately.

### **2.2.1 Micro inclusion and voids**

Researchers are concerned with contact forces because it directly affects the initiation of cracks [9]. And the contact stresses are affected by various factors, such as loading magnitude, contact geometry, surface imperfections and slip amplitude, which consequently affect the failure process. On the other hand, material properties also have a significant influence on contact stresses. With the continuous updating of experimental equipment, people have more and more understanding of the material microstructure. As a common consensus, heterogeneity of material leads to stress concentration which has a great influence on the life and stability of the structure [54]. For many engineering components,

the required design lifetime may be greatly affected by heterogeneity. Therefore, material heterogeneity has been widely studied in recent years [24, 53, 55-59]. Generally, materials contain second phase inclusions [60-62], fibres [66-70], porosities [63-65], or voids/cracks [53, 71] at the micro level, which is the cause of the heterogeneity.

SEM(scanning electron microscopy) is Generally used to observe the microstructure of material [95]. There are several kinds of typical inclusions in alloys;  $Al_2O_3$ ,  $MgO$ ,  $Al_2MgO_4$ ,  $CaSO_4$ ,  $TiB_2$ ,  $Al_3Ti$ . The material considered in this thesis aluminium alloy 2024-T3 is widely applied in the aviation field. Two kinds of inclusions  $Al_2CuMg$  and  $Al_2O_3$  that are very common embedding in aluminum alloy 2024-T3 [92]. SEM observations showed that inclusions in the material were highly discrete and random distribution. Typical geometric form of inclusions are particles, films or group of films and rods [96]. The inclusions can be regarded as foreign particles, which exist in metals[97]. According to the relative position of the inclusions and the material surface, there can be surface inclusions and internal inclusions [98]. As a result, stress concentration will appear at the interface between different materials, which may give rise to shorter fatigue life. Thus, in addition to the contact area, the subsurface area can also be affected by the heterogeneity, and in some cases, it is very strongly affected as presented in Ref [59]. For example, the stress concentration that appears around the randomly distributed inclusions will shorten fatigue life [24]. Therefore, this means

that the crack initiation point not only appears at the contact surface but also is likely to appear inside the material below the surface. There are many ways to study the behaviour of heterogeneous materials. Previous researchers have proposed several models to predict the effect of inclusions and defects on metal fatigue strength. Murakami and Endo [59] proposed an engineering guide to predict the fatigue strength of components with heterogeneity. Some experimental results about high-strength steels showed that fatigue failures were mostly caused by the inclusions inside the matrix [99-104].

It is shown that micro-voids are widely found in metallic materials. And when the micro-voids size in the material exceeds a critical value, the crack mainly originates near the micro-voids [65]. Fatigue cracks formed by micro-voids and micro-notches are more considered in the literature than cracks formed from second-phase inclusions [62]. Our work also showed that micro-voids produced greater stress and complexity of stress distribution than inclusions [24]. The numerical studies have found that fretting fatigue characteristics are difficult to be directly related to defect volume ratio and size. The experimental research found that the inclusion size and fatigue life had not a clear relationship with each other [105]. The initiation of cracks often depends on the most dangerous defect, which we can call a critical defect. From the experiment research proposed by Murakami and Endo [72], a similar conclusion was obtained. If all micro-voids diameter is below a critical value, i.e. 25  $\mu\text{m}$ , the

heterogeneous and homogeneous Sr-modified A356 alloys will have similar fatigue strength [73]. Kumar, Biswas [53] used numerical analysis to study the influence of heterogeneity on stress distribution in fretting fatigue problems. They studied heterogeneity by considering micro-voids in the material, which is easily found in metal alloy materials[63]. They found that the effect of heterogeneity on shear stress was greater than on normal stress. Normally, for homogeneous material, the peak shear stress appears at the contact interface. However, in the case of heterogeneous materials, the peak may shift to the micro-voids.

### **2.2.2 Surface pit treatment and stop hole**

Compared to uniaxial fatigue, fretting fatigue has more complex stress concentration and shorter life [106]. For homogeneous materials, the fretting fatigue performance mainly depends on the surface stress and strain distributions [107]. In addition to load, material, temperature and microstructure, the shape of the contact surface also has a significant impact on fretting fatigue crack initiation. Previous researchers have compared the stress profiles of the two most common fretting fatigue contact types: flat-flat and cylinder-flat by numerical and experimental method [108]. It shows that the cylinder-flat contact leads to earlier crack initiation than flat-flat contact. And the larger the pad width, the longer the crack initiation and propagation life is. The experimental crack initiation life prediction studies for these two contact geometries are also reported in Ref. [109]. The effect of contact edge geometry on the fretting

fatigue also is studied by numerical and experimental method [110]. The difference between the sphere and the cylinder contact are presented in Ref. [111]. The ratio between initiation life and the total life of spherical contact is much smaller than cylindrical contact. Hojjati-Talemi, Wahab [112] studied the influence of contact geometry on crack propagation behaviour. They found that for flat-flat and cylinder-flat type contacts, the maximum transverse stress occurs at the contact edge. The crack propagation life of the flat-flat and cylinder-flat type contact increases with the increase of the pad width. Fretting fatigue research mainly focuses on the cylindrical pad [45, 74] or flat pad [113, 114] contact with flat specimen. However, the improvement plan for the contact of cylinder-flat type will be discussed in this thesis. The artificial cylindrical pit is processed on the surface of the flat specimen so that the cylindrical pad is in contact with the cylindrical pitted specimen as shown in Figure 2.7.

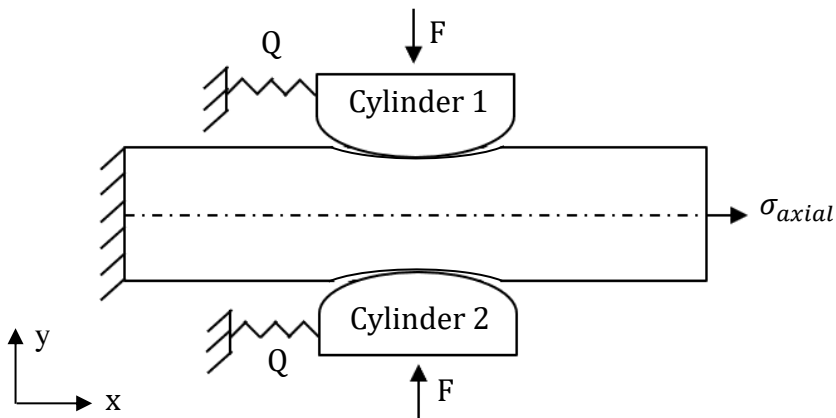


Figure 2.7. An example of surface cylindrical pit treatment contact.

The geometry of the contact surface can affect not only crack initiation but also crack propagation. Reasonable macro contact surface structure can effectively improve the overall fatigue life. However, for the crack propagation stage, there are also various crack repair techniques to extend the service life of components. For example overload technique [115-117], cold expansion [118-121], indentation (dimple) [52, 122, 123] and stop hole [52, 94, 117, 124-127]. A single overload causes crack closure, tip dullness and strain hardening near the tip. Lu, Yang [115] conducted a series of experiments on QSTE340TM automotive steel under different load ratios and overload ratios to study the effect of single overload on fatigue crack propagation. Cold expansion refers to drilling a hole at the crack tip, and then using an oversized steel ball to pass through the hole from one side to other sides. The residual stress caused by this process will effectively extend the fatigue crack propagation life [118]. The indentation or dimple technology use an indenter to press into the crack tip, generating residual compressive stress around it. The extension effect of 3 different indentation methods has been investigated by experimental and numerical methods [123]. The results show that applying a greater indentation load can better extend the service life.

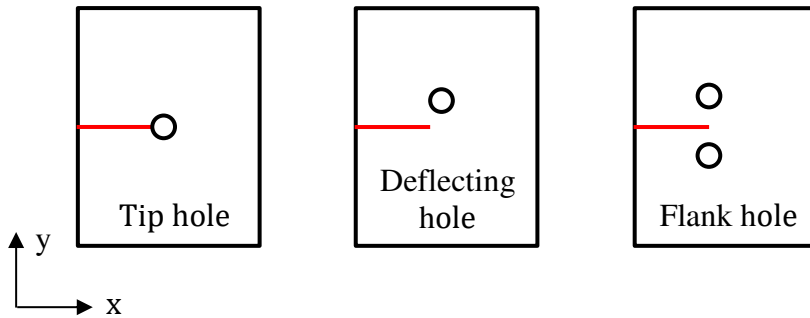


Figure 2.8. Three kinds of stop hole.

Compared with the above crack repair methods, stop hole technology is relatively simple and economical [126]. Adding stop holes at or near the crack tip can effectively reduce stress concentration. As shown in Figure 2.8, according to the relative location between the drilling position and the crack tip, there are three types of stop holes: tip hole, deflecting hole, and flank hole. The tip hole is located at the crack tip. And the second crack initiation will appear on the hole edge. The deflecting and flank hole can affect the stress intensity factor (SIF) to change the crack propagation direction and increase the fatigue life. Song and Shieh [126] carry out experimental research about the 6061-T651 aluminium alloy and AISI 304 stainless steel. They found that the larger the hole diameter, the longer the second crack initiation life is. Fanni, Fouda [128] optimized the shape of the stop hole and got a better extension effect than the circular hole. The effects of deflecting hole on the crack direction and residual life are studied by Hu, Song [127] through Extended Finite Element Method

(XFEM). Lu, Yang [117] completed the experiment of crack propagation under the combined application of stop hole and overload technology. Most of the above studies on stop holes are under pure mode-I or pure mode-II. Ayatollahi, Razavi [94] studied the effect of stop hole under mixed mode loads and predicted the initiation position of the new crack at the edge of the hole.

Through the above literature review, it can be found that the stop hole technology has always been a research hotspot. However, the research application of stop hole in fretting fatigue is still relatively few. The numerical and experimental research about the effect of stop hole on the fretting fatigue crack propagation is not available, but it is very valuable. So, this will be discussed in subsequent chapters of this thesis by numerical method. Fretting fatigue is more dangerous than pure fatigue due to its special loading condition. The crack propagation path is also more complicated. The behaviour and characteristics of fretting fatigue will be reviewed in the next section.

## **2.3 Fretting fatigue and numerical methods**

### **2.3.1 Introduction**

Due to the complexity of industrial mechanical structures, contact problems appear in many applications. The slight lateral relative movement between the contact surfaces causes the fretting phenomenon.

And fretting problems always involve fretting fatigue and fretting wear that two failure mechanisms. Therefore, according to different load conditions, fretting fatigue and fretting wear, respectively, dominate and commonly affect the failure. As shown in Figure 2.9, Vingsbo and Söderberg [23] provided the law of fretting wear volume and fretting fatigue life with respect to the relative sliding of the contact surface through experimental measurements.

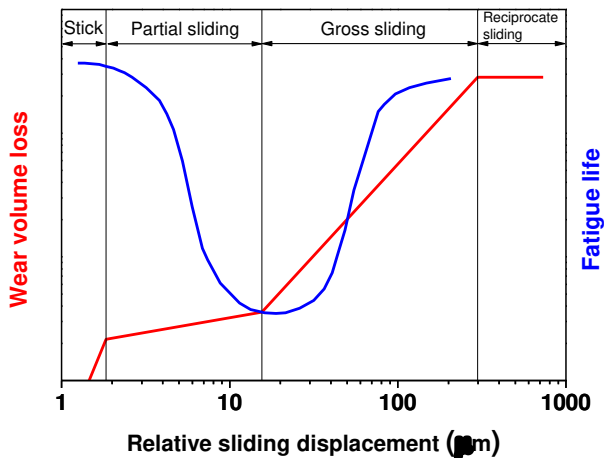


Figure 2.9. The influence of relative sliding displacement on fretting wear and fretting fatigue [23].

At stick regime, relative sliding tendency of two contact surfaces is small. They move together, so the fatigue wear is quite little and fatigue life is high. The partial sliding regime means that the two contact surfaces stick together at contact centre, and slide relative to each other at two contact

edges. Under this condition, the fatigue life reduce seriously. However, the volume of wear debris is reasonably low and not visible. Therefore, in the partial sliding regime, fretting fatigue dominate the failure. At the gross sliding regime, the wear increases significantly and the fatigue life increases instead. A large amount of surface wear removes the cracks initiating on the contact edge and form an oxide layer, thereby increasing the fatigue life. Therefore, under this regime, fretting wear is the focus of attention.

All cases involved in this thesis belong to the partial sliding regime. So here we focus on the fretting fatigue phenomenon, which is common and has a huge impact on engineering applications [4-12]. Fretting fatigue can significantly affect structural performance in many engineering applications[4]. The fatigue life of the structure may be reduced by the fretting phenomenon, which occurs due to small oscillatory motion between two contact surfaces [3]. The failure process of fretting fatigue is generally characterized by two phases, crack nucleation [26, 27] and crack propagation [11, 28] as shown in Eq. (2.15).

$$N_f = N_i + N_p \quad (2.15)$$

Where  $N_f$ ,  $N_i$ , and  $N_p$  are total fatigue life, initiation life, and propagation life, respectively.

The propagation phase is divided into the mixed propagation stage and the vertical propagation phase. In short, this fretting fatigue behavior can

be summarized in Figure 2.10. A detailed introduction will be given in the next section.

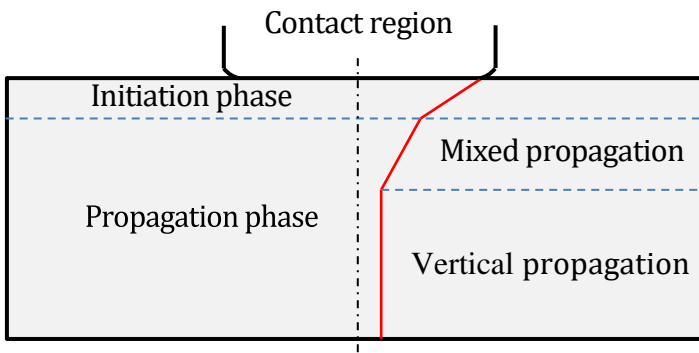


Figure 2.10. Fretting fatigue crack initiation and propagation process.

### 2.3.2 Finite element analysis

In addition to the theoretical solution of contact mechanics mentioned above, in order to study the mechanism of fretting fatigue, experiments using different equipment's and under different conditions were carried out [22, 45, 74, 129, 130]. Through observation, they gave many valuable and interesting conclusions, including crack initiation location and the effect of different loading conditions, etc. However, for experimental methods, it is difficult to obtain the details of stress field at crack initiation point and crack tip. Therefore, the finite element analysis (FEA) technique is a popular and powerful tool to solve nonlinear contact and multiaxial stress field problem such as fretting fatigue [9, 10, 30-35]. Lykins, Mall [131] proved that the crack initiation life and orientation

depend on the maximum shear stress range by a combined experimental-numerical approach. Their results show that it is necessary to analyse the stress and strain field of the contact surface under different loads. Especially when there are processing defects (inclusions, micro voids, etc.) near the high stress area [132]. In the experimental and numerical studies of fatigue crack initiation of HPDC magnesium AM60B alloy, Lu, Taheri [133] study the relationship between local maximum plastic shear strain range and casting pore features and loading conditions. And Gall, Horstemeyer [62] tried to quantify the driving force for fatigue crack formation from damaged inclusions and voids by numerical method. Yi, Gao [134] discussed the dispersion phenomenon in the fatigue life of cast A356-T6 aluminium-silicon alloy due to the existence of pores. As mentioned in the previous section, different types of microscopic defects are widely present in materials, which significantly affect fatigue life. Therefore, in fretting fatigue, the influence of defects near the contact edge on fatigue initiation life and crack orientation should be monitored. The FEA technique is also an important tool for the study of crack propagation. It is usually combined with LEFM to predict crack growth life and direction [45, 50, 94, 124]. The FEA technique can solve the local stress under different contact geometries and loading conditions. So, the FEA technique is an effective and convenient way to study the crack initiation and propagation phases of fretting fatigue quantitatively. The specific implementation method will be introduced in the following two chapters.

In the numerical simulation, if the various defects are randomly distributed in the whole specimen, it will bring a great computational cost. And in order to decrease the computational cost, the representative volume element (RVE) method is also commonly used to consider the void and inclusion inside the specimen [24, 135]. It can be used to obtain the equivalent mechanical properties of the heterogeneous material containing the defects by the Digimat-FEM [136]. As shown in Figure 2.11, we choose a small volume with periodic boundary conditions and microstructure, which can represent the property of the whole specimen. The equivalent macroscopic material properties can be obtained, in this way.

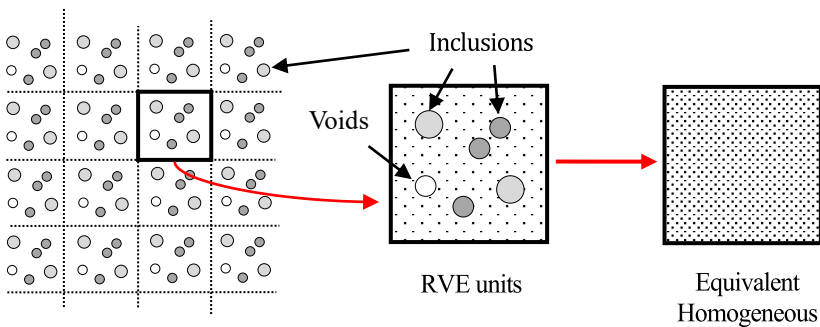


Figure 2.11. Schematic of RVE method.

The fretting fatigue FEM model of heterogeneous material can be built in two ways: use the equivalent homogenized material in the whole specimen, or model a small area near the contact region by the heterogeneous material with inclusions and use equivalent homogenized

material in the rest of the specimen. Since inclusion will cause stress concentration[59, 92, 98, 103], and fretting fatigue has maximum stress near the contact area[9]. So the second way will be chosen in order to study the effect of inclusion on the stress distribution near the contact area, and the partition diagram of the specimen is shown in Figure 2.12.

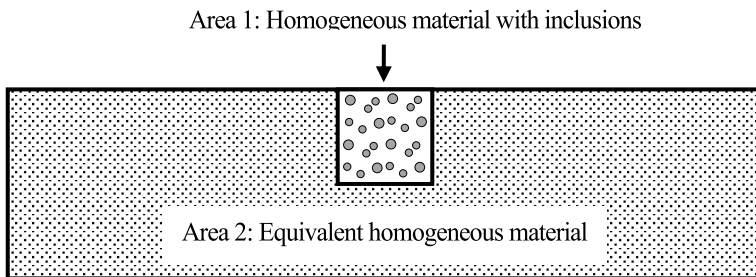


Figure 2.12. A partition diagram of the specimen with two areas.

### 2.3.3 Crack initiation

Generally, the initiation refers to the formation of cracks. Crack initiation is affected by load, microstructure and environmental variables. It is micro-level, which is close to the grain size of material [40]. However, it can account for a large part of the entire failure life. So, the research on initiation is very meaningful. The cyclical stress that causes fatigue is usually smaller than the static ultimate tensile stress or yield limit. But as long as the cyclical stress amplitude exceeds the fatigue limit, the damage accumulates continuously at the crack initiation point. Many experimental observations show that usually, the crack initiates at the

surface of component [132]. And irreversible local damage under cyclic loading usually leads to the development of a persistent slip band [132, 137]. When observing the fatigue crack initiation of copper, the intrusion and extrusion phenomena appear at the slip band on the material surface [138]. The formation of micro crack occurs after that.

### 2.3.3.1 Initiation location and orientation

For fretting fatigue, the stress concentration caused by contact dominates the crack initiation [90]. The initial crack is usually observed to appear at the contact edge as shown in Figure 2.13 [45, 89, 139, 140]. Although it is the main crack that causes the final failure, there are still several secondary cracks [131]. The main crack orientation  $\theta$  defined by the angle between crack and specimen surface perpendicular is shown in Figure 2.13. The crack initiation orientation observed through the experiment about AA2024-T3 is between  $-35^\circ$  and  $-45^\circ$  [45]. In the fretting fatigue crack test of titanium alloy Ti-6Al-4V, the obtained  $\theta$  by the different specimens are  $40^\circ$ ,  $-45^\circ/43^\circ$ , and  $-39^\circ$ , respectively [131]. These results indicate that the crack initiation phase of fretting fatigue in Figure 2.10 is dominated by shear. Under the combined effect of the tangential friction force on the contact surface and the cyclical transverse axial stress  $\sigma_{axial}$  acting on the specimen, inclined microcracks are gradually formed.

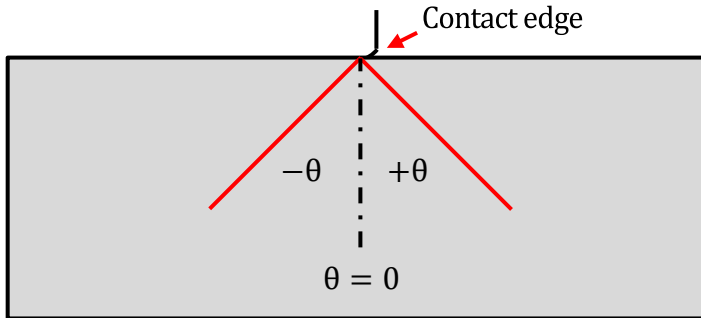


Figure 2.13. The main crack orientation defined by the angle between crack and the axis perpendicular to specimen surface.

### 2.3.3.2 Initial crack length

Due to the obvious difference between the growth rates, the fatigue process is divided into different phases from crack initiation to final fracture. As shown in Figure 2.10, the crack propagation phase is after the initiation phase. In the initiation phase, the crack length increases slowly, which mainly depends on the stress and strain at the initiation point. In the propagation phase, the crack growth rate mainly requires the determination of the stress intensity factor (SIF) at the crack tip. However, according to the literature, there is no clear definition of the crack initiation length, which is the boundary between the two phases. In experimental research, the initiation length often depends on the accuracy of the measuring instrument. For instance, usually the accuracy of non-destructive detection is  $380\ \mu\text{m}$ , and Lykins, Mall [131] assumed this value as the initial crack length. So, the average propagation life  $N_p$  is

between 6% and 15% of the total failure life  $N_f$  in their fretting fatigue experiment results. At the same time, the recognition limit of scanning electron microscope (SEM) technology is  $130\ \mu\text{m}$ . When  $130\ \mu\text{m}$  is used as the initiation length, the ratio  $N_p/N_f = 0.3$  [131]. And some experiments and numerical studies use experience to specify the initiation length. When the initiation life predicted by the critical plane method is compared with the experimental result,  $1\ \text{mm}$  is considered as the initiation length [74, 141]. In numerical simulations, there are usually two methods to determine the initiation length, namely variable initiation length and fixed initiation length. The main idea of variable initiation length is shown in Figure 2.14.

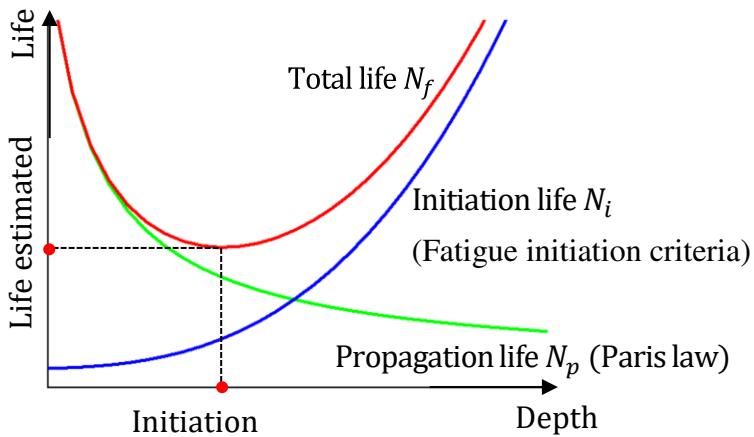


Figure 2.14. Total life estimated according to the initiation length [114].

The numerical prediction of fatigue life includes two parts, crack initiation life and crack propagation life. The general process is first to predict the crack initiation life through multi-axial fatigue criteria such as critical plane parameters or continuum damage mechanics. And then insert a short crack at the initiation location as the start point of crack propagation combine with Paris law to predict the crack growth life. For the green line shown in Figure 2.14, as the initiation length increases, the crack propagation life decreases, which is easy to understand. Usually, the stress at the initiation point is the highest, so the longer the crack initiation length, the smaller the equivalent or average stress. And the smaller the equivalent stress, the longer the predicted initiation life. So, the blue line in Figure 2.14 shows that the initiation life increases together with the defined initiation length. The red line is the total life having a minimum value as shown in figure 2.14. And Navarro, Garcia [142] assumed that when the total life takes this minimum value, the corresponding length is the appropriate initiation length. So, the initiation length is variable with different loading conditions. With variable initiation length, the numerical prediction and fretting fatigue tests result under spherical contact have a good consistency [142-144]. And Sabsabi, Giner [114] used the same method at the initiation phase and XFEM in the propagation phase to study the fretting fatigue under contact between flat pad and flat specimen. They showed that the combination of this method and the XFEM can make reasonable predictions compared to the experimental

results. The fixed initiation length is regarded as the critical minimum crack length of a material in fracture mechanics. And  $l_c$  can be calculated by El Haddad empirical law [145]:

$$l_c = \frac{1}{\pi} \left( \frac{\Delta K_{th}}{\sigma_{0[10^6]}} \right)^2 \quad (2.16)$$

where  $\Delta K_{th}$  is a long crack threshold stress intensity factor (SIF) range. And  $\sigma_{0[10^6]}$  is plain specimen fatigue strength of fatigue material.

In the research of fretting fatigue crack propagation life of AA2024-T3 specimen, the crack initiation length is considered as a fixed value of 50  $\mu\text{m}$  [45, 50]. Comparison with experiments shows that this method is reasonable and efficient. This thesis also uses the same fixed initiation length to study the crack propagation in AA2024-T3 specimen, then considers the crack propagation phase.

### 2.3.3.3 Critical plane and Ruiz parameter

Fretting fatigue is a multi-axis periodic load problem, which is a non-proportional loading condition. Especially near the contact edge of the specimen, high-stress concentration will occur. In order to predict the crack initiation life, scholars have established many empirical theoretical formulas. The critical plane approach is a widely used and validated method [146, 147]. In fact, under cyclic loading, the stresses are constantly changing, and during the deformation process, the energy is

also continuously transformed. When these parameters reach a critical value with time, cracks are generated. The critical plane approach is divided into three categories based on stress, strain, and energy [147]. For the critical plane of stress, the plane subjected to the maximum stress amplitude is defined as the critical plane. The strain and energy critical plane methods have a similar definition, which will be discussed in a later section. In addition to experimental research, recent numerical methods are increasingly used by researchers because they can help to understand in depth the distribution of stress and strain at the contact surface, which is difficult to be measured by experiments [148, 149]. Fretting fatigue is a complex multi-axis fatigue problem. The critical plane method is widely used as a recognized fatigue rule on fretting fatigue problems. In such a method, the crack will initiation along some special plane with the maximum critical plane parameter or shear strain amplitude. In this thesis, three kinds of critical plane parameters are used namely stress based Findley FP [150], strain based Fatemi-Socie FS [151], and energy based Smith-Watson-Topper SWT [152] parameters.

Normally the criteria of stress based are more suitable for high cycle fatigue. In addition, Findley defines the critical plane parameter as:

$$FP = \frac{\Delta\tau_{max}}{2} + k_1\sigma_n^{max} \quad (2.17)$$

where  $\frac{\Delta\tau_{max}}{2}$  is maximum shear stress amplitude on any plane passing a certain point in the whole loading cycle, and  $\sigma_n^{max}$  is the maximum normal stress on any plane passing this point.  $k_1$  is the material fatigue constant that can be obtained experimentally. In this study, it can be obtained using Eq.(2.18).

$$\frac{\sigma_{f-1}}{\tau_{f-1}} = \frac{2}{1 + \frac{k_1}{\sqrt{1 + k_1^2}}} \quad (2.18)$$

where  $\sigma_{f-1}$  is the fatigue limit under tension and the  $\tau_{f-1}$  is the fatigue limit under torsion of material. For the experimental materials (AA2024-T3) of this study, their values are equal to 114.9 MPa and 66.34 MPa, respectively [25, 153]. After Findley's work, Park [154] proposed a formula for predicting the crack initiation life:

$$FP = \tau_f' (2N_i)^b \quad (2.19)$$

where  $\tau_f' = 482.08$  MPa is the fatigue strength coefficient in shear and  $b = -0.096$  is the fatigue strength exponent in tension [153, 155]. The point at which the FP parameter reaches the maximum is the crack initiation starting point, and the plane passing this point is the critical plane, that is, the crack initiation plane.

Fatemi and Socie [38] proposed a critical plane criterion that can apply to materials and load conditions that produce shear mode failures. Moreover, it is also the most representative strain-based criterion. For this criterion, the critical plane is the orientation that is subjected to the maximum shear strain amplitude and has the largest FS parameter value. The  $N_i$  can be determined using Eqs.(2.20) and (2.21).

$$FS = \frac{\Delta\gamma_{max}}{2} \left( 1 + k_2 \frac{\sigma_n^{max}}{\sigma_y} \right) = \frac{\tau_f'}{G} (2N_i)^{b'} + \gamma_f' (2N_i)^{c'} \quad (2.20)$$

$$k_2 = \frac{\sigma_y}{\sigma_f'} \quad (2.21)$$

where  $\Delta\gamma_{max}$  is the maximum shear strain amplitude.  $b' = b = -0.096$  and  $c' = -0.644$  are the shear fatigue strength and shear fatigue ductility exponent.  $G$  is the shear modulus of elasticity;  $\gamma_f' = 0.2944$  is shear fatigue ductility coefficient;  $\sigma_y = 383$  MPa is tensile yield strength and  $\sigma_f' = 835$  MPa is tensile fatigue strength coefficient [153, 155].

For the energy based critical plane criteria, SWT parameter was proposed by previous scholars and was very suitable for tensile fatigue problems [156]. Then, on this basis, Socie [157] proposed the final form as shown in Eq. (2.22).

$$SWT = \sigma_n^{max} \frac{\Delta \varepsilon_n}{2} = \frac{\sigma_f'}{E} (2N_i)^{2b} + \sigma_f' \varepsilon_f' (2N_i)^{(b+c)} \quad (2.22)$$

where  $\Delta \varepsilon_n$  is normal strain amplitude, and  $\varepsilon_f' = 0.17$  is tensile fatigue ductility coefficient [153]. Through the formulas of the above three criteria, it can be found that the stress and strain history in the periodic load will determine the fatigue life of the specimen.

From the above description, it can be found that the critical plane parameters does not consider the influence of slip between the contact surfaces on the crack initiation. Ruiz, Boddington [158] studied the fretting phenomenon of dovetail joint between blade and disk in a gas-turbine configuration. The experimental results show the importance of fretting between the disk/blade interface. And they proposed two Ruiz parameters depends on their experimental observations. First one named wear parameter  $F_1$  which is given by:

$$F_1 = q(x)d_x \quad (2.23)$$

where  $q(x)$  is shear stress and  $d_x$  is the slip value.

The position, where has the maximum value of the wear parameter  $F_1$ , is close to the maximum wear location in the experiment. The second one is named initiation parameter  $F_2$ . It evaluates the crack initiation location and life by introducing tensile stress  $S_{11}$ :

$$F_2 = S_{11}\tau d_x \quad (2.24)$$

As shown in Figure 2.9, greater wear may lead to greater fretting fatigue life. Therefore, compared with Eq. (2.23) and Eq. (2.24), the maximum location of  $F_1$  and  $F_2$  may be different. Finally, this thesis will use the Ruiz parameters [158] to evaluate the influence of slip.

#### 2.3.3.4 The critical distance method

Various numerical fatigue parameters are widely used. For example, the critical plane method is usually used to predict the crack initiation life, position and angle. However, more and more works of literature prove that it is not appropriate to predict the crack initiation direction by using the critical plane of the peak point, which is called hot spot method. Moreover, because of stress concentration, the damage parameters decrease rapidly along the depth direction as the red dotted line shows in Figure 2.15. So the life of crack initiation will be underestimated if one uses the hot spot method directly [159, 160]. Due to the sharp changing stress in the vicinity of peak point, the critical distance (TCD) method, which was proposed by Taylor [161] based on linear elastic fracture mechanics, is commonly used to average the damage parameters around the crack initiation point [162, 163].

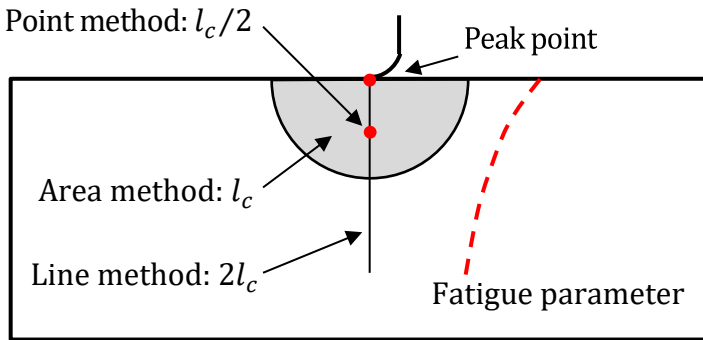


Figure 2.15. Schematic diagram of three critical distance methods.

The most two commonly used critical distance methods are point method (PM) and line method (LM). As shown in Figure 2.15, the PM defines the equivalence stress is of the point at  $l_c/2$  away from the peak point on the critical plane orientation. The characteristic critical distance  $l_c$  is equal to the crack initiation length, which can be calculated by El Haddad empirical law as shown in Eq. (2.16). Where the long crack threshold stress intensity factor range is  $\Delta K_{th} = 100 \text{ MPa}\sqrt{\text{mm}}$  [164], and the plain specimen fatigue strength is  $\sigma_{0[10^6]} = 263 \text{ MPa}$  for the aluminium alloy 2024 T3, therefore  $l_c = 46.02 \text{ }\mu\text{m}$ . And the LM defines the average stress of all point on the critical plane within  $2l_c$  distance, which is the equivalence stress. The other method is the area method (AM,) which determines the equivalence stress by average all points in the semi-circular with radius  $l_c$  and peak point as the center [45, 165, 166]. And Hattori, Ab Wahab [167], [168] combined the fretting fatigue S-N curve and critical distance theory to predict the high cycle and low cycle fatigue.

The Modified Wöhler Curve Method was also used together with it to estimate fretting fatigue strength of cylindrical contacts [169]. The combination of the critical plane method and the critical distance theory is used for the research of notched specimens under multiaxial fatigue loading[159]. And when the TCD method is applied to fretting fatigue problems, some scholars directly averaged the fatigue parameters in a specific range and obtained good results [144, 170-172]. The equivalence fatigue parameter can reduce the effect of the life underestimation caused by stress concentration.

As an extension of TCD method, Susmel and Taylor [166] assume that the characteristic critical distance  $l_c$  varies with the number of initiation fatigue life  $N_i$ . The  $l_c$  and  $N_i$  conform to a simple power function as:

$$l_c = AN_i^B \quad (2.25)$$

And there are two methods to fit the two parameters A and B. The first method is to consider the two extreme cases of static failure and fatigue limit. The distance calculated by Eq. (2.16) corresponding to  $N_i = 10^6$  is the state of fatigue limit. For static failure, a similar equation is given to predict the critical distance as [173, 174]:

$$l_c = \frac{1}{\pi} \left( \frac{K_{Ic}}{\sigma_{\text{ref}}} \right)^2 \quad (2.26)$$

Where  $K_{Ic}$  is the plane strain material toughness, and  $\sigma_{ref}$  is reference material strength. They assumed that the value of  $\sigma_{ref}$  is close to the ultimate tensile stress  $\sigma_{UTS}$ . And the static failure means that the crack initiation life is just one cycle. So, the critical distance obtain from Eq. (2.16) and Eq.(2.26) corresponding to  $10^6$  and 1 cycles [175]. Then, bringing these relationships into Eq. (2.25), the function between  $l_c$  and  $N_i$  can be obtained. It can be found that this method is very convenient for certain material with certain stress ratio, and the relationship between the critical distance  $l_c$  and the fatigue life  $N_i$  can be obtained directly through the material properties. However, the research shows that the fitting formula Eq. (2.25) obtained by two experiment cases with different stress gradient can provide more accurate prediction [173, 174]. The fatigue life of two cases get from experiment, and the stress gradient is obtained from simulation. Then, combined with fatigue parameters, a reasonable critical distance corresponding to two fatigue life can be found. Finally, the parameters A and B can be obtained.

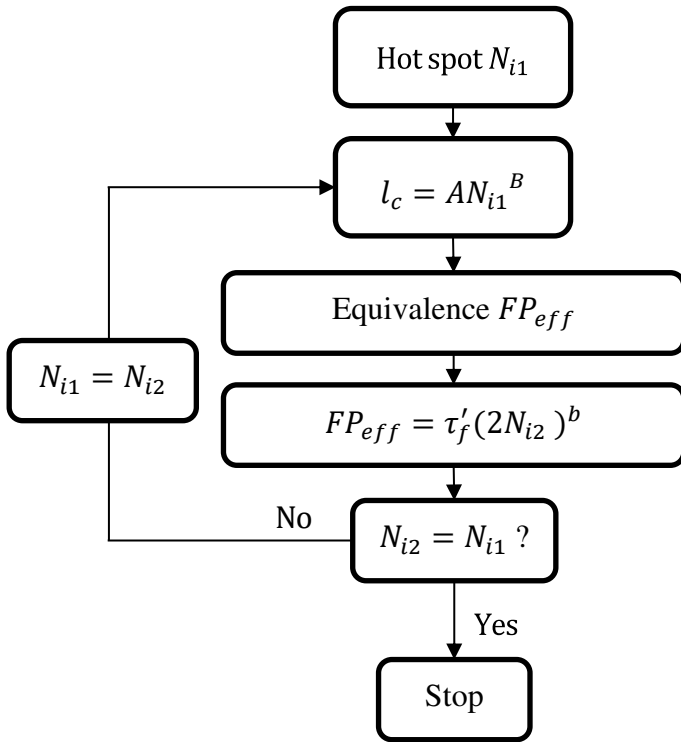


Figure 2.16. Flowchart of fatigue life prediction based on variable critical distance and FP parameter [166].

As an example, the FP parameter is used in Figure 2.16 to predict fatigue life based on variable critical distance. The averaged  $N_{i2}$  is assigned to  $N_{i1}$  until the results of two iterations are equal.

Finally, the combined application of critical plane parameter and critical distance method for predicting crack initiation response are summarized in Figure 2.17.

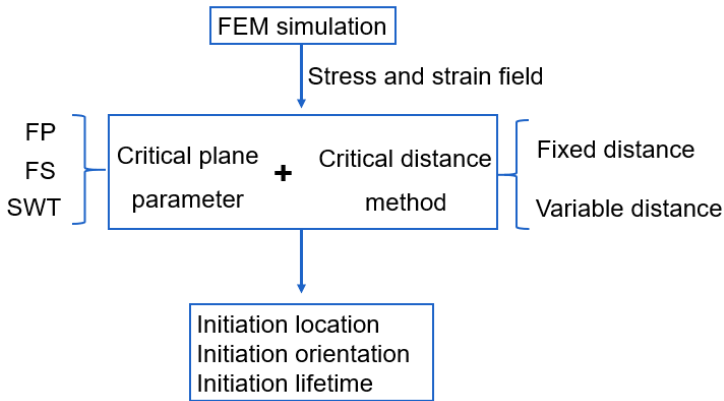


Figure 2.17. Combined application of critical plane parameter and critical distance method.

### 2.3.4 Crack propagation

As shown in Figure 2.10, the propagation phase of fretting fatigue is divided into the mixed propagation stage and the vertical propagation stage. This is because normally the crack originates at the contact edge and initiates inwards the contact zone [45]. The crack propagation behaviour is affected by fretting contact stress and bulk stress  $\sigma_{axial}$  at mixed propagation stage. So, in this mixed mode, the crack continues to propagate in a direction inclined to the surface. And the contact force of the fretting contact surface usually induces crack face closure. This closure also affects the crack propagation behaviour. When the crack length reaches the characteristic dimension of the contact zone, the influence of contact force can be ignored, which is the vertical propagation

stage [22]. In this stage, crack propagation is dominated by bulk stress and perpendicular to the contact surface until its final failure.

For crack propagation, the determination of crack growth rate and crack propagation direction is very important. Normally the linear elastic fracture mechanics (LEFM) approach is applied to predict the crack propagation behaviour [25, 45, 176]. The existence of the plastic zone at the crack tip lends the crack to grow gradually. When the plastic zone is relatively small compared to the size of the crack, the elastic stress field around this plastic zone can be used to describe the state of the crack tip. The stress field around the crack tip depends on the location, load and geometry. And the location in a polar coordinate system can be represented by radius  $r$  and angle  $\theta$  as shown in Eq. (2.27):

$$\sigma_{ij} = \sigma_{ij}(\text{Location}, \text{Loading}, \text{Geometry}) = \sigma_{ij}(r, \theta, K) \quad (2.27)$$

Where  $K$  is stress intensity factor (SIF), which is used to represent the combined effect of loading and geometry.

$$K = K(\text{Loading}, \text{Geometry}) \quad (2.28)$$

And there are three modes of SIF according to opening, sliding, and tearing loading mode. They correspond to Mode I, Mode II, and Mode III, respectively, as shown in Figure 2.18.

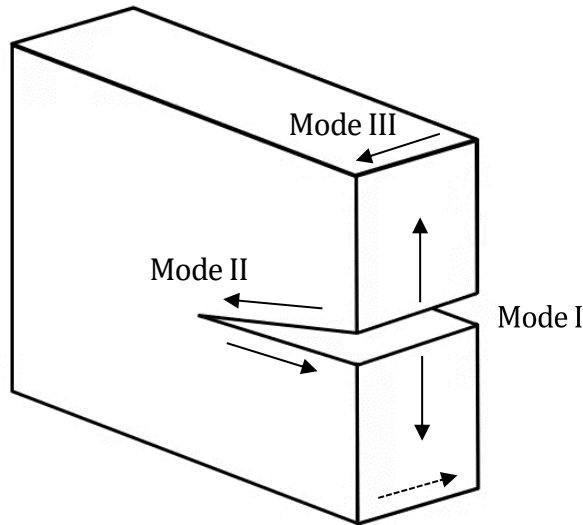


Figure 2.18. Three modes for crack growth.

#### 2.3.4.1 Crack growth rate

In order to improve the calculation efficiency, the fretting fatigue problem is usually treated as a plane strain problem. It is a mixed-mode fatigue include the effect of opening mode  $K_I$  and sliding mode  $K_{II}$ . The impact of loading can be ignored. And the calculation of crack growth rate can be written as:

$$\frac{dl}{dN} = f(\Delta K, R_s) \quad (2.29)$$

Where  $\Delta K$  is the stress intensity factor range at the crack tip. And  $R_s$  is the stress ratio and it also equals the ratio between the maximum and minimum SIF in one loading cycle.

$$R_s = \frac{K_{min}}{K_{max}} = \frac{\sigma_{min}}{\sigma_{max}} \quad (2.30)$$

So, the crack growth rate is affected by stress intensity factor range and stress ratio. Related experimental measurements are implemented to explore such influence laws [177].

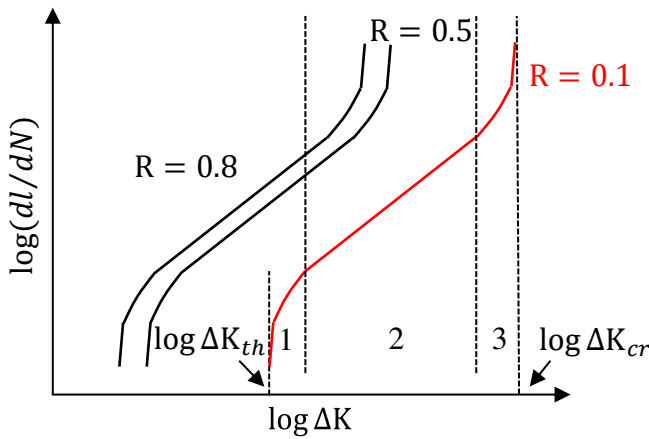


Figure 2.19. A typical plot of crack growth rate change with the stress intensity range.

A typical plot of crack growth rate change with the stress intensity factor range and stress ratio is shown in Figure 2.14. There are three different stress ratios, which are 0.1, 0.5, and 0.8, respectively. Under the same  $\Delta K$ , the lower the stress ratio  $R_s$ , the lower the crack growth rate. The red line shows the  $R_s = 0.1$  case and there are three regions from crack formation till final fracture. When the stress intensity factor range is approaching the long crack threshold,  $\Delta K_{th}$  is defined as the short crack

growth region (Region 1). In this region, the crack is short and grows very slow, which can be understood as crack formation process. If the maximum stress intensity factor increases till close to the fracture toughness  $K_{Ic}$ , the crack growth is very fast and unstable, which is region 3. The critical limit stress intensity factor range  $\Delta K_{cr}$  in Figure 2.19 can be expressed as:

$$\Delta K_{cr} = (1 - R)K_{Ic} \quad (2.31)$$

In region 2, the log-log plot is linear. And well known Paris–Erdogan equation is defined as [178]:

$$\frac{dl}{dN} = C\Delta K^m \quad (2.32)$$

Where  $C$  and  $m$  are a constant factor and an exponent, respectively. Both of them can get from the test. For material AA2024-T3 and  $R = 0.1$  case in this thesis, the factor  $C = 2.73 \times 10^{-11} \text{ (mm/cycle)/(MPa}\sqrt{\text{mm}})^m$  and exponent  $m = 2.6526$  are adopted [179]. The  $dl$  and  $dN$  are small increments in crack length and fatigue life, respectively. According to Eq. (2.32), the fatigue cycle of the crack propagation stage  $N_p$  can be predicted by the integral method as shown in Eq. (2.33):

$$\int_{a_i}^{a_f} \frac{dl}{C\Delta K^m} = \int_{N_i}^{N_f} dN = N_p \quad (2.33)$$

For the mixed-mode fatigue problem, such as fretting fatigue, there are different kinds of definition for  $\Delta K$ . As proposed by Irwin [42] and used by Liu [180],  $\Delta K$  equals to the equivalent SIF range  $\Delta K_{eff}$ , which is given as:

$$\Delta K = \Delta K_{eff} = \sqrt{\Delta K_I^2 + \Delta K_{II}^2} \quad (2.34)$$

Where  $\Delta K_I$  and  $\Delta K_{II}$  are mode I (opening) and mode II (sliding) stress intensity range at crack tip between maximum and minimum loading conditions. Tanaka [41] proposed another criterion for mixed-mode conditions based on the previous model [181]:

$$\Delta K_{eff} = [\Delta K_I^4 + 8\Delta K_{II}^4]^{1/4} \quad (2.35)$$

An in-plane mixed mode criterion is raised by Pook [182]. The equivalent SIF range can be obtained using mode-I and mode-II SIFs:

$$\frac{\Delta K_{eff}}{\Delta K_{th}} = [0.08 \left( \frac{\Delta K_I}{\Delta K_{th}} \right)^2 - 0.83 \frac{\Delta K_I}{\Delta K_{th}} + 0.75]^{1/2} \quad (2.36)$$

Where  $\Delta K_{th}$  is the threshold stress intensity range.

Defining a reasonable crack length increment  $dl$  and bring one  $\Delta K_{eff}$  criterion into Eq. (2.32), the propagation life increment  $dN$  can be obtained. If the direction of the next crack increment is known, the total propagation  $N_p$  can be obtained through integral by Eq. (2.33). So,

another key point is to predict the crack growth orientation according to the SIFs as shown in Figure 2.20.

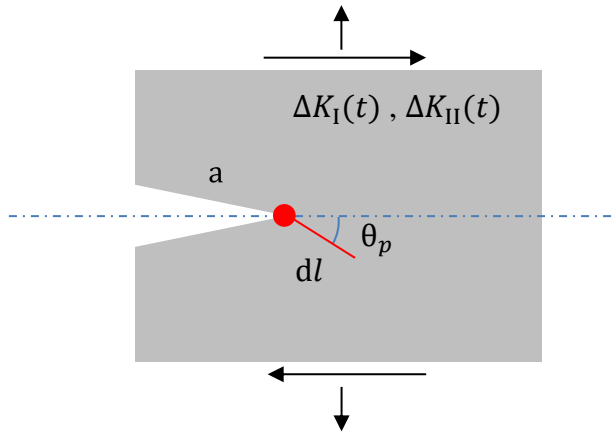


Figure 2.20. The prediction of the crack growth orientation according to the SIFs.

#### 2.3.4.2 crack growth orientation

Like crack growth rate, the crack growth orientation also depends on the stress and strain fields at the crack tip. Rozumek and Macha [183] reported that in the case of mixed-mode fatigue, non-proportional loads and crack closure would seriously affect the process of fatigue crack growth. And they summarized several orientation prediction criteria in the literature that can be applied to the mixed-mode fatigue problem. Many criteria are proposed in the literature such as the maximum tangential stress (MTS) [184], minimum strain energy density (SED) [185], the maximum energy release rate (MERR) [186], the maximum

tangential strain (MTSN) [187], and the zero  $K_{II}$  ( $K_{II} = 0$ ) [188] criterion. Different criteria are based on different assumptions. All these assumptions are related to the stress, strain or energy at the crack tip. For homogeneous linear elastic material, the crack tip stress in polar coordinates can be expressed as [189]:

$$\sigma_{\theta\theta} = \frac{1}{\sqrt{2\pi r}} \cos \frac{\theta}{2} \left[ K_I \left( \cos \frac{\theta}{2} \right)^2 - \frac{3}{2} K_{II} \sin \theta \right] \quad (2.37)$$

$$\begin{aligned} \sigma_{rr} = \frac{1}{\sqrt{2\pi r}} \cos \frac{\theta}{2} & \left[ K_I \left( 1 + \left( \sin \frac{\theta}{2} \right)^2 \right) \right. \\ & \left. + K_{II} \left( \frac{3}{2} \sin \theta - 2 \tan \frac{\theta}{2} \right) \right] \end{aligned} \quad (2.38)$$

$$\tau_{r\theta} = \frac{1}{2\sqrt{2\pi r}} \cos \frac{\theta}{2} \left[ K_I \sin \theta - K_{II} (3 \cos \theta - 1) \right] \quad (2.39)$$

Where  $\sigma_{\theta\theta}$ ,  $\sigma_{rr}$  and  $\tau_{r\theta}$  are stress components in the polar system. And  $r$  and  $\theta$  are crack tip coordinates as shown in Figure 2.21.

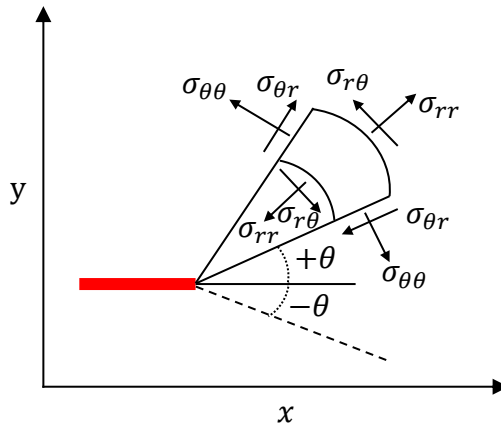


Figure 2.21. The stress near the crack tip in polar coordinates.

The most commonly used criteria proposed by Erdogan and Sih [184] (MTS criteria) defined the plane, which has the maximum tangential stress  $\sigma_{\theta\theta}$  on the crack tip is the growth orientation. And fracture yields when the maximum tangential stress  $\sigma_{\theta\theta}$  reaches a critical value. The maximum value can be obtained by set condition  $\partial\sigma_{\theta\theta}/\partial\theta = 0$  and  $\partial^2\sigma_{\theta\theta}/\partial\theta^2 < 0$ . The corresponding growth orientation is given by:

$$\theta_p = \cos^{-1}\left[\frac{3K_{II}^2 + \sqrt{K_I^4 + 8K_I^2 K_{II}^2}}{K_I^2 + 9K_{II}^2}\right] \quad (2.40)$$

$\theta_p$  is the angle between the predicted crack propagation direction and the original crack plane. And if  $K_{II} > 0$ , the growth orientation is negative. On the contrary, if  $K_{II} < 0$ , the growth direction is positive as shown in Figure 2.20.

Because the calculation is simple and has been verified by many experiments, MTS criteria is widely used [190, 191]. However, the existence of non-proportional load makes the crack propagation problem more complicated. In some cases, the MTS criteria also showed incorrectness [30, 45, 192]. As the fretting fatigue is a mixed-mode and non-proportional loading condition fatigue problem [193]. The traditional LEFM orientation criteria could not predict a reasonable crack path compared with fretting fatigue experimental results [45]. Therefore, scholars try to improve the traditional criteria (MTS, MERR,  $K_{II} = 0$ ). Hourlier, d'Hondt [49] extend the traditional MTS method to apply to multiaxial non-proportional loading condition. They proposed three orientation criteria that depend on stress intensity factors of branched crack on the crack tip instead of stress. They assumed that the direction has maximum  $K_I^*(\theta, t)$ ,  $\Delta K_I^*(\theta)$  or  $\frac{dl}{dN}(\theta)$  was the next growth orientation.

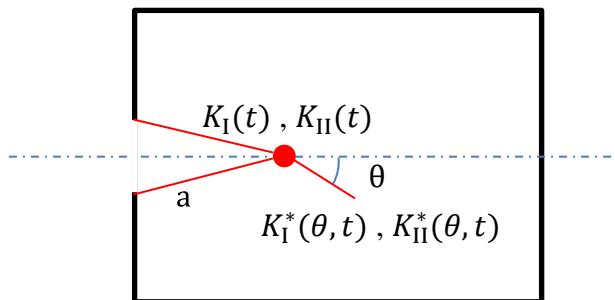


Figure 2.22. The stress intensity factor of branch cracks.

In one loading cycle, the  $K_I$  and  $K_{II}$  on the crack tip change with time  $t$ . Therefore, the stress intensity factor of branch cracks in different directions at the crack tip as shown in Figure 2.22 can be expressed as [194, 195]:

$$K_I^*(\theta, t) = K_{11}(\theta)K_I(t) + K_{12}(\theta)K_{II}(t) \quad (2.41)$$

$$K_{II}^*(\theta, t) = K_{21}(\theta)K_I(t) + K_{22}(\theta)K_{II}(t) \quad (2.42)$$

Where the  $K_{ij}$  are analytical coefficients, which can be obtained by:

$$K_{11}(\theta) = \left(\frac{1-m}{1+m}\right)^{\frac{m}{2}} \left(\cos \theta - \frac{1}{2\pi} \sin L\theta\right) \quad (2.43)$$

$$K_{12}(\theta) = \left(\frac{1-m}{1+m}\right)^{\frac{m}{2}} \left(-\frac{3}{2} \sin \theta\right) \quad (2.44)$$

$$K_{21}(\theta) = \left(\frac{1-m}{1+m}\right)^{\frac{m}{2}} \left(\frac{1}{2} \sin \theta\right) \quad (2.45)$$

$$K_{22}(\theta) = \left(\frac{1-m}{1+m}\right)^{\frac{m}{2}} \left(\cos \theta + \frac{1}{2\pi} \sin L\theta\right) \quad (2.46)$$

Where  $m = \theta/180$  and  $L = \ln\left(\frac{1-m}{1+m}\right) - 2\left(\frac{m}{1-m^2}\right)$ . And the  $\Delta K_I^*(\theta)$  is the difference between  $K_I^*(\theta, t)$  at maximum and minimum loads. Dubourg and Lamacq [196] introduced this method into rolling contact fatigue and achieved good results in crack growth direction prediction compared

with experimental observations. Ribeaucourt, Baietto-Dubourg [195] studied the rolling contact fatigue problem under the effect of the contact interaction between the crack interface. Their results combined with Hourlier's criteria were consistent with the results obtained from the reference model. More intuitively, Pereira and Wahab [50] studied the fatigue problems of proportional and non-proportional loads, respectively, through numerical methods. The proportional load case is uniaxial tensile fatigue with oblique crack whose  $K_I/K_{II}$  ratio is constant in one cycle. The fretting fatigue model is considered as the non-proportional load case. The results showed that for the problem of proportional load, the traditional MTS and  $K_{II} = 0$  criteria and the maximum  $\Delta K_I^*(\theta)$  criteria had the same predicted crack propagation direction. However, for non-proportional loading, variable ratio  $K_I/K_{II}$  resulted in the orientation corresponding to the maximum tangential stress at different time was different. The orientation with the maximum  $\Delta K_I^*(\theta)$  corresponded to the direction with the minimum  $\Delta K_{II}^*(\theta)$ . And the maximum  $\Delta K_I^*(\theta)$  criteria provided much reasonable crack propagation path prediction of fretting fatigue than the MTS, MERR and  $K_{II} = 0$  criteria compared with experimental results [45, 50].

#### 2.3.4.3 Numerical framework for crack propagation

The initial crack position and orientation are obtained by the critical plane method, and the initial length is obtained by Eq. (2.16). After determining the crack growth rate by Paris-Erdogan equation and equivalent SIF

range, crack growth direction criteria can be obtained from the Maximum  $\Delta K_I^*(\theta)$  criteria. Using finite element technology, a numerical framework for fretting fatigue crack growth prediction can be established. And the flowchart of fretting fatigue crack growth analysis based on fracture mechanics is shown in Figure 2.23.

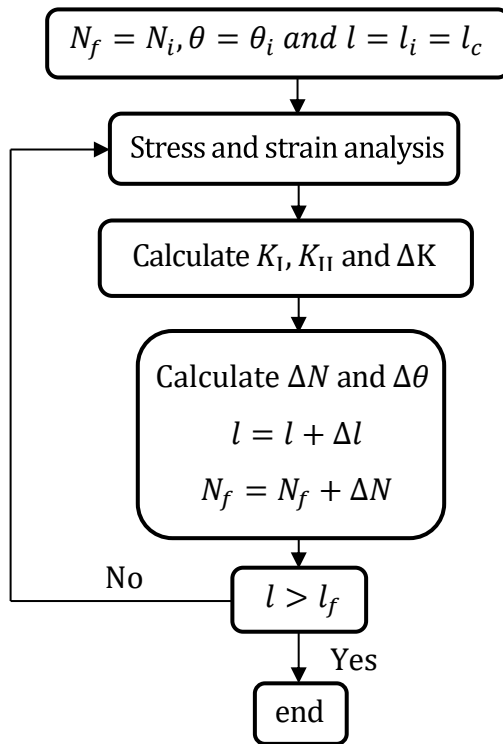


Figure 2.23. The flowchart of fatigue crack growth analysis based on fracture mechanics.

## 2.4 Summary

In this chapter, the contact mechanics of fretting fatigue is reviewed, at first. The contact stress of two parallel cylinders under normal loading given by the classical Hertzian solution is introduced. Furthermore, when combining the effect of normal and tangential loads, the contact will change to partial slip contact. The Coulomb friction law is used to solve the shear stress, and the model will become a fretting fatigue problem as the axial load  $\sigma_{axial}$  is considered. The formulas of eccentric displacement of contact zone and shear stress of contact surface are introduced. After that, the effects of micro defects (inclusion and void) and macro geometry (surface geometry and stop hole) on fatigue crack initiation and propagation are reviewed also.

The analytical results mentioned above are based on some assumptions. It is not necessarily suitable for different loads and geometries. Therefore, the experimental and numerical studies of fretting fatigue are reviewed. From the experiment, it is observed that the crack normally initiated from the contact edge of the surface. At the initial stage of crack propagation, the path inclined to contact the surface, which is affected by the contact stress. When the crack growth is enough deep, the crack path is perpendicular to the contact surface. However, the stress and strain fields at the contact surface and below area are obtained by FEM simulation which can provide more information than experimental study. The

---

influence of inclusions and micro-voids on the macro material properties of specimen is considered through RVE method.

The using of CP parameter and TCD method to predict crack initiation life is discussed. For the surface pit treatment specimen, in order to consider the effect of slip amplitude, the Ruiz parameter is introduced. And a review of the application of LEFM in fretting fatigue crack propagation is presented. Different equivalent SIF range and crack propagation direction prediction formulas are introduced. Finally, the framework for predicting crack initiation location, life, crack propagation path and life is presented. After combing these background knowledge, the main purpose of this thesis is to study the influence of microstructure and macrostructure on the initiation and propagation of fretting fatigue cracks.

## **Chapter 3      Randomly      distributed inclusions**

Analysis of fretting fatigue plays an important role in many engineering fields. Generally, micro cracks are observed inside the slip zone and at the contact edge. The presence of heterogeneity may affect the performance of a machine or a structure, including its lifetime and stability. So, both fretting fatigue and heterogeneity may significantly influence the lifetime and stability of mechanical components. The macroscopic fatigue failure occurs due to the distribution of micro-stress. In the literature, homogeneous materials are widely assumed to study fretting fatigue problems[53]. However, only a few studies have considered the heterogeneity of material under fretting fatigue conditions [53, 197, 198]. In this chapter, the effect of randomly distributed micro inclusions on fretting fatigue behaviour of heterogeneous materials is analysed using Finite Element Method (FEM) for different sizes, shape and properties of inclusions. The effect of micro inclusions on macroscopic material properties is also considered by representative volume element (RVE). It is shown that the influence of micro inclusions on macroscopic material properties cannot be ignored, and the shape and size of the inclusions

have less effect on the macroscopic material properties compared with the material properties of inclusion and volume ratio. And various parameters of inclusions have little effect on the peak value and position of the tensile stress, it is kept almost the same as homogeneous material. Wherever the peak of shear stress occurs, high-amplitude shear stress occurs in many places inside the specimen, which can result in multiple cracking points occurring inside the sample as well as contact surface. Moreover, the stress band formed by the stress coupling between adjacent inclusions has an important influence on the direction of crack propagation in the later stage.

### 3.1 Finite Element Model and Validation

From Figure 3.1, we can see the experimental setup by a schematic view [45] for a contact of two cylindrical pads and a flat specimen. Under the action of normal load  $F$ , the two fretting pads maintain contact. In addition, the coefficient of friction between the contact surfaces is 0.65 [45]. The cyclic axial load  $\sigma_{axial}$  is acting on the right side of specimen. Two springs are attached to the fretting pad, which will generate the tangential load  $Q$ , under the combined effect of these loads, so that fretting fatigue will occur around the contact area.

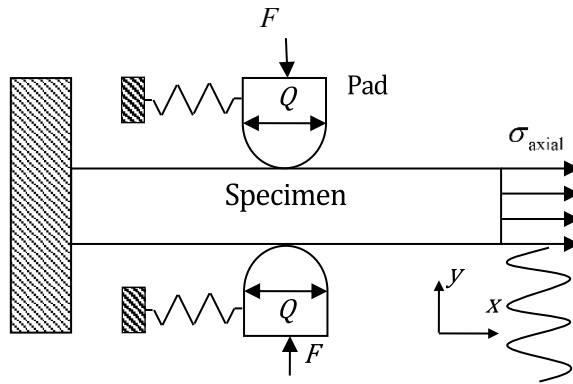


Figure 3.1. Schematic view of fretting fatigue experimental setup [25].

Because geometries and loads are symmetric, a simplified model of the structure can be constructed, which is one pad and half of the specimen. Same as previous researchers [9, 10, 33, 53], we can model the load and boundary conditions as shown in Figure 3.2.

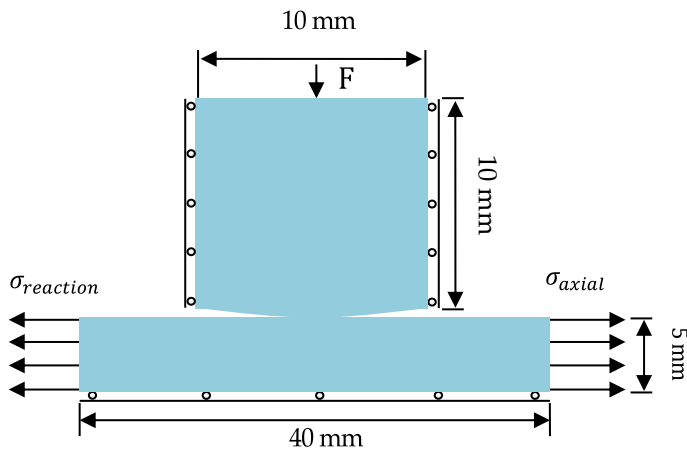


Figure 3.2. Configuration of the fretting fatigue numerical model.

The radius of the pad and width of the specimen are taken from Ref [45]. As it is shown in Figure 3.2, the length of the specimen is 40 mm and the width is equal to 5 mm. In addition, the thickness of two bodies and the radius of cylindrical pad are 4 mm and 50 mm, respectively. At the top surface of the cylindrical pad, we apply a normal load  $F$  and convert it to average pressure  $p$ . The pad is restrained from both sides in  $x$ -direction. On the right hand-side and left hand-side of the specimen, an axial stress  $\sigma_{axial}$  and a reaction stress  $\sigma_{reaction}$  are applied, respectively. The value of  $\sigma_{reaction}$  is given by [199]:

$$\sigma_{reaction} = \sigma_{axial} - \frac{Q}{A_s} \quad (3.1)$$

Where  $Q$  is the tangential force between the contact surfaces. In addition, the cross-section area of the specimen is expressed as  $A_s$ . The bottom side of the specimen is fixed in the  $y$ -direction. In order to verify our FE model and study the effect of inclusions on fretting fatigue, the experimental data used in this paper is taken from the work of Talemi and Wahab [45]. In this study, in both validation models and parametric studies, the FF 2 [45] load case has been used, with  $F = 543\text{N}$ ,  $\sigma_{axial} = 115\text{MPa}$ ,  $Q_{max} = 186.25\text{N}$ .

As described in the previous chapter, we consider the heterogeneity of materials by representative volume element method using DIGMAT-FE as shown in Figure 2.11. In this way, we can get the macro material

properties (Equivalent elastic modulus  $E^*$  and Equivalent Poisson's ratio  $\mu^*$ ) that consider the effect of microscopic inclusions [200-203]. Here, we just consider the elastic material response, because for all specimens with inclusions, von-Mises stress is always below the yield limit under such loading conditions. This is common in fretting fatigue problems. According to the previous literature, the original material properties of Aluminium alloy 2024-T3 [45],  $Al_2CuMg$  [204] and  $Al_2O_3$  [205] in this paper are present in Table 3.1. And this article assumes that the cylindrical pad is a homogeneous Aluminium alloy 2024-T3.

Table 3.1. The original material properties involved in this paper.

Material	Modulus(GPa)	Poisson's ratio
Aluminum alloy 2024-T3	72.1	0.33
$Al_2CuMg$	120.5	0.1999
$Al_2O_3$	380	0.2

According to SEM study by AliMerati [92], here 2%, 4%, and 6% volume ratio  $v$  between inclusions and matrix material were chosen. From the experimental observation by T. Hashimoto[206] and other FEM research about the inclusion [62, 206]. We consider the inclusions as idealized spherical and ellipsoid with 23  $\mu m$  to 65  $\mu m$  diameter, perfectly bonded with matrix material. Due to the randomness and uniformity of inclusions distribution, the RVE is constructed as a cube that is subject to periodic boundary conditions. In order to study the effect of inclusion size, here for same case each inclusion has a uniform size. But cases with randomly

distributed inclusion sizes will also be discussed in the end. As an example, a RVE with spherical  $Al_2O_3$  inclusions, 65  $\mu m$  diameter, and 6% volume ratio has been study at first as shown in Figure 3.3. The RVE cube with randomly distributed inclusions is built by DIGMAT-FE. The minimum relative distance between inclusions is equal to 5% relative to inclusion diameter. The periodic geometry and periodic boundary condition are also satisfied, so that the RVE cube can represent the macro properties of the whole material.

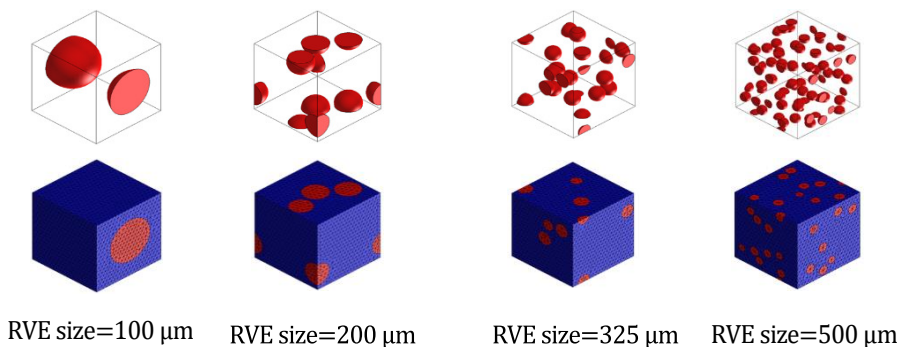


Figure 3.3. Four different size RVEs and corresponding mesh models.

This case has the strongest inclusions, and the convergence of RVE size is studied for it. 4 kinds of different size RVEs and corresponding mesh models are shown in Figure 3.3. And for the convergence research 9 kinds of size have been calculated and the corresponding macro material properties are shown in Figure 3.4. When the RVE size reaches 325  $\mu m$  the macro elastic modulus will keep around 78.84 GPa and Poisson's

ratio will keep around 0.324 and relative difference from adjacent results is less than 1%. So, the convergence RVE size of this case is 325  $\mu\text{m}$  and it can be applied to all other cases. In order to be safe, each case has been calculated three times, and then the average of the results is taken. In this way can get the macroscopic material properties of a specific heterogeneous Aluminium alloy.

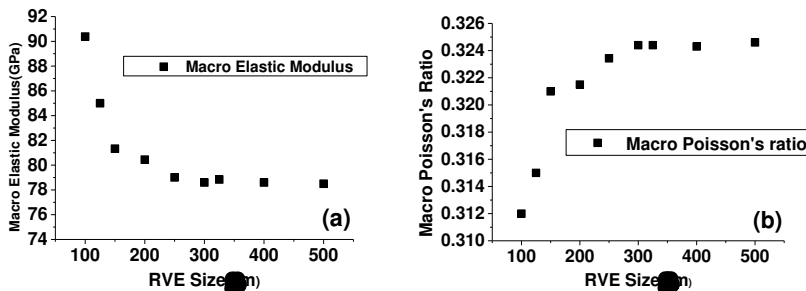


Figure 3.4. Convergence of (a) Macro elastic modulus and (b) Poisson's ratio

For comparative research, all the cases involved in this study are given in Table 3.2. The aspect ratio describes the evolution of inclusion from sphere to ellipsoid. And the size refers to the diameter of the ball or the length of the long axis of the ellipsoid. In case 7 and case 8, we consider the ellipsoid inclusion and in order to control them have the same cross-sectional area as the spherical inclusion with a diameter of 44  $\mu\text{m}$ , the long axis length of the ellipsoid are converted to 53.889  $\mu\text{m}$  and 62.225  $\mu\text{m}$ , respectively. From the results of case 3 and case 5 to 9, it can be seen that the macroscopic material properties have little to do with the

size and shape of inclusions. The numerical and experimental researches about the composite show similar conclusions [207, 208]. However, compare case 1 with case 3, it shows the material properties of inclusion have a significant impact on macro elastic modulus. For the same reason, comparing case 3, 4, 5, shows that the volume ratio of inclusion also obviously affects the macroscopic material properties. And the macroscopic Poisson's ratio has hardly changed. It is worth noting that the above conclusions are only applicable to the cases in Table 3.2.

Table 3.2. All the cases involved in this study.

Number	Volume ratio	Type	Size( $\mu\text{m}$ )	Aspect ratio	$E^*$ (GPa)	$\mu^*$
Case 1	4%	$Al_2CuMg$	44	1	73.7005	0.32584
Case 2	2%				74.269	0.32791
Case 3	4%	$Al_2O_3$	44	1	76.615	0.32579
Case 4	6%				78.2946	0.3243
Case 5	4%	$Al_2O_3$	23	1	76.5524	0.32503
Case 6	4%	$Al_2O_3$	65	1	76.5046	0.32537
Case 7	4%	$Al_2O_3$	53.889	1.5	76.318	0.3256
Case 8	4%	$Al_2O_3$	62.225	2	76.163	0.32255
Case 9	4%	$Al_2O_3$	23 to 65	1	76.2028	0.32532
Case 10	4%	Void	44	1	69.1	0.327

According to the contact width for all load cases in an experiment [45] is 0.47 mm and calculation results from Kumar [53], the 2 mm  $\times$  2 mm area near the contact interface is the main field of stress concentration. As described in the previous chapter, so 2 mm  $\times$  2 mm rectangle will be chosen as the size of Area 1 in Figure 2.12. The simulation study in this paper is divided into two parts. The first part is the simulation of the nine

inclusion structures in Table 3.2 which has completely randomly distributed inclusion. Some conclusions will be described in the next section. For the second part, since the inclusion locations of each case are randomly generated, each case cannot have the same inclusion order. This makes it impossible to use the control variable method to explore the effect of the shape, size and position of the inclusion on the contact stress distribution. So, we artificially placed four inclusions below the sample contact area to compare the effects of different inclusions on the surface stress distribution. These inclusions vary in size, shape, and material corresponding to different cases. The parametric 2D finite element model is created in ABAQUS [209] using Python script. High order elements always cause instability in the stress value on the contact surfaces [210]. Therefore, we chose CPE4R element (plane strain element, 2D, four nodes) instead of eight-node element to mesh both parts. Figure 3.5 shows a completed finite element model, corresponding to case 3 in Table 3.2. And for homogeneous case, the total number of elements is 64510.

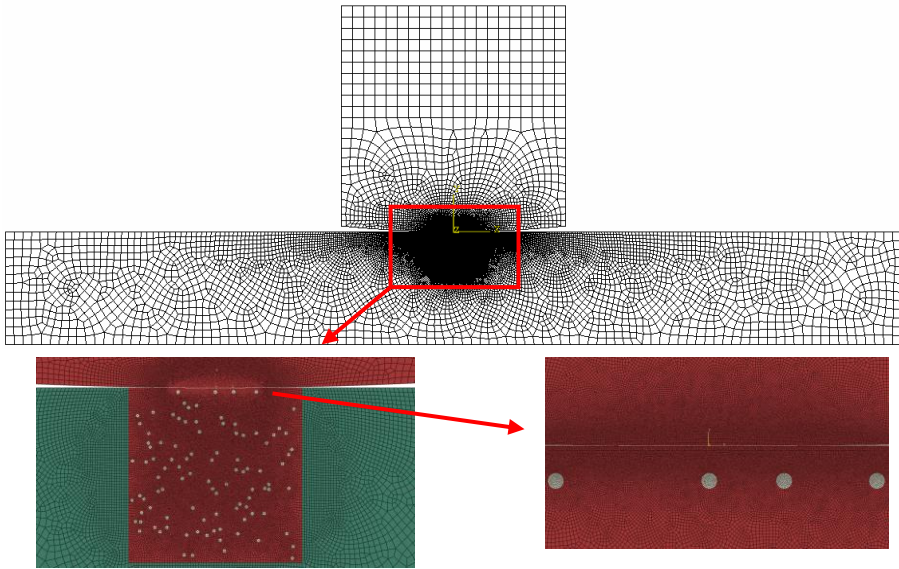


Figure 3.5. Finite element model of case 3 with artificially placed four inclusions.

As shown in Figure 2.6, the stress distribution in contact region is very complicated and stress amplitude is large. In particular, near the border between slip and stick zone, it changes very rapidly. In order to get precisely the stress distribution and contact stresses, the model is refined near the region of contact and inclusions. The boundary and loading conditions are as described at the beginning of this section. And the contact behaviour is described by master-slave algorithm. A Lagrange multiplier is used to establish the contact between the pad and the specimen. The slave surface is defined on the top surface of the specimen and the master surface is defined on the bottom surface of the pad. For

homogeneous material, the stress distribution at the contact interface can be obtained analytically, if the assumptions of the Hertz solution are met. The most important two assumptions are: (a) pure elasticity prevails and (b) the size of the contact area is small enough relative to both contact bodies. The first assumption is met as only linear elasticity is considered in this study. The second one is also called half-space assumption [22]. The contact width for all load cases in the experiment presented in Ref [45] is 0.47 mm, which is less than one-tenth of the height (5 mm) of the sample. A comparison between analytical solution Eq.(2.13) and simulation results with different mesh sizes, for the case of homogeneous material, is shown in Figure 3.6 (a). Element sizes of 5  $\mu\text{m}$ , 3  $\mu\text{m}$  and 2  $\mu\text{m}$  around the contact zone have been chosen for the convergence study. The mesh refinement showed convergence towards the peak analytical solution for the shear traction. Finally, according to the results, 2  $\mu\text{m} \times 2 \mu\text{m}$  element size is used around the contact zone, which is smaller than in previous numerical studies [9, 10, 30-35]. The simulation results and the theoretical results may not be exactly the same, due to numerical errors and geometric constraints [211]. However, the difference between the simulation and the analytical solution is less than 2% (green line and red line in (a)), which can be considered good enough to validate our FE contact model.

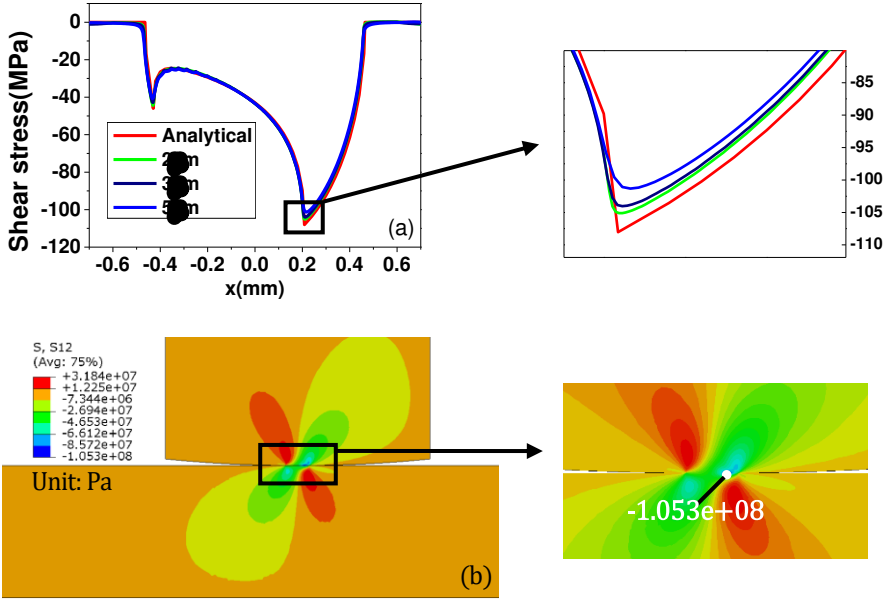


Figure 3.6. (a) Mesh sensitivity diagram (effect of mesh refinement on shear stress distribution on contact interface) and (b) shear stress distribution near contact interface for a homogenous case with 2 μm contact element size.

The accuracy of the stress near the inclusion is also studied through element size convergence. As an example (case 4) shown in Figure 3.7 (a), the peak Mises stress location is locked by a rough mesh model. Then the accuracy of stress is increased by halving the element size. Until the stress difference between two iterations is less than 1% as shown in Figure 3.7 (b) and (c), the penultimate element size will be used for the final mesh scheme. Although the use of RVE method greatly increases the computational efficiency, however, due to the existence of inclusions near

the contact area, the number of elements here will exceed the homogeneous case. For instance, the total number of elements in case 1 is 97391.

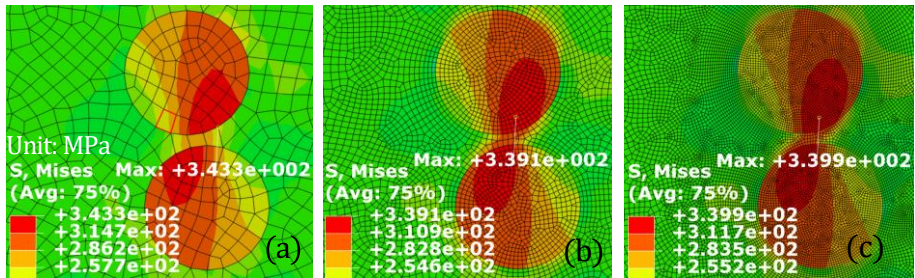


Figure 3.7. Element size convergence of inclusions.

## 3.2 Completely randomly distributed inclusion

### 3.2.1 Stress peak and its position

There are many experimental studies [64, 92, 98, 212] and numerical studies [62] on the fatigue problem of heterogeneous materials. But the numerical research on fretting fatigue of heterogeneous materials is not a lot [53]. So, the first part of our research is to study the cases with random distribution inclusions. In real metal materials, inclusions and defects are common and randomly distributed. In the fretting fatigue problem of homogeneous materials, the peak of shear stress appears between the stick zone and the slip zone, as shown in (b). The peak tensile stress and peak Mises stress in the whole specimen appear near the edge of contact [9]. For our experimental materials and loading conditions, the point of

occurrence of Mises stress and tensile stress peaks is  $x = 0.47$  mm, the shear stress peak is occurred at  $x = 0.21$  mm on the contact surface. But for the heterogeneous materials with randomly distributed inclusions in this Chapter (Table 3.2), significant stress concentration inside the specimen, as shown in Figure 3.8. It is the stress distribution below the contact surface of the specimen. It can be seen from comparison Figure 3.8 (c) with (b) that the shear stress peak is transferred from the contact surface to the inside of the specimen in the heterogeneous situation. It also showed that there may be multiple high stress points (the points around peak value) inside the structure. Thereby forming an influencing group of intrusions, eventually causing multiple fatigue cracking points inside the material as observed in the experiment [92].

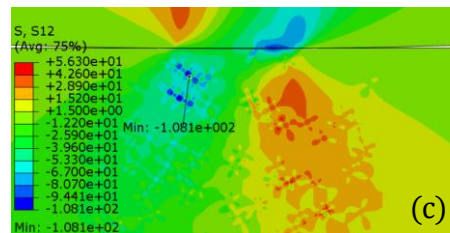
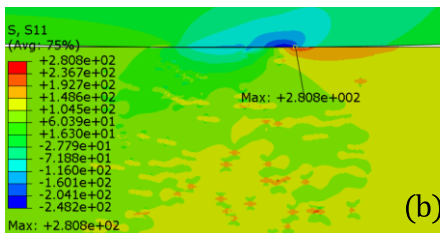
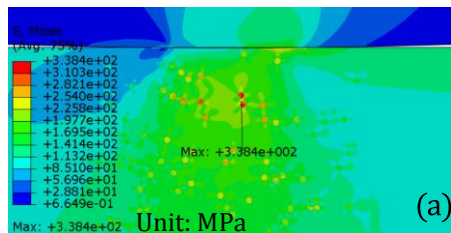


Figure 3.8. Stress distribution of Case 3 below the contact surface (a) Mises stress (b) Tensile stress and (c) Shear stress.

Due to the complete randomness of the inclusion distribution, it is difficult to investigate the effect of particle size, shape and other factors on the stress distribution by the control variable method. Such as maintain the same inclusion material, shape, size but different volume ratio (case 2, 3, 4) to study the effect of volume ratio on the surface stress distribution of the sample. There is no regularity in the results, that is, the stress peak is almost determined by the critical defects in each case. It is similar to the experimental observation, the size of the particles is not necessarily related to the fatigue life [92].

So, we can only extract the distribution of stress extreme values based on the completed simulation calculation, as shown in Figure 3.9.

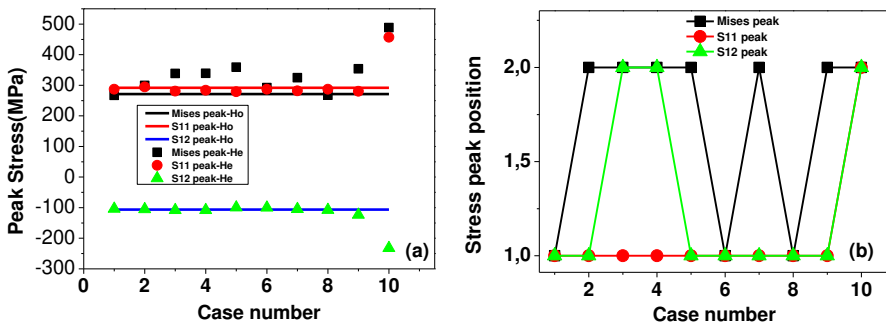


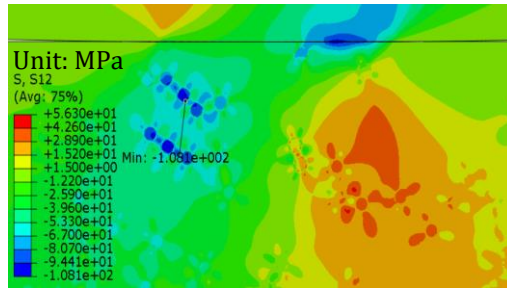
Figure 3.9. (a) Comparison of stress peaks between heterogeneous materials and homogenous materials and their (b) location of all cases

Although many kinds of parameters (type, volume ratio, size, shape) of inclusions are considered on the fretting fatigue numerical model, the data from Figure 3.9 (a) indicates that tensile stress  $S_{11}$  and shear stress  $S_{12}$  are similar to homogeneous materials except for the Mises stress which is significantly higher than the case of homogeneous materials. As shown in Figure 3.9 (b), if the stress peak location is the same with homogeneous specimen on the contact surface as mentioned before, the ordinate value is equal to 1, otherwise (below the contact surface), equal to 2. From those two figures, we can know that, for fretting fatigue problem, heterogeneous materials containing randomly distributed inclusions have almost the same tensile and shear stress peaks and locations as homogeneous materials on the contact surface. Due to the presence of hard inclusion, the equivalent elastic modulus of the material becomes larger, resulting in a situation where the stress peak in heterogeneous material is sometimes even lower than that of the homogeneous material. But at the same time, the shear stress inside the specimen is also relatively large, comparable to peak value on the surface. Therefore, for materials with shear stress as the main fatigue index, it is likely that cracks will occur simultaneously on the surface as well as inside (Figure 3.8(c)). But the Mises stress will be increase and appears below the contact surface with a high probability. Moreover, we can notice the Case 10 which use voids instead of inclusions, all of the three kinds of stress peak are significantly increased and appear inside the specimen

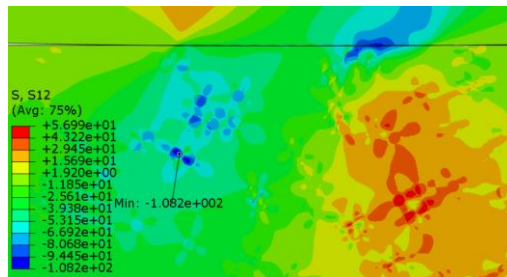
near the edge of voids. And the Mises stress even beyond the yield limit 383 MPa. This confirms experimental observations, the porosity is the main cause of fatigue damage, followed by oxide [64] and provides more useful results data.

### 3.2.2 Stress peak position characteristic

From Figure 3.9 (b) we can see the shear stress will randomly appearing inside or on the surface of the material. Figure 3.8 (c) indicates that there will be multiple cracking points appearing on the surface or inside the material because both have roughly the same shear stress. For homogeneous materials, the peak value of shear stress appears on the contact surface, but on the left side of sample inside, the shear stress is also in a relatively high state as shown in (b). So, when there are inclusions in the material, the peak value of shear stress is likely to transfer to this area (Left side of sample inside). The local inclusion alignment of the stress peak location of case 3 and case 4 are shown in Figure 3.10. So this shows that the inclusion in the high stress region is more likely to cause the transfer of stress peaks from the surface to the inside. Moreover, the effect of mutual coupling between the inclusions. Forming a stress band between the inclusions, which will directly affect the expansion direction of the crack later.



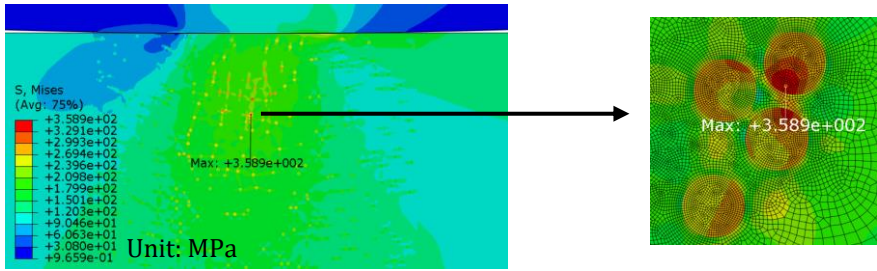
(a)



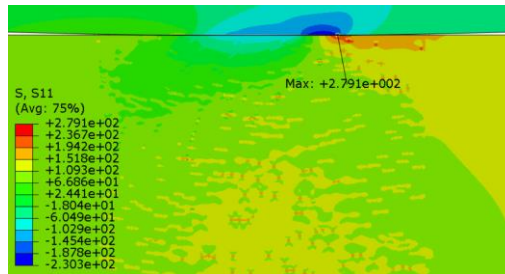
(b)

Figure 3.10. The local inclusion alignment of the shear stress peak of (a) case 3 and (b) case 4.

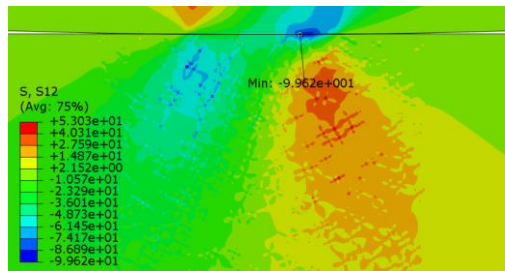
In all cases, except for the case of void (case10), case 5 has the largest Mises stress. And the local inclusion alignment of the stress peak location of case 5 is shown in Figure 3.11(a). Stress coupling between the inclusions also appears here, and smaller and denser inclusions form a more pronounced stress band as shown in Figure 3.11.



(a)



(b)



(c)

Figure 3.11. Stress distribution of Case 5 below the contact surface (a) Mises stress (b) Tensile stress and (c) Shear stress.

### **3.3 Randomly distributed and manually placed inclusions**

After observing the preliminary analysis of the effects of phenomena on inclusion, we artificially placed four inclusions below the contact surface of the specimen for each case shown in Figure 3.5. The geometric centre is zero, and the abscissa corresponding to the four inclusions is -0.43, 0, 0.21, 0.47. These four points correspond to the two peaks of shear stress, the geometric centre and the contact edge point. As for the vertical position, their original position is 100  $\mu\text{m}$  below the specimen surface. In order to research the effect of inclusion on the contact surface stress distribution, the size and shape of inclusions are corresponding to each case.

#### **3.3.1 Effect of inclusions type**

As commonly known there are many kinds of inclusions inside metallic material depends on the process of smelting and late-out impurities. Here we consider two different inclusions by comparing case 1 and case 3 (Table 3.2).

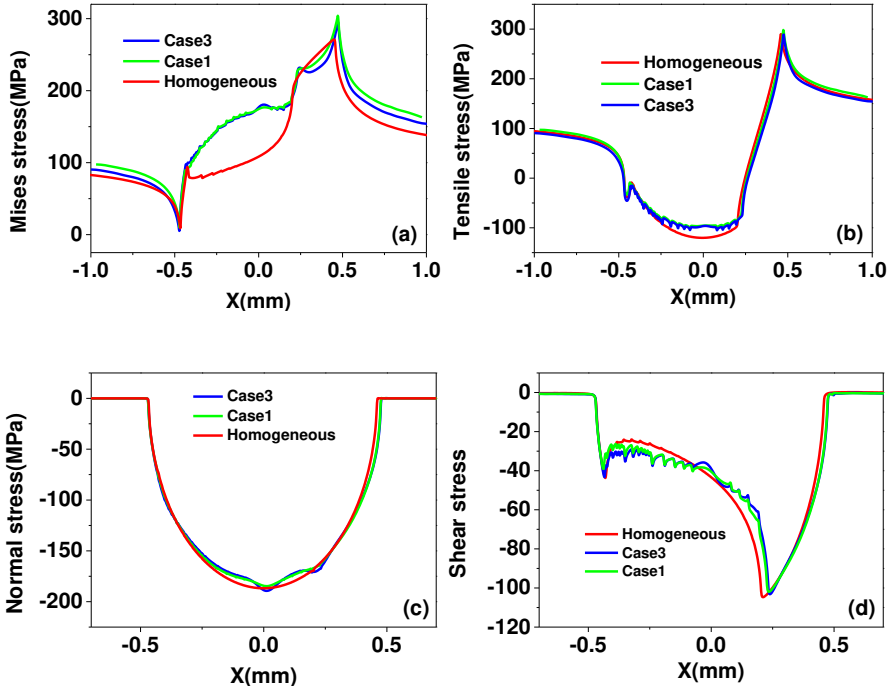


Figure 3.12. (a) Mises stress (b) Tensile stress (c) Normal stress (d) Shear stress distribution on the contact surface for different inclusion materials cases.

As we can see in Figure 3.12(a), in both homogenous and heterogeneous specimen, the Mises stress peak is near the contact edge. And it changes very sharply near the edge of the contact. The presence of inclusions makes the peak of the Mises stress increase significantly, and  $Al_2CuMg$  has a more obvious effect than  $Al_2O_3$ . It means in the heavy load condition, the presence of inclusions will accelerate the plastic yielding of the contact edge of the fretting fatigue contact member. The effect of

inclusion on the surface tensile stress is not obvious. But the inclusion will disturb the normal and shear stress.

### 3.3.2 Effect of distance from surface

The volume ratio (case 2,3,4) is not easy to measure for a single or several inclusions, so here we refer to the volume ratio as the particle crowding, which is reflected here as the distance between the inclusion and the contact surface. So here for case 2, case 3, case 4 distance between the centre of the particle to the surface is  $120\ \mu\text{m}$ ,  $100\ \mu\text{m}$ ,  $80\ \mu\text{m}$ , respectively. The results are shown in Figure 3.13.

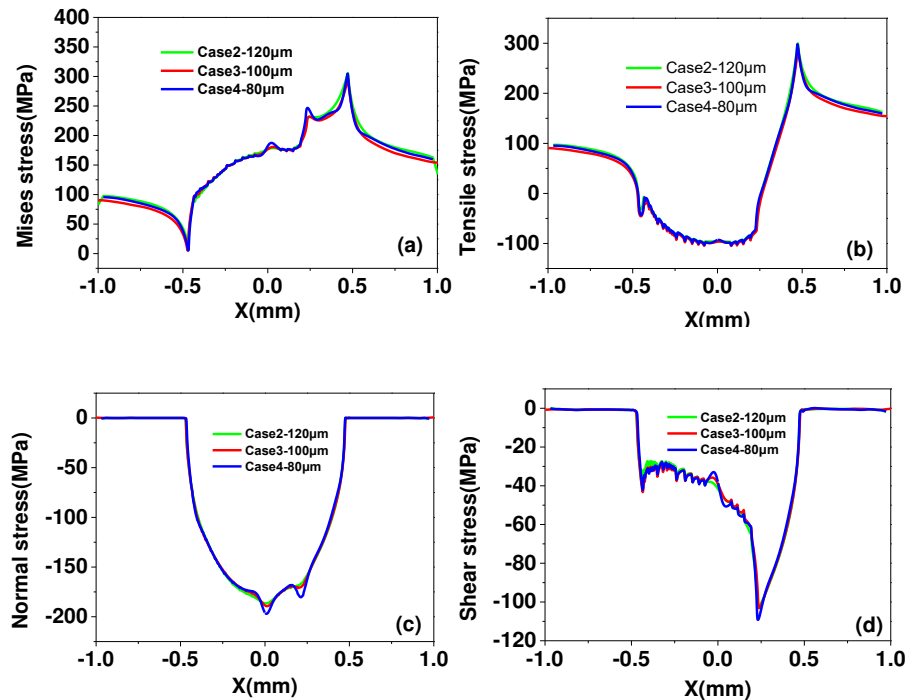


Figure 3.13. (a) Mises stress (b) Tensile stress (c) Normal stress (d) Shear stress distribution on the contact surface for different distance cases

In the experimental study[98], the authors believe that the distance between the inclusions or the distance from the surface of the defect is important for fatigue damage. From our results, it is clear in Figure 3.13, the distance from the surface has a more significant effect on the shear stress and normal stress. The smaller the distance from the surface, the greater the peak value of the shear stress generated. However, it can also be seen that the influence of the depth on the surface contact stress distribution is different for the inclusions at different lateral positions.

### 3.3.3 Effect of inclusion size

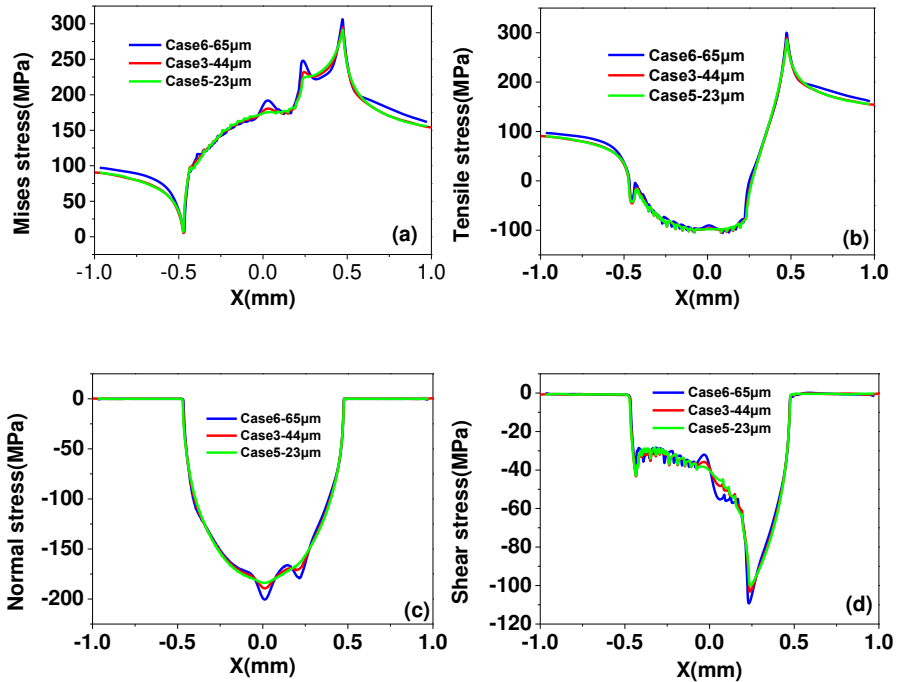


Figure 3.14. (a) Mises stress (b) Tensile stress (c) Normal stress (d) Shear stress distribution on the contact surface for different inclusion size cases

From Figure 3.14 we can find the effect of the inclusion size is more pronounced than the influence of the inclusion type on the surface stress distribution (Figure 3.12).

## 3.3.4 Effect of inclusion shape

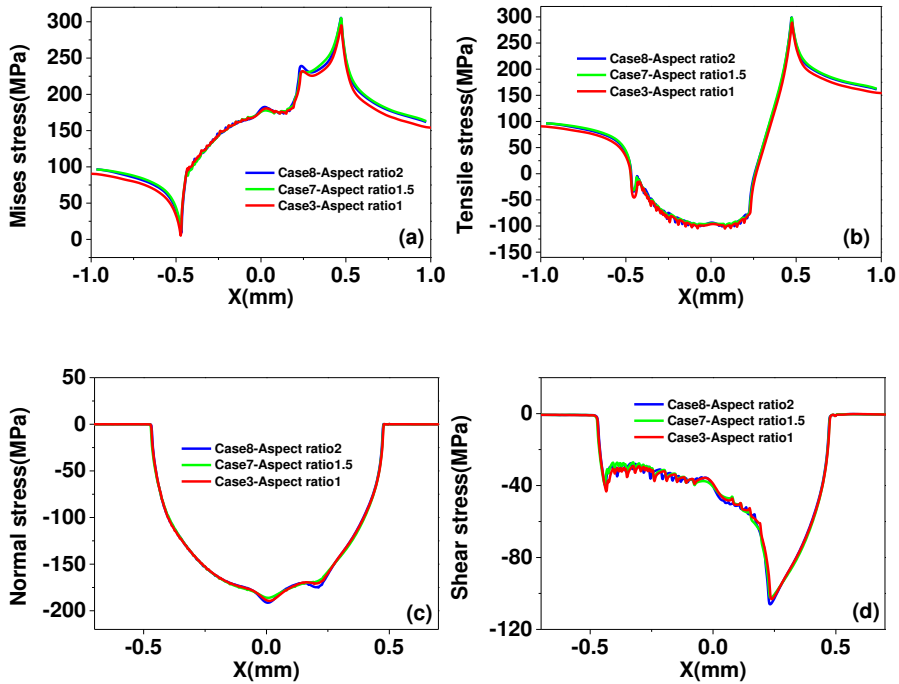


Figure 3.15.(a) Mises stress (b) Tensile stress (c) Normal stress (d) Shear stress distribution on the contact surface for different inclusion shape cases

Here we consider the effect of different aspect ratio of inclusions. But as shown in Figure 3.15, there has not too much difference between inclusion shape cases. And for all cases in this part, the effect of inclusion parameters on the tensile stress is very inconspicuous. This is similar to the phenomenon in the previous chapter.

### 3.4 Summary

In this study, in order to consider the effect of inclusions in Aluminium alloy 2024-T3 on the fretting fatigue stress distribution, a numerical research method combining RVE with finite element is proposed. Based on the research results, we can draw the following conclusions.

For the cases in this study, if under the same inclusion material to volume ratio, the shape and size of the inclusions have little effect on the macroscopic material properties. But the material properties of inclusion and volume ratio have a significant impact on macro elastic modulus. And the macroscopic Poisson's ratio has hardly changed as the change of different parameters.

Due to the randomness of the inclusion distribution, the fatigue cracking nucleation depends on the most dangerous key inclusion. The Mises stress peak very likely increases and transfer from the contact surface into inner of the specimen. But various parameters of inclusions have little effect on the peak value and position of the tensile stress, it is kept almost the same as homogeneous material. Among the materials with inclusions, the peak value and position of the shear stress are consistent with the homogeneous material, but sometimes it is also transferred to the inside of the specimen. Moreover, in all cases, high-amplitude shear stress occurs in many places inside the sample which can result in multiple cracking points occurring inside the sample as well as a contact surface.

---

Due to the presence of hard inclusion, the equivalent elastic modulus of the material becomes larger, resulting in a situation where the stress peak in heterogeneous material is sometimes even lower than that of the homogeneous material. Void compared to inclusion will cause more large stress and randomness of stress distribution. Therefore, the influence of microstructure on macroscopic material properties should be considered in engineering.

Inclusion in high stress areas is more likely to cause stress concentration leading to peak transfer. And stress coupling between adjacent inclusions will form a high stress band, which has an important effect on the direction of crack propagation.

The size of the inclusion and the distance from the surface have a more significant effect on the surface stress distribution than the type and shape of inclusion. And the effect of inclusion parameters on the tensile stress is very inconspicuous.

## **Chapter 4     The effect of critical micro-void on the crack initiation**

Fretting fatigue problems are common in the aerospace and automotive industries, which can seriously affect the fatigue response of the material and the stability of the overall structure. However, the research on the influence of material heterogeneity on fretting fatigue is relatively scarce [53, 197, 198]. Therefore, the heterogeneity of critical micro-voids is worth studying. In this paper, the effect of the size, location of single critical micro-void on the fretting fatigue initiation life of heterogeneous materials is studied by numerical simulation and modified critical plane criterion. The theory of critical distance (TCD) is used to consider stress gradients near the crack initiation points. It is shown that when the critical micro-void is located at different positions inside the sample, there is a weakened area similar to the half butterfly wings. This means that when the micro-voids are located in this area, the crack initiation life will be less than that in the case of homogenous material. Furthermore, there are also two enhancement zones. When the micro-voids are located in these two zones, the fretting fatigue life can be increased, that is, at a certain depth

below the contact edge and a certain distance to the right of the contact edge.

## 4.1 Experiment data

The experimental data in this article comes from the research work conducted in our research group by Hojjati-Talemi et al. [25]. The servo-hydraulic load frame is used to execute the fretting fatigue test considering a cylindrical pad on a flat specimen. A simplified structure of the fretting fatigue experimental device is shown in Figure 3.1 as present in the last chapter. Both cylindrical pad and specimen are made from Aluminium 2024-T3. This kind of material is widely used in the aviation industry because of its good fatigue characteristics. The specific chemical composition of the material is listed in Table 4.2.

Table 4.1: The chemical composition of the Al2024-T3 [45]

Al 2024-T3	Al	Si	Fe	Cu	Mn	Mg	Cr	Zn	Ti	Others
Max	Base	0.5	0.5	4.9	0.9	1.8	0.1	0.25	0.15	0.05
Min				3.8	0.3	1.2				

The stress ratios of  $\sigma_{axial}$  and tangential force  $Q$  are 0.1 and -1, respectively. The detail about the tests load and life result are list in the Table 4.2. Specimens are in elastic range under all experimental loads. A uniform pressure equivalent to the top force ( $F = 543 N$ ) is applied at the top of the cylindrical pad.

Table 4.2. The fretting fatigue experiments load condition and life results [25].

Test number	$\sigma_{axial}$ (MPa)	$Q_{max}$ (N)	$N_{failure}$
1	100	155.165	1407257
2	115	186.25	1105245
3	135	223.7	358082
4	135	195.55	419919
5	160	193.7	245690
6	190	330.15	141890
7	205	322.1	114645
8	220	267.15	99607
9	220	317.845	86647

## 4.2 Multiscale numerical model

The heterogeneity of the material not only affects the local response of the region near the contact area, but also affects the overall macroscopic properties of the material. The two most common inclusions ( $Al_2CuMg$  and  $Al_2O_3$ ) and micro-voids that are ubiquitous in Aluminium alloy 2024-T3 are introduced, in order to be as realistic as possible to reflect the natural defects inside the material. The distribution, size of defects are discrete and random [59, 105].

Table 4.3. The property of all materials and defect characteristics

Material	Modulus (GPa)	Poisson's Ratio	Volume Ratio	Size ( $\mu m$ )	Aspect ratio
AA 2024-T3	72.1	0.33			
$Al_2CuMg$	120.5	0.2	1.35%	23~65	1/1.84/2.68
$Al_2O_3$	380	0.2	1.35%	23~65	1/1.84/2.68
Micro-voids			0.7%	23~65	1/1.84/2.68

The details of original material properties of Aluminium alloy [25],  $\text{Al}_2\text{CuMg}$  [213], and  $\text{Al}_2\text{O}_3$  [214] are shown in Table 3.1. Similar to previous finite element studies, the shape of all defects varies from spherical to elliptical [134, 215-217]. Three typical different aspect ratio shapes are considered [105]. The volume ratio of two kinds of inclusion, the size and aspect ratio of three kinds of defects are taken from the experimental observation average value of Aluminium alloy 2024-T3 by Merati [105]. Many small particle inclusions or voids are also observed, but the lower limit of the size considered in this paper is  $23\ \mu\text{m}$ , which is slightly larger than the Aluminium alloy 2024-T3 grain  $20\ \mu\text{m}$  [218]. The volume ratio of micro-voids of 0.7% is taken from the experimental and numerical research of Li [219].

#### **4.2.1 Representative volume element (RVE)**

The RVE units with three kinds of different defect aspect ratios and random distribution of defect size and position are shown in Figure 4.1. The size of the RVE unit ( $325\ \mu\text{m}$ ) and the element mesh ( $2\ \mu\text{m}$ ) have been studied for convergence. The result difference is less than 2% between two subsequent iterations. In order to obtain the macroscopic material properties of a specimen that has all of these shape features defects, the average of the material properties obtained from the three cases in Figure 4.1 is taken as the final equivalent macroscopic material property in this study. Therefore, considering the defect, the Poisson's ratio and equivalent elastic modulus of the heterogeneous materials are

0.325 and 72.79 GPa, respectively. Because the inclusions are harder than the matrix material can enhance the macro properties of the material. However, the micro-void will weaken the macro properties. Therefore, under the combined effect of these two effects, the difference between equivalent properties of the heterogeneous materials and matrix material is very limit. More details about RVE method have been mentioned in the previous chapter.

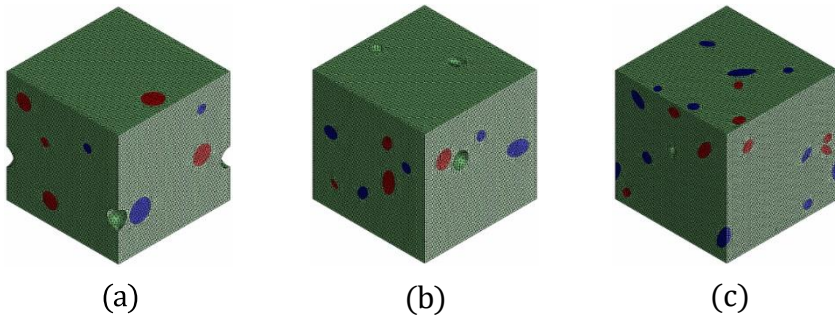


Figure 4.1. The RVE units with three different defect aspect ratios (a) 1, (b) 1.84 and (c) 2.68 with a random distribution of defect size and position.

#### 4.2.2 Macro-scale finite element model

The geometric dimensions and loading conditions of the FE model are the same as shown in Figure 3.1. And FE model for critical proe problem can be presented as shown in Figure 4.2.

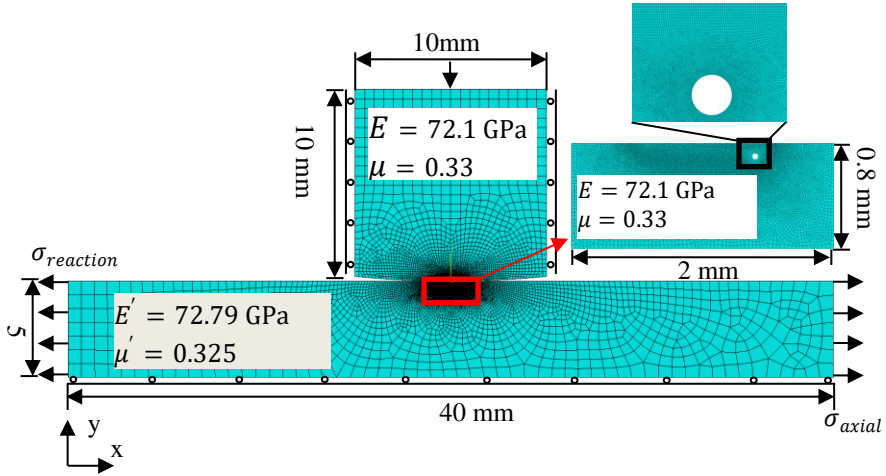


Figure 4.2. Numerical model configuration of the fretting fatigue.

Under the action of the top pressure (a uniform pressure load, which can be obtained from  $F$  and the top surface area), the system will reach equilibrium, and through the load ratio, which is equal to 0.1, all loads in the entire cycle can be obtained. As an example, the entire cycle load for test 1 is shown in Figure 4.3.

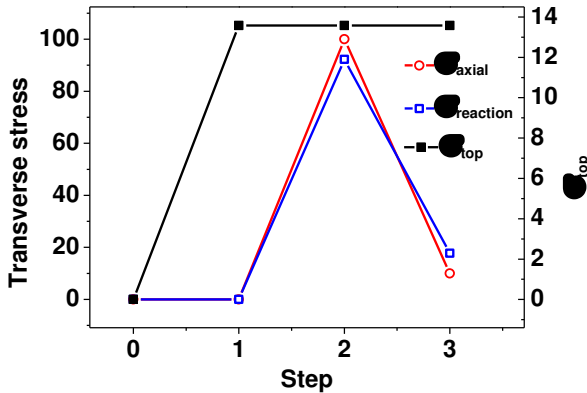


Figure 4.3. Entire cycle load for test 1

As shown in Figure 4.2, away from the portion of the contact area, the specimen is the equivalent homogeneous material, which gets from the RVE study. Under the contact surface, due to the obvious stress concentration [72, 105, 220, 221], the defect will greatly affect the crack initiation position and life, so a small rectangular area ( $2 \text{ mm} \times 0.8 \text{ mm}$ ) near the contact area is still original homogeneous aluminum alloy as shown in Figure 4.2, the red rectangle area. As mentioned in the above article, the critical micro-void has the dominant effect on the fretting fatigue initiation of the structure [24, 73]. In order to avoid the effects of too many random variables, the effects of other non-critical defects are ignored here. A single critical micro-void, which is assumed to be the most dangerous defect with different positions and sizes is introduced under the contact area. The effect of smaller voids around the critical void (porous interaction) and the comprehensive effect of several voids on the contact edge (the initiation point of the crack in the homogeneous case) will be our next study. All micro-void locations considered herein vary from 0 to 0.7 mm in the transverse direction, increasing by 0.1 mm case by case. It changes uniformly from -0.05 to -0.3 in the vertical direction, decreasing by 0.05 each time. Figure 4.2 shows the case where the critical micro-void with  $44 \mu\text{m}$  diameter locate at  $x = 0.4 \text{ mm}$ ,  $y = -0.1 \text{ mm}$ . In the finite element model, CPE4R plane strain element has been used. According to the convergence study, the mesh at the contact surface and

the critical micro-voids are well-ordered and uniform, with a size of 2  $\mu\text{m}$  and 1  $\mu\text{m}$ , respectively. The difference of contact shear stress between simulation and the theoretical solution is less than 2%.

### 4.3 Results and discussion

In order to Prediction of crack initiation location, angle, and lifetime, the first step is to extract the stress and strain history over the entire period by the simulation in the ABAQUS [222]. Then Python codes are used for post-processing to get the stress and strain values for each calculated sub-step. Not only the nodes on the contact surface are considered, but also the simulation results of the entire rectangular area below the contact surface are extracted step by step. Here is an example of using FP parameter. According to Eq. (2.17), the maximum normal stress and the shear stress amplitude in the entire period of each node in every direction determine the value of the damage parameter. The shear stress and normal stress in any direction can be converted from the lateral and vertical stresses by Mohr's cycle as shown in the following three formulas.

$$\sigma_{x'} = \frac{\sigma_x + \sigma_y}{2} + \frac{\sigma_x - \sigma_y}{2} \cos(2\theta) + \tau_{xy} \sin(2\theta) \quad (4.1)$$

$$\sigma_{y'} = \frac{\sigma_x + \sigma_y}{2} - \frac{\sigma_x - \sigma_y}{2} \cos(2\theta) - \tau_{xy} \sin(2\theta) \quad (4.2)$$

$$\tau_{x'y'} = -\frac{\sigma_x - \sigma_y}{2} \sin(2\theta) + \tau_{xy} \cos(2\theta) \quad (4.3)$$

The damage parameter values of each node on each plane are obtained. The angles of these planes range from -90 degrees to 90 degrees, which are iterated with 1 degree, covering all possible crack initiation directions at this node. Finally, from all the points on all the planes, the largest damage parameter value appears in the critical plane, so that the crack initiation position and direction can be predicted. Then the crack initiation life can be predicted by Eq.(2.19). For the other two kinds of damage parameters, the method is similar. Moreover, all material parameters for the specimen in this study involved in the above formula are list in Table 4.4.

Table 4.4. The fatigue material parameters for aluminum alloy 2024-T3 [153, 155]

Ultimate tensile strength	$\sigma_{UTS} = 506 \text{ MPa}$
Tensile yield strength	$\sigma_y = 383 \text{ MPa}$
Shear yield strength	$\tau_y = 221.12 \text{ MPa}$
Tensile fatigue limit	$\sigma_{f-1} = 114.9 \text{ MPa}$
Torsion fatigue limit	$\tau_{f-1} = 66.34 \text{ MPa}$
Tensile fatigue strength coefficient	$\sigma'_f = 835 \text{ MPa}$
Shear fatigue strength coefficient	$\tau'_f = 482.08 \text{ MPa}$
Tensile fatigue ductility coefficient	$\epsilon'_f = 0.17$
Shear fatigue ductility coefficient	$\gamma'_f = 0.2944$
Fatigue strength exponent in tension	$b = -0.096$
Fatigue strength exponent in torsion	$b' = -0.096$
Fatigue ductility exponent in tension	$c = -0.644$
Fatigue ductility exponent in torsion	$c' = -0.644$

### 4.3.1 Validation of the homogeneous model

As shown in Figure 4.3, the maximum load of test 1 defined as step 2, and the minimum load is step 3. Combined with ABAQUS and Python codes, the surface contact stress at step 2, step 3 and the distribution of three different critical plane parameters at the contact surface can be extracted by the above method, as shown in Figure 4.4 (c).

The stress distribution of step 2 is shown in Figure 4.4 (a), according to the normal stress, the contact area is from  $x = -0.468 \text{ mm}$  to  $x = 0.458 \text{ mm}$ . According to the shear stress distribution, the stick area is from  $x = -0.442 \text{ mm}$  to  $x = 0.25 \text{ mm}$ . For test 1, the  $\sigma_{axial}$  is 100 MPa, however, the peak tensile stress is 264.4 MPa, which appears at  $x = 0.456 \text{ mm}$  around the right edge of contact. This means that a strong stress concentration occurs at the right edge of contact, and the maximum stress value is much larger than the far field stress value 100 MPa. As shown in Figure 4.4 (b), the contact area of the minimum load step is from  $x = -0.46 \text{ mm}$  to  $x = 0.468 \text{ mm}$ , which is almost the opposite of the maximum load case. The stick area is from  $x = -0.332 \text{ mm}$  to  $x = 0.31 \text{ mm}$ . The peak tensile stress (167.2 MPa) appears at  $x = -0.458 \text{ mm}$  near the left contact edge, too. And it is much larger than the far-field lateral load.

In general, at load step 2 and step 3, the stress concentration occurs on both sides of the contact surface, respectively. Moreover, in the case of these two extreme loads, the contact area is between from  $x = -0.468$  mm to 0.458 and from -0.46 to 0.468, respectively. This means that the contact area of the fretting fatigue problem is dynamically changing due to the existence of periodic loads and slip zones. For the fretting fatigue problem of homogeneous material, the maximum value of each critical plane parameter is always located near the edge of contact surface [155]. Since the magnitudes of the three damage parameters vary greatly, in order to visually compare their distribution, these three parameters are dimensionless by dividing by their peak values. The distribution of dimensionless critical plane parameters is shown in Figure 4.4 (c). The peaks of FP, FS, and SWT parameter appear at  $x = 0.454$  mm,  $x = 0.452$  mm and  $x = 0.456$  mm, respectively. They are inside and close to the contact right edge of maximum load.

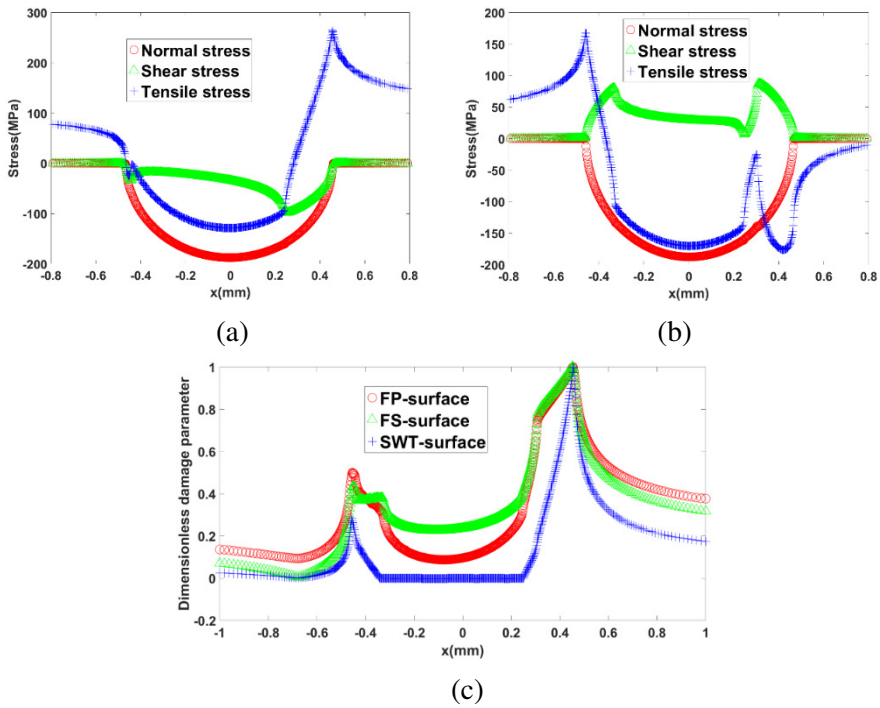


Figure 4.4. (a) Stress distribution at contact surface for maximum load step, (b) Stress distribution at contact surface for minimum load step and (c) dimensionless critical plane parameter distribution at contact surface – Test 1.

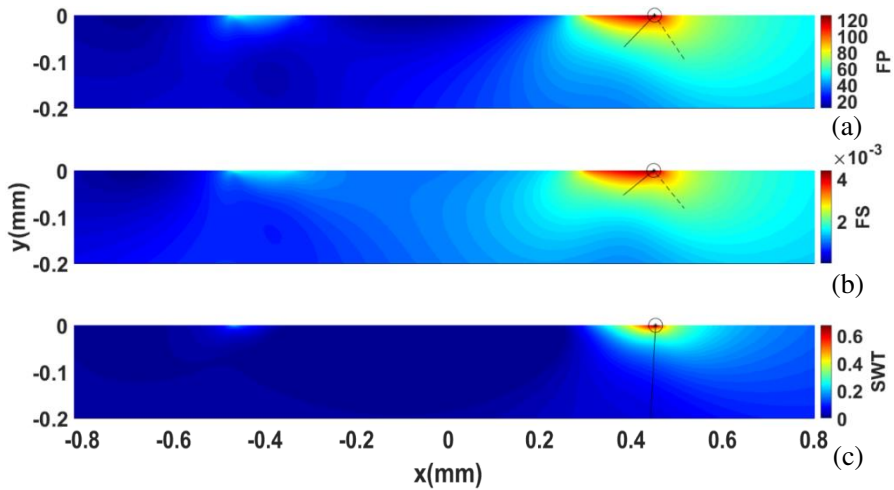


Figure 4.5. (a) FP, (b) FS and (c) SWT parameters distribution at contact surface for test 1.

For homogeneous materials, previous scholars generally defaulted that the crack initiation point located at the contact edge in Ref [155, 223]. However, there is little concern about the distribution of damage parameters below the contact surface. The peaks of damage parameters are located at the contact surface edge, shown as the black circle in Figure 4.5. For FP and FS parameters, the black dotted line is a schematic diagram of the critical plane direction, indicating the crack initiation direction predicted by the different critical plane criteria. The SWT parameter, it is represented by a black line. Based on the vertical line, the crack initiation direction is positive to the right side and negative to the left side. Therefore, the predicted critical plane directions are 34, 39, and

-3 degree, respectively. As shown in Table 4.5, previous researchers [155] have collected experimental results of crack initiation plane direction.

Table 4.5. Fretting fatigue experimental results of critical plane direction from literature

Material	$\theta_c$ (°)	Reference
Ti-6Al-4V	40, -45, -39	Lykins et al.[224]
Ti-6Al-4V	(45/-45) $\pm$ 15	Namjoshi et al.[40]
Al 2024-T351	-55	Proudhon et al.[225]
Ti-6Al-4V	41	Almajali[226]
Al 2024-T351	-50	Szolwinski MP, Farris TN[227]
Al 2024-T3	-35 to -45	Hojjati-Talemi et al.[25]

The most inconsistent prediction results with the experimental results is SWT criteria. It is an energy-based criterion, and the lateral load is dominant in our load so that the predicted direction is almost perpendicular to the specimen surface. Although the predicted results of FP and FS parameter are similar to some experimental results of other materials [40, 224, 226], in the experimental results from our group [25], the direction kept negative, pointing to the inside of the contact area. Using FP and FS critical plane criteria lead to an opposite result, pointing out of the contact area. This shows that it is not appropriate to predict the crack initiation direction by using the critical plane of the peak point, which is called hot spot method. Moreover, because of stress concentration, the damage parameters decrease rapidly along the depth direction. So the life of crack initiation will be underestimated if one uses the hot spot method directly [159, 160]. Herein, the critical distance method is used to average the high local stresses. The critical distance  $l_c$

can be calculated by El Haddad empirical law [145] as Eq. (2.16). Where the long crack threshold stress intensity factor range is  $\Delta K_{th} = 100 \text{ MPa}\sqrt{\text{mm}}$  [164], and the plain specimen fatigue strength is  $\sigma_{0[10^6]} = 263 \text{ MPa}$  for the Aluminium alloy 2024 T3, therefore  $l_c = 46.02 \text{ }\mu\text{m}$ . This study makes use of the area averaging method to reduce the effect of the life underestimation caused by stress concentration. Taking the peak point as the centre and using the critical distance as the radius, the damage parameters in this region are averaged to predict the life.

Through the above method, the crack initiation lifetime can be predicted by the hot spot method and the area average method. The part about the crack propagation life is completed by other colleagues in our group, which predicts the crack propagation lifetime by an extended maximum tangential stress criterion [228]. The size of the initial crack in the propagation phase is  $50 \text{ }\mu\text{m}$  which is calculated from Eq. (2.16). The result should be  $46.02 \text{ }\mu\text{m}$ , but they made an approximation [25, 228]. And the crack initial orientation is  $-40^\circ$ . For all tests, the total life expectancy by the hot spot method is conservative and lower than the experimental total life [25] as shown in Figure 4.6 (a). However, after averaging the damage parameters by the area average method, the predicted life will better fit the experimental results. In addition, the difference between all prediction results and experimental results is within the factor of 2 lines as shown in Figure 4.6 (b). Moreover, in this way

the critical distance of FP, FS and SWT parameters can be obtained, which are 14  $\mu\text{m}$ , 10  $\mu\text{m}$ , 14  $\mu\text{m}$ , respectively.

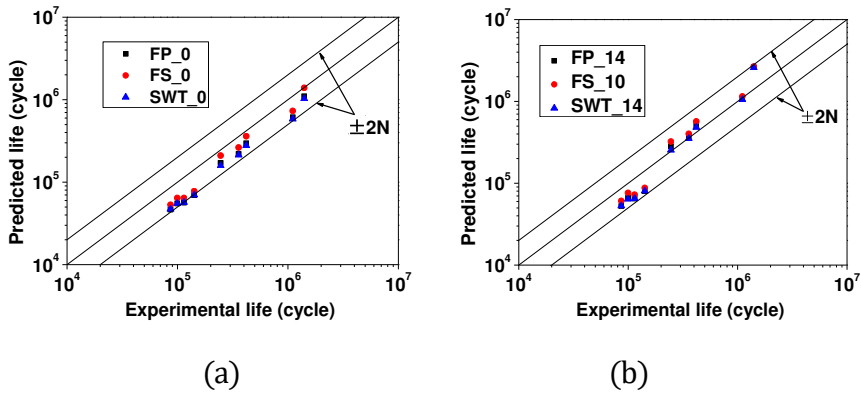


Figure 4.6. Comparison between prediction and experimental failure life using (a) hot spot method and (b) area average method.

In addition to the material and load conditions, the contact size can also affect the critical distance. The comparison between simulations and experiments proves that for the case of high-stress concentration, the critical distance equivalent to the grain size can be used to obtain good prediction results [229]. Therefore, in this study, for the peak value appearing at the edge of the micro-void, the critical distance of the three damage parameters is 20  $\mu\text{m}$ . Then, the peak point of the edge of the micro-void  $P_v$  and the maximum value point of the contact surface  $P_s$  are averaged with different critical distances. Finally, by comparing the life predicted by these two dangerous points ( $N_{iv}$  and  $N_{is}$ ), and choose the lower, the final result is obtained as shown as Figure 4.7.

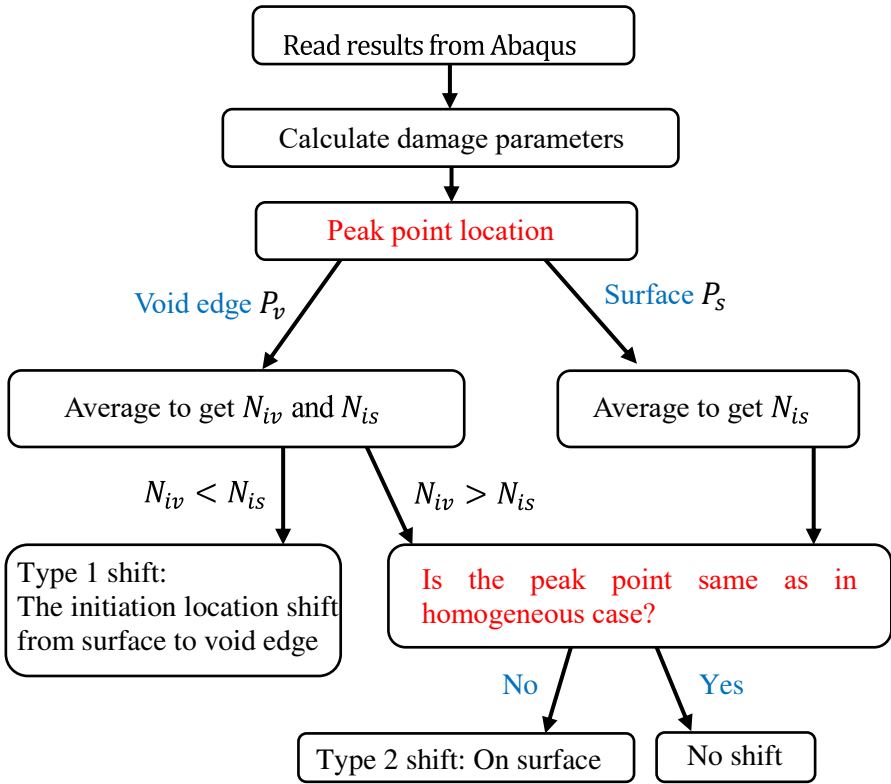


Figure 4.7. Flow chart for calculation of damage parameters and crack initiation location

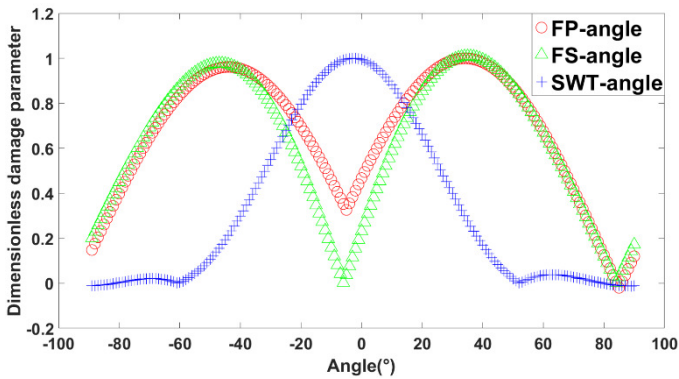


Figure 4.8. Variation of dimensionless parameter with angle at peak point.

Regarding the crack initiation direction, the quadrant average method is used to determine whether the crack initiation angle is directed to the contact area or away from the contact area [160]. As shown in Figure 4.8, the dimensionless FP and FS parameters have two peaks, one between  $-90^\circ$  and  $0^\circ$ , the other between  $0^\circ$  and  $90^\circ$ . The quadrant averaging method uses the surface vertical line of the peak point to divide the specimen into two left and right quadrants as shown in Figure 4.9 (a). For the case of considering critical void, the quadrant division diagram is shown in Figure 4.9 (b).

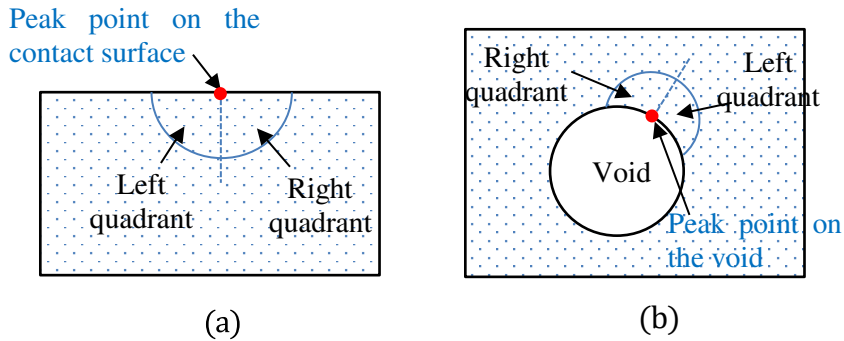


Figure 4.9. Quadrant method diagram (a) Peak point on the contact surface and (b) Peak point on the void.

Then, the damage parameters are averaged in the range of a quarter circle in the two quadrants with the critical distance as the radius. Because the different definition of the critical plane of the different parameter, for the FP parameter, if the average parameter of the left quadrant is larger than the right side, the critical plane will be searched among the angle from  $-90^\circ$  to  $0^\circ$ . Otherwise, the critical plane will be searched among the angle from  $0^\circ$  to  $90^\circ$  as shown in Figure 4.8. For the FS parameter, the critical plane is defined as the plane subjected to the maximum shear strain amplitude. Therefore, there are two planes with maximum shear strain amplitude for one point depending on the Mohr's strain circle. In addition, there are  $90^\circ$  difference between these two planes. Therefore, according to the quadrant method, the crack initiation angle with larger regional average damage parameter can be obtained. As shown in Table 4.6, based on the FP and FS parameters, there is a big difference between the critical

plane angles obtained by the hot spot method and the quadrant average method. For test 1, as shown in Figure 4.5, the black dotted line and black line is the critical plane obtained by the hot spot method and the quadrant average method, respectively. And the results of quadrant method are closer to the experimental results, from  $-45^\circ$  to  $-35^\circ$  [25] as shown in Table 4.5. SWT parameter just has one peak from  $-90^\circ$  to  $90^\circ$ , so that it does not need to correct the critical plane angle.

Table 4.6. Predicted peak position (abscissa) and critical plane angle for all test.

Test number	Peak position (mm)			Hot spot method $\theta_c(^{\circ})$			Quadrant method $\theta_c(^{\circ})$	
	FP	FS	SWT	FP	FS	SWT	FP	FS
1	0.454	0.452	0.456	34	39	-3	-44	-51
2	0.452	0.452	0.454	34	40	-3	-44	-50
3	0.452	0.452	0.454	35	40	-3	-43	-50
4	0.452	0.452	0.454	34	40	-3	-44	-50
5	0.452	0.452	0.454	34	40	-3	-43	-50
6	0.448	0.446	0.45	35	40	-2	-43	-50
7	0.448	0.446	0.45	35	40	-2	-43	-50
8	0.45	0.45	0.452	35	41	-2	-42	-49
9	0.448	0.45	0.45	35	41	-2	-43	-49

In summary, the area average method can obtain a crack initiation life closer to the test than the hot spot method, and the difference between all prediction results and the experimental results is within the band of 2N as shown in Figure 4.6. The quadrant average method can obtain a more reasonable critical plane angle, showing that the cracking direction points are inside the contact area. The FP criteria has the best prediction angle.

And the crack initiation angle predicted by SWT parameters is almost perpendicular to the contact surface, which is inconsistent with the experimental observations. In addition, the prediction peak position is very stable around  $x = 0.452$  mm for all parameters and test as shown in Table 4.6.

#### 4.3.2 Effect of critical micro-void location

In order to study the effect of critical micro-void location on the fretting fatigue, one circle micro-void with 44  $\mu\text{m}$  diameter shift the location under the contact surface from  $x = 0$  mm to  $x = 0.7$  mm in increments of 0.1 mm and from  $y = -0.05$  mm to  $y = -0.3$  mm in increments of  $-0.05$  mm. A total number of 48 different micro-void location cases is considered. In addition, the load of Test 1 is used in all studies. As shown in Figure 10, an example is given for the case where the critical micro-void locates at  $x = 0.4$  mm and  $y = -0.1$  mm. The damage parameters distribution and critical plane angles are shown in Figure 4.10. After introducing the micro-void, the distribution of the parameters under the contact surface is very different compared with the homogeneous case in Figure 4.5. When considering specimen heterogeneity, multiple peak points appear simultaneously on the contact surface as well as inside specimen, indicating that the specimen may have multiple cracks initiation position, which is consistent with experimental observation [105]. In addition to the maximum value transferred to the

inside of the specimen, the damage parameters appear to decrease at the contact surface directly above the micro-void.

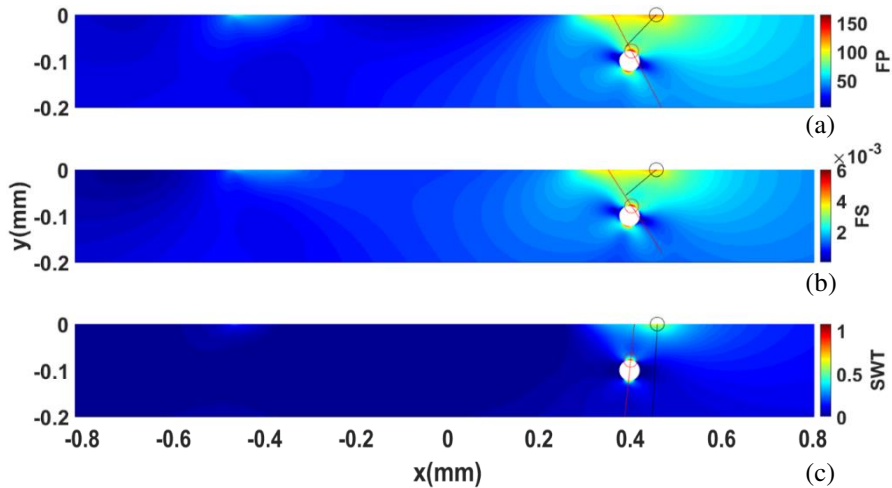


Figure 4.10. (a) FP, (b) FS and (c) SWT parameters distribution for the case with a critical micro-void locate at  $x = 0.4$  mm,  $y = -0.1$  mm.

The red circle and the red line indicate the point of the maximum parameter and the critical plane at that point for all three parameters. For the three damage parameters, their maximum values appear at the edge of the micro-void, but after averaging, the regions surrounding the contact edge still provide smaller predicted lives. Therefore, the black circle and the black line indicate the crack initiation position and crack plane as shown in Figure 4.10. It can be seen that the presence of critical micro-void causes significant interference in the distribution of all damage parameters. However, it has less influence on crack initiation position and angle compared with the homogeneous case as shown in Table 4.6.

### 4.3.2.1 The crack initiation position

The prediction of crack initiation point coordinates of FP, FS, and SWT parameter for all cases are shown in Figure 4.11. FP parameter, the crack initiation point is transferred to the inside of the specimen when the micro-voids located at  $x = 0.4 \text{ mm}$ ,  $y = -0.05 \text{ mm}$  and  $x = 0.6 \text{ mm}$ ,  $y = -0.05 \text{ mm}$ . The crack initiation position appears near the top edge of the critical micro-void, and we call this kind of peak shift 'type 1' as listed in Table 4.7. Figure 4.7 also shows the decision logic for this type of shift. The reason why the case when the micro-void centre located at (0.5, -0.05) peak point shift does not occur is that the micro-void is very close to the contact edge. The effect of the micro-void results in high damage parameters at the vicinity of the contact edge. Although both the contact edge and the top edge of the micro-void are dangerous, the contact edge gives a shorter crack initiation life estimate. In addition to the two cases where the peak shift occurred, the peak positions of other cases were stable and located at the edge of the contact surface. Moreover, the abscissa of heterogeneous case  $x_{he}$  range between 0.45 mm and 0.456 mm, which is 0.454 mm for homogeneous case ( $x_{ho}$ ). This shows that except for a few critical micro-voids that are very close to the contact edge, the micro-void at other locations have little effect on the crack initiation position and are consistent with the homogeneous case.

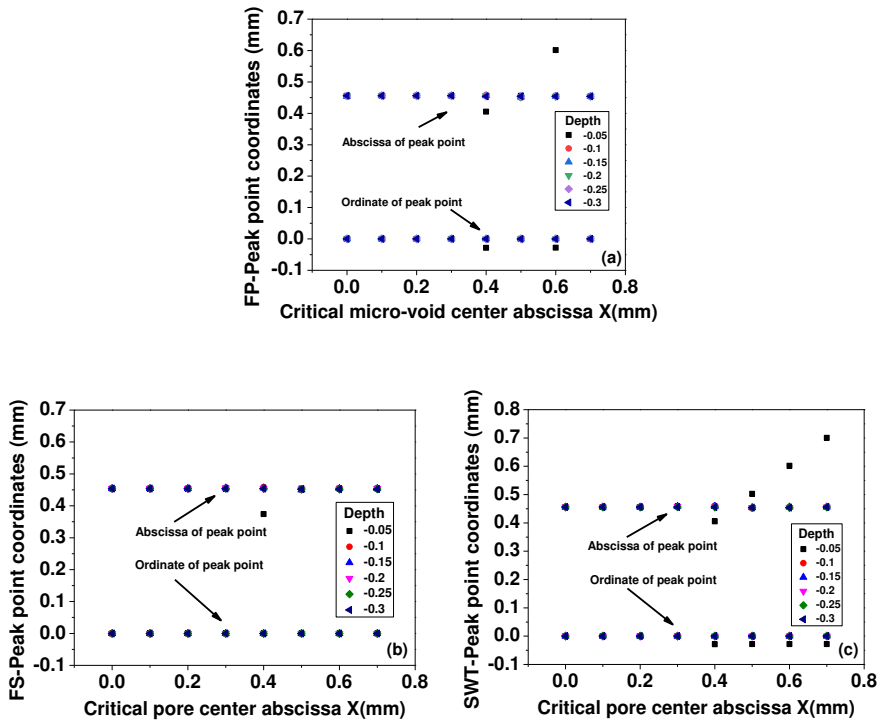


Figure 4.11. The prediction of peak point coordinates of (a) FP, (b) FS and (c) SWT parameters for all cases.

FS parameter, as shown in Figure 4.11(b), the peak point of all cases appears on the contact surface and does not transfer into the specimen. Most of the peak point located between  $x = 0.45$  mm and  $x = 0.458$  mm and the homogeneous case it is  $x = 0.452$  mm as list in Table 4.7.

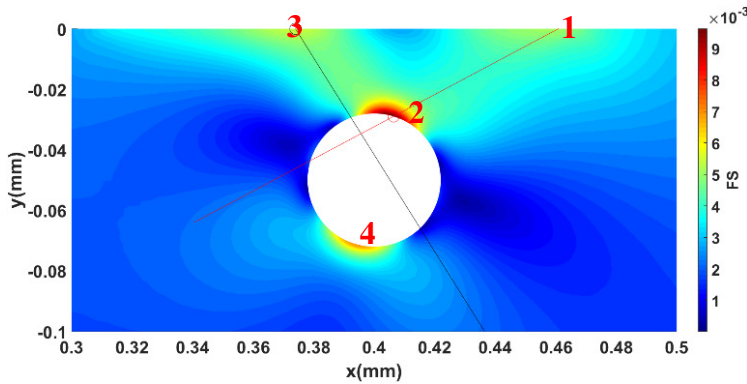


Figure 4.12. FS parameter distribution of the case with a critical micro-void locate at  $x = 0.4$  mm,  $y = -0.05$  mm

However, when the micro-void is located at  $x = 0.4$  mm and  $y = -0.05$  mm, the peak lateral shift is from point 1 (contact edge) to point 3 (0.374, 0) as shown in Figure 4.12. By including the contact edge (point 1) and the top edge point of the micro-void (point 2), the peak point is also possible to appear at point 3. This point is located at the left intersection of the contact surface and the high-stress zone is caused by the micro-void. This kind of peak shift on the surface is called ‘type 2’ as listed in Table 4.7. Moreover, including point 4, other potentially dangerous points are likely to propagate new cracks soon after crack initiates at the peak point. Numerical and experimental studies on the effects of individual embedded inclusion defects on the Hertz loading damage have similar multi-point cracking result, such as the crack distribution of butterfly wings [230].

The results of SWT parameter are similar like FP parameter. When the micro-void depth is located at -0.05 and the micro-void centre abscissa is greater than 0.4, the crack initiation point will appear near the top edge of the micro-void as type 1 peak shift. For other cases, the results are very stable and the peak point position is similar to the homogeneous case.

Table 4.7. The general range of peak position and the detail of the special case (peak shift) of three kinds of prediction.

Normal cases			Peak shift		
Parameter	$x_{ho}$ (mm)	$x_{he}$ (mm)	Micro-void position	Peak position	Type
FP	0.454	0.45-0.456	(0.4, -0.005)	(0.4055, -0.0287)	1
			(0.6, -0.05)	(0.6015, -0.028)	1
FS	0.452	0.45-0.458	(0.4, -0.05)	(0.374, 0)	2
SWT	0.456	0.452-0.46	(0.4, -0.05)	(0.4055, -0.0287)	1
			(0.5, -0.05)	(0.5025, -0.028)	1
			(0.6, -0.05)	(0.6015, -0.028)	1
			(0.7, -0.05)	(0.7005, -0.028)	1

#### 4.3.2.2 The crack plane angle

As shown in Figure 4.13, in most cases where a single critical micro-void is considered, the critical plane angle of the heterogeneous specimen ( $\theta_{he}$ ) is almost constant and is the same as homogenization case ( $\theta_{ho}$ ). But there are still some special cases here when the micro-void is particularly close to the contact edge as listed in Table 4.8. In comparison with Table 4.7, it can be seen that a significant change in the critical plane angle when the peak shift (type 1 and type 2). In addition, when the micro-void located at (0.5, -0.05), the peaks do not shift, but the predicted

critical plane is also changed significantly compared with the homogeneous case.

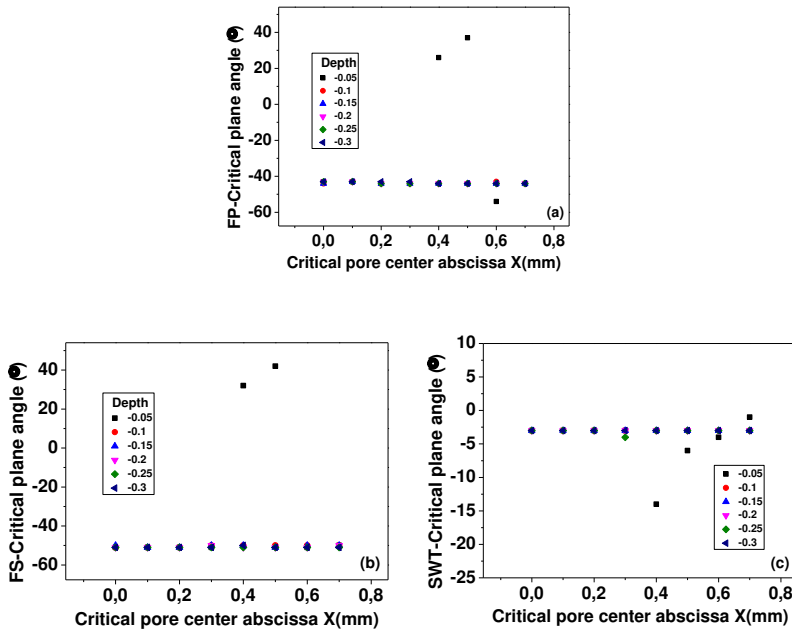


Figure 4.13. The prediction of critical plane of (a) FP, (b) FS and (c) SWT parameter for all cases

Table 4.8. The general range of critical plane angle and the detail of the special case (critical plane shift) of three kinds of prediction.

Parameter	Normal cases		Critical plane shift		
	$\theta_{ho}$ (°)	$\theta_{he}$ (°)	Micro-void position(mm)	CP angle(°)	Type
FP	-44	-44 and -43	(0.4, -0.005)	26	1
			(0.5, -0.05)	37	
			(0.6, -0.05)	-54	1
FS	-51	-50 and -51	(0.4, -0.05)	32	2
			(0.5, -0.05)	42	

---

SWT	-3	-3	(0.4, -0.05)	-14	1
			(0.5, -0.05)	-6	1
			(0.6, -0.05)	-4	1
			(0.7, -0.05)	-1	1

---

In this case, both critical planes predicted by FP and FS parameters are directed from the contact edge to the micro-void. As the micro-void becomes close to the contact edge case, although damage parameters near the contact edge are large due to the influence of the micro-void, the dangerous point position is still the same as in the homogenous case. However, the critical plane is seriously affected by the heterogeneity. Presumably, in this case, the crack initiation life will also change significantly.

#### 4.3.2.3 The crack initiation life

As mentioned above, except for the cases where the critical micro-void is close to the contact edge, the existence of the micro-voids does not have much influence on the peak position and the critical plane angle. However, critical micro-voids have a significant effect on crack initiation life. The predicted dimensionless crack initiation lives for all cases by three parameters are shown in Figure 4.14. The dimensionless initiation lifetime is the ratio of the crack initiation life between the heterogeneous and homogenized conditions to evaluate the effect of the critical micro-void at different locations on crack initiation.

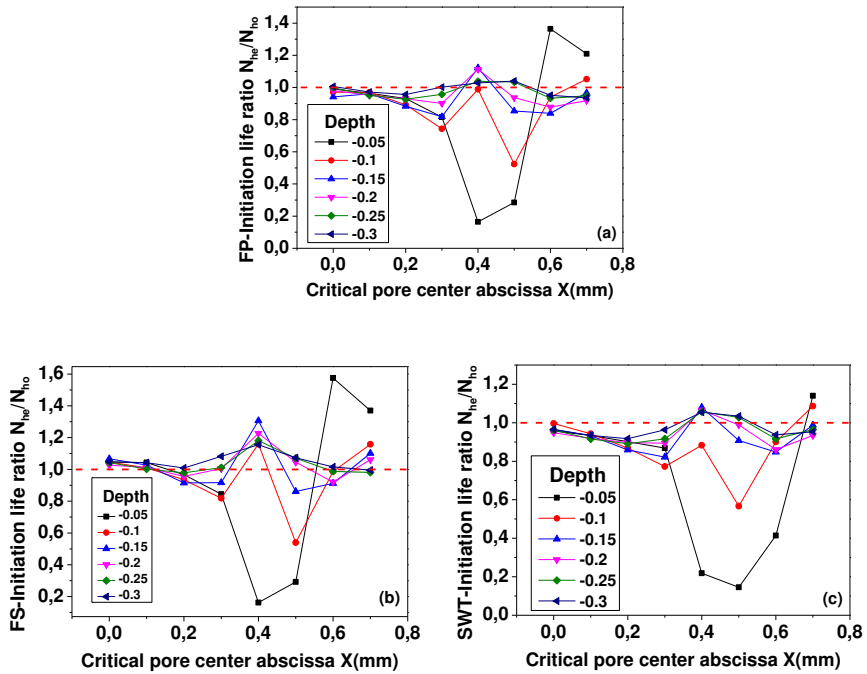


Figure 4.14. The predicted dimensionless crack initiation life for all cases by (a) FP, (b) FS and (c) SWT parameters

When the micro-void is located in the first layer (depth =  $-0.05$  mm), the prediction life changes very much. For this layer, if the micro-void located at the left side of the contact edge, the initiation life decrease as the abscissa of the micro-voids increases. If the micro-void located at the right side of the contact edge, the initiation life increases quickly at first and then decrease as the abscissa of the micro-void increase. It is conceivable that as the abscissa of critical micro-void continues to increase, the predicted dimensionless initiation life will gradually

approach 1. The minimum of initiation life appears when the micro-void near the contact edge. Here the minimum prediction initiation life is around 15% of the homogenization case. If there is more intensive forecast data, perhaps the above life peak and turning point will change, but the trend will be the same.

For the second layer (depth =  $-0.1$  mm), the trend of initiation life is not very obvious, and it is a little confusing. Such oscillations are also an uncertain factor in the fretting fatigue of components. Because when the micro-voids are close to the contact edge, the crack initiation life is also significantly reduced, causing the component to damage faster.

For the layer below the second layer, the trend of initiation life is consistent and interesting. When the micro-voids are close to the contact centre, the estimated life in the heterogeneous case is not much different from the homogeneous case. As the abscissa of the centre of the micro-void increases, the life expectancy gradually decreases. As the micro-void depth increases, the decrease in predicted life is less obvious. The estimated life will suddenly increase when it approaches the left side of the contact edge ( $x = 0.4$  mm). The prediction life will even exceed the homogeneous material. When the abscissa of the micro-void centre is equal to  $0.4$  mm, the estimated life decreases as the micro-void depth increases.

---

This phenomenon indicates that when the critical micro-void is located on the left side of the contact edge and the depth exceeds a certain value, the existence of the micro-void has a positive effect on the crack initiation life. This effect gradually decreases as the depth continues to increase. When the abscissa of the centre of the micro-voids exceed the contact edge, the estimated life is first reduced and then increased. Ultimately, with the micro-voids relatively close to the surface, the estimated life may still exceed the homogeneous case. The effect of micro-void location on crack initiation lifetime is more intuitively shown in 2D cloud map Figure 4.15.

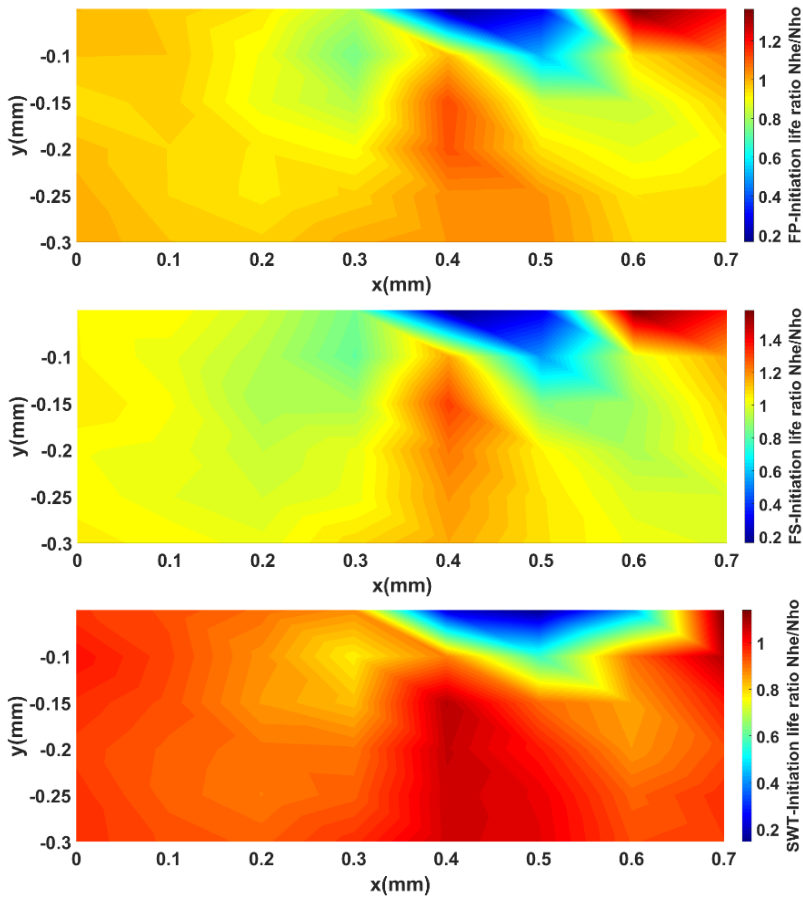
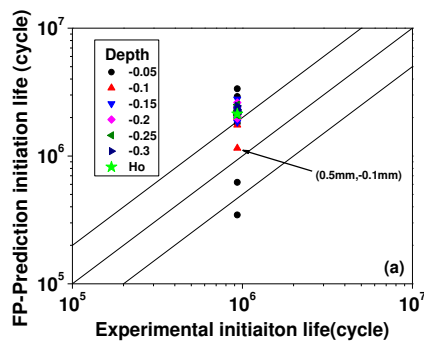


Figure 4.15. The effect of micro-void location on crack initiation lifetime (2D cloud map).

As shown in Figure 4.15, when the micro-void coordinates are in the blue and light-yellow areas, the heterogeneity of the material will accelerate the initiation of the crack compared to the homogeneous case. When the micro-voids are in red and deep red areas, the micro-voids can increase

the crack initiation life of the specimen. There are two main areas here; one is below the left side of the contact edge beginning from a certain depth. The other is the area near the surface of the specimen when the abscissa is at a certain distance larger than the contact edge. Both initiation life enhancement effects occur suddenly and then decrease with increasing depth and abscissa, respectively. Interesting to note that the dangerous area is similar to half of the butterfly's wings, and there are similar high damage parameter areas near points 2 and 4 in Figure 4.12. Referring to the experimental results, the specimens used in experimental tests [25] also contain some kind of defects, which are the reason for the discrete phenomenon when comparing the total estimated lifetime with the experimental observations as shown in Figure 4.6. Because of the micro-voids have a severe effect on the fatigue [24, 62, 65], the single critical micro-void considered in this paper may also be one kind of these defects.



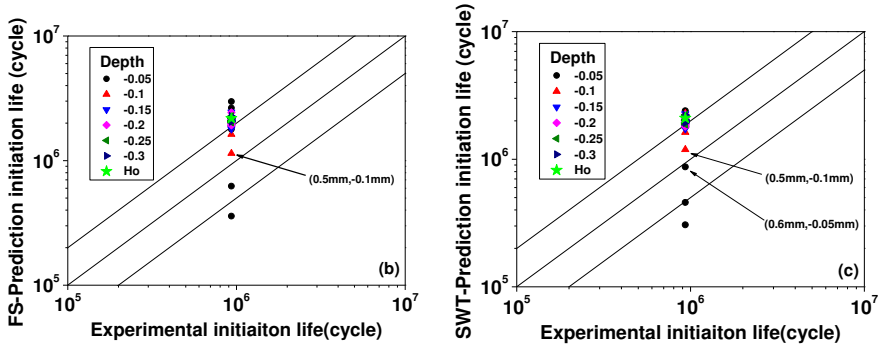


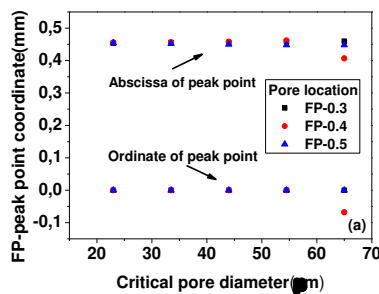
Figure 4.16. The comparison between the prediction initiation life of heterogeneous specimen and experimental result: (a) FP, (b) FS and (c) SWT criterion.

The peak shift occurs mostly when the micro-void is very close to the contact edge. Moreover, when the micro-void is far from the contact edge, the peak point position is almost the same as the homogeneous sample. Therefore, in order to make a rough contrast, the effect of micro-void on crack propagation is ignored, here. The comparison between the crack initiation life of experimental result (test 1) and the prediction result of heterogeneous cases (considering different location critical micro-void) is shown in Figure 4.16. For all 48 cases considered in this paper, it can be found that the existence of a single critical micro-void will lead to the discretization of the crack initiation life. Most of the prediction initiation life are bigger than the experimental ones. In addition, for FP and FS criterion, the prediction results are closer to the test results when the micro-void is located at (0.5 mm, -0.1 mm). The differences are 18.86%

and 18.32%, respectively. For SWT criterion, the two micro-void location cases closest to the test results are (0.6 mm, -0.05 mm) and (0.5 mm, -0.1 mm). Moreover, the differences are 21.62% and 6.75%, respectively. This gives us inspiration. If the prediction model considers critical defects that are consistent with the actual situation (can get by X-ray CT scanning system [63]), it will greatly improve the accuracy of the prediction.

### 4.3.3 Effect of micro-void size

In this study, in order to compare the effect of different micro-void diameter on fretting fatigue, three micro-void locations and five kinds of micro-void diameter have been chosen to study. The critical micro-voids located at depth equal -0.1 mm, abscissa equal 0.3, 0.4 and 0.5 mm. The micro-void diameters are 23, 33.5, 44, 54.5, 65  $\mu\text{m}$ , which cover the range of all randomly distributed micro-voids that have been considering in the heterogeneous specimen as shown in Figure 17.



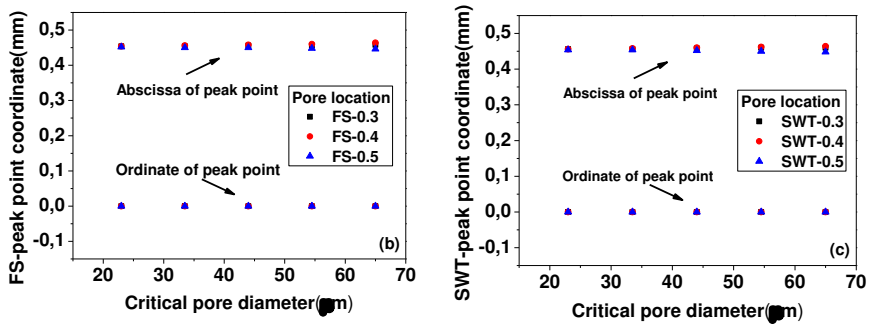


Figure 4.17. The prediction of peak point coordinates of (a) FP, (b) FS, (c) SWT parameter for all cases with different micro-void size.

As shown in Figure 4.17(a), only when the 65 micron diameter micro-void located at  $x = 0.4$  mm is predicted by the FP criterion, the crack initiation point is transferred. Moreover, the crack initiation point shift to the top edge of the micro-void ( $x = 0.407$  mm,  $y = -0.068$  mm), which is type 1 shift. However, for all other cases, the crack initiation point is almost unchanged and similar to the homogeneous case.

The effect of micro-void size on the critical plane orientation has similar characteristics. The critical plane orientation changes into  $-52^\circ$  in the case of the crack initiation point shift. For other cases, the critical plane orientations are almost constant and similar to the homogenization situation as shown in Table 4.8.

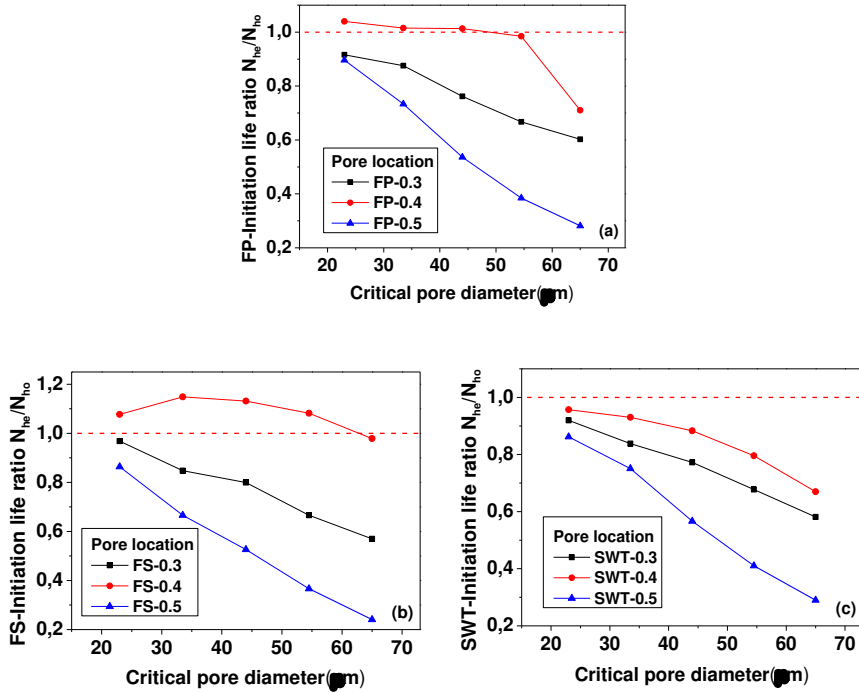


Figure 4.18. The prediction of dimensionless crack initiation life of (a) FP, (b) FS and (c) SWT parameter for all cases with different micro-void size.

As shown in Figure 4.18, in general, the crack initiation life decreases with the increase of micro-void diameter at the same position. In addition, when the micro-void are at  $x = 0.5$  mm, this downward trend is the most obvious. However, as shown in Figure 4.18 (b), for the case which micro-void centre is located at  $x = 0.4$  mm and one uses the FS criterion, the predicted initiation life increases at first and then decrease as the size increase. It means the effect of micro-void size is different with a different

micro-void location. And as shown in Figure 4.14 (b) red solid line, the dimensionless initiation life is more than 1 when the void located at (0.4 mm, -0.1 mm).

It is mean this particular trend occurs when the void is located in the enhancer region. The fretting fatigue life is enhanced because the existence of the void weakens the stress concentration at the contact edge, Larger void can more effectively reduce this stress concentration, resulting in an increase in crack initiation life. However, when the void size continues to increase beyond a certain value, the presence of the void causes high stress at the contact edge, thereby reducing the predicted life. Therefore, it can be guessed that when the micro-voids are located in the enhancer region as shown in Figure 4.15 red part, the crack initiation life of fretting fatigue will reach a maximum at a certain micro-void diameter, and larger or smaller than this diameter will reduce the crack initiation life. This phenomenon can be understood as the existence of suitable micro-voids weakens the stiffness of the contact edge, thereby reducing the stress concentration at the contact edge. In a certain range, the micro-void size increases, which in turn relieves the stress concentration at the contact edge. Therefore, the crack initiation life will increase.

#### 4.4 Summary

From this study, the following conclusions are drawn:

1. For the homogeneous case, all peaks of three kinds of the critical plane parameter are located inside and close to the contact right edge of maximum load. Moreover, the FP criterion can obtain the critical plane angle that best matches the experimental results by the quadrant averaging method.
2. The presence of material heterogeneity (critical micro-voids) has a strong influence on the distribution of damage parameters below the contact surface of the specimen. But for most heterogeneous materials, the crack initiation position and crack plane angle are similar to the homogeneous case. When the critical micro-void is close to the contact edge, the peak point of the damage parameter has two kinds of shift and the critical plane also change. For some cases, even if the cracking position is unchanged, the crack initiation direction may change greatly compared with the homogeneous case.
3. When the critical micro-voids are located at different positions inside the sample, there is a weakened area similar to the half butterfly wings, that is, when the micro-voids are located in this area, the crack initiation life will be less than the homogenous case. Moreover, the weakening effect is more severe when the micro-voids are close to the left and below the contact edge. Conversely, there are also two enhancement zones. When the micro-voids are located in these two zones, the fretting fatigue life can be increased, that is, a certain depth below the contact edge and a certain range to the right of the contact edge. Both of these

---

enhancements only occur within a certain range and eventually disappear as they become farther away from the contact edge. The enhancement on the right is more noticeable. Moreover, if the prediction model considers critical defects that are consistent with the actual situation, it can greatly improve the accuracy of the prediction.

4. For most micro-void locations, the location of the crack initiation point and the angle of initiation are not very sensitive to the micro-void size. The micro-void size has different effects on fatigue at different locations. When the micro-voids are located in the reinforcement zone, the fatigue life increases first and then decreases as the micro-void size increases. When the micro-voids are in the danger zone, the life span will decrease rapidly with the increase of the micro-void size.

## **Chapter 5 Fretting fatigue with pit treatment surface**

This chapter analyses the effect of surface treatment on fretting fatigue specimen by numerical simulations using Finite Element Analysis. The processed specimen refers to artificially adding a cylindrical pit to its contact surface. Then, the contact radius between the pad and the specimen is controlled by adjusting the radius of the pit. The stress distribution and slip amplitude of the contact surface under different contact geometries are compared. The critical plane approach is used to predict the crack initiation life to evaluate the effect of processed specimen on its fretting fatigue performance. Both crack initiation life and the crack initiation angle can be predicted by the critical plane approach. Ruiz parameter is used to consider the effect of the contact slip. It is shown that the crack initial position is dependent on the tensile stress. For the same type of model, three kinds of critical plane parameters and Ruiz method provide a very similar position of crack initiation. Moreover, the improved sample is much safer than the flat-specimen.

## 5.1 Numerical Model

As shown in Figure 3.1, a schematic of fretting fatigue specimen is illustrated. The specimen is flat, which is the general case. This paper aims to study the effect of surface pit treatment on fretting fatigue behaviour. Three models are used for comparative studies depending on the degree of surface pit treatment. The finite element model of the flat specimen, named as type 1, is shown in Figure 3.1. Next, artificially processed specimen, i.e. adding pits to the surface of the contact area, is also studied. The size of the pit is selected based on the contact radius between the pad and the specimen under normal compression contact load. In this study, the material of cylinder pad and specimen is Aluminium 2024-T3, whose elastic modulus and Poisson's ratio are 72.1 GPa and 0.33, respectively.

As shown in Figure 3.2, if only the normal force  $F = 540$  N acts at the top of the pad, which is a Hertzian contact problem [75]. When the pit radius is  $R_{pit}$ , the contact radius  $R$  and contact stress distribution on the contact surface  $p(x)$  are given by Eq. (5.1) and Eq. (5.2), respectively [75].

$$R = \sqrt{\frac{4F\left(\frac{1-v_1^2}{E_1} + \frac{1-v_2^2}{E_2}\right)}{\pi t\left(\frac{1}{R_{pad}} + \frac{1}{R_{pit}}\right)}} \quad (5.1)$$

$$p(x) = -\frac{2F}{\pi R t} \sqrt{1 - (x - R)^2} \quad (5.2)$$

where  $E_1 = E_2 = 72.1 \text{ Gpa}$  is the elastic modulus of the cylinder pad and the specimen, and  $\nu_1 = \nu_2 = 0.33$  is Poisson's ratio .

Therefore, as shown in Figure 5.1, the contact radius of two components will change with different pit radius on the specimen depends on the Hertzian contact theory. It is worth noting that for the case where the cylinder is in contact with the pit, the pit radius  $R_{pit}$  should be taken as a negative value in Eq. (5.1). In Fig. 5, the relationship between the true pit radius and the contact radius is shown for the sake of intuition. If the pit radius tends to infinity the Hertzian contact radius is 0.462 mm. This is the type 1 model, shown as a red point in Figure 5.1. When the pit radius is slightly larger than 50 mm , the theoretical contact radius changes drastically, and the maximum value can reach 5 mm. The main idea of surface processing is to increase the contact area and reduce the surface stress and strain amplitudes. Thus, adding a pit to the specimen with a radius of 50 mm (same as the pad) is considered first. However, this produces a complete slip, and the calculation could not converge. Therefore, 50.5 mm (blue point) is selected as the pit radius to facilitate convergence (in the remaining part of this article, it is named type 3). Its Hertzian contact radius of is 4.645 mm . In order to consider the

intermediate state, 52 mm is used as pit radius for type 2 model, whose theoretical contact radius is 2.36 mm (green point).

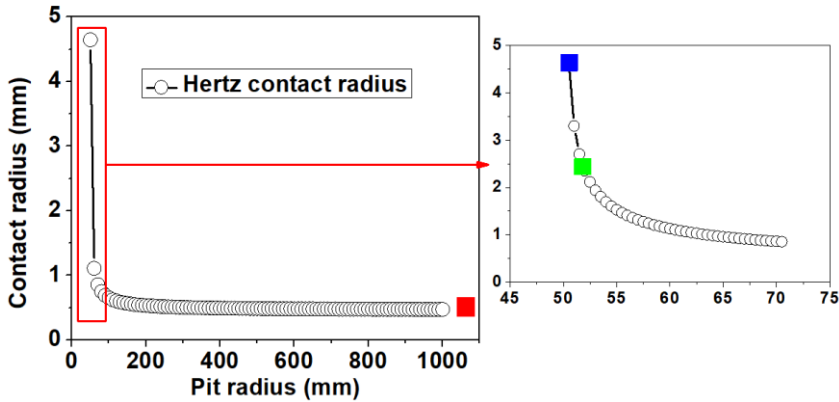


Figure 5.1. The theoretical contact radius change with the pit radius

As mentioned above, the theoretical contact radius can be achieved by machining a pit with a milling cutter of a specific diameter. To ensure that the width of the pit is greater than that of the cylinder pad, point B is 0.05 mm higher than point A as shown in Figure 5.2. Therefore, through this principle, the height of the center of the pit from the specimen surface can be calculated. The heights of pits center of Type 1, Type 2 and Type 3 are 50 mm, 51.745 mm and 50.245 mm respectively. Moreover, the local finite element model of Type 3 is also shown in Figure 5.2.

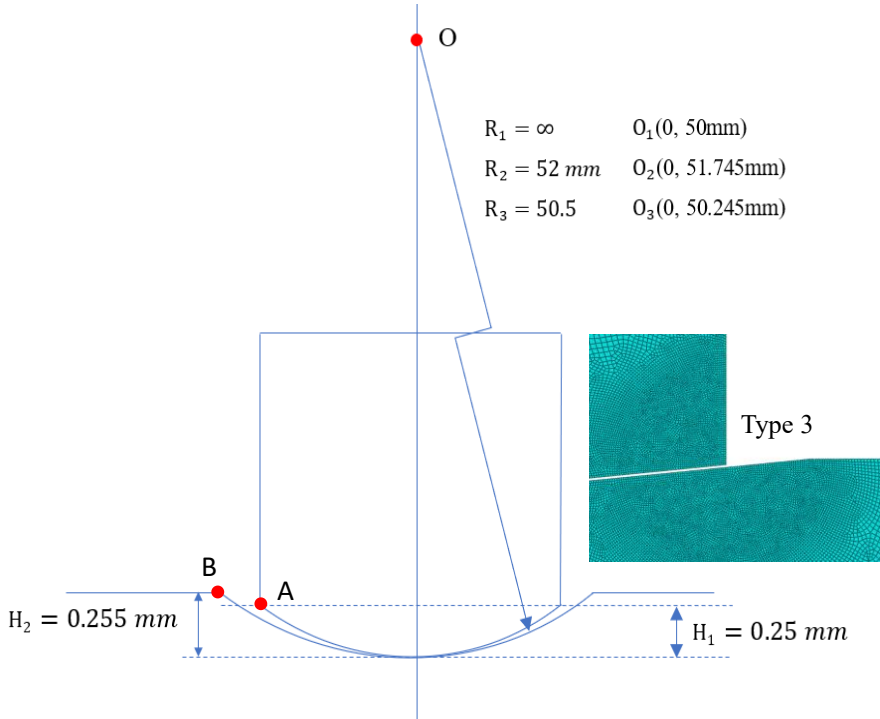


Figure 5.2. Pit radius and position.

Based on the Hertz contact theory as Eq. (5.2), the normal stress on the contact surface is shown in Figure 5.3. The maximum normal stresses of each model are  $-186.965 \text{ MPa}$ ,  $-36.66 \text{ MPa}$  and  $-18.6 \text{ MPa}$ , respectively. The contact radius of type 3 is almost 10 times higher than that of type 1, and the maximum normal stress is one-tenth of the maximum value of type 1.

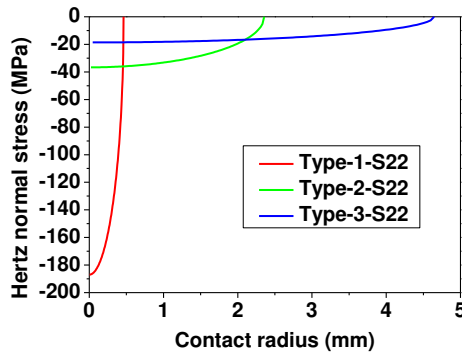


Figure 5.3. The theoretical normal stress of the contact surface for types 1, 2 and 3

The artificially processed specimen and FE model of type 2 are shown in Figure 5.4 as an example. The FE model in Figure 5.4 is built in Abaqus using plane strain 2D four nodes element (CPE4R). On the contact surface, the size of the element is 0.002 mm, which allows the mesh to converge and obtain sufficiently accurate results [107]. The element numbers of Type 1, Type 2 and Type 3 are 39760, 159095 and 112269, respectively.

After the simulation, Python codes were used to do the post-process in order to get the stress and strain history for each node on the contact surface. Matlab codes were used to calculate the critical plane parameters. The codes would go through every node on the contact surface of the specimen. For every node, every angle plane would be checked, in order to find out the critical plane. In addition, an angle increment of  $1^\circ$  was used for each iteration.

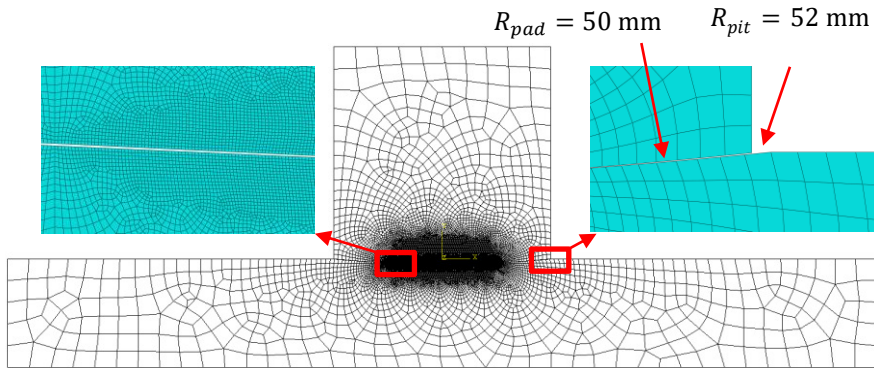


Figure 5.4. Finite element model of type 2 (pit-specimen)

## 5.2 Experimental Validation

The experimental research on fretting contact between pad and flat specimen [231] has been described in the previous two chapters. Here only give a short review. Figure 3.1 shows the schematic of the experimental setup.

And the load conditions of the fatigue experiments and failure life results are listed in Table 4.2. In order to verify the rationality of the critical plane method for predicting crack initiation life, the  $N_f$  of all tests are used to validate the numerical model and the prediction methods. However, to study the effects of the surface pit treatment on fretting fatigue, the load of test 1 is used along with all kind of critical plane methods for all proposed models.

The above critical plane method without averaging described in chapter 2, is used to predict the crack initiation life of type 1 model under 9 kinds of test. Then, combined with the crack propagation part [228], the total fretting fatigue life prediction for all tests can be compared with the total failure life from the experimental as shown in Figure 4.6 (a). From the results, it is shown that the FS parameter gives the best prediction. Although the prediction of all cases has a certain degree of conservatism, all the results are within the factor of  $\pm 2N$ . Therefore, it can be concluded that the critical plane method can be used to predict crack initiation life under multiaxial stress field. Furthermore, it is reasonable to use the critical plane method to estimate the crack initiation lifetime for the other two types of models.

### 5.3 Results and Discussion

Because the stress distribution has a great influence on the fretting fatigue life of the structure, after applying the cyclic load to the model, the stress distribution in the specimen can be calculated over the entire period. Moreover, by extracting the result data, the fatigue characteristics of the specimen can be evaluated by three different critical plane parameters. In addition to the contact surface, the critical plane parameters below the surface are also calculated and presented, which allows a more comprehensive comparison of the two models considered in this paper.

### 5.3.1 Stress Distribution in the Three Models

The biggest difference between each model is the contact radius. From the resulting stress distribution as shown in Figure 5.5, the difference in stress concentration is very obvious. The high stress concentration of type 1 model is distributed near the edge of a very small contact area. Therefore, it leads to a higher peak value of stress, not only shear stress but also normal and tensile stresses. However, for the other two models, the stress distribution takes place in a relatively large contact area. The absolute peak value of the shear stress is also much smaller than type 1.

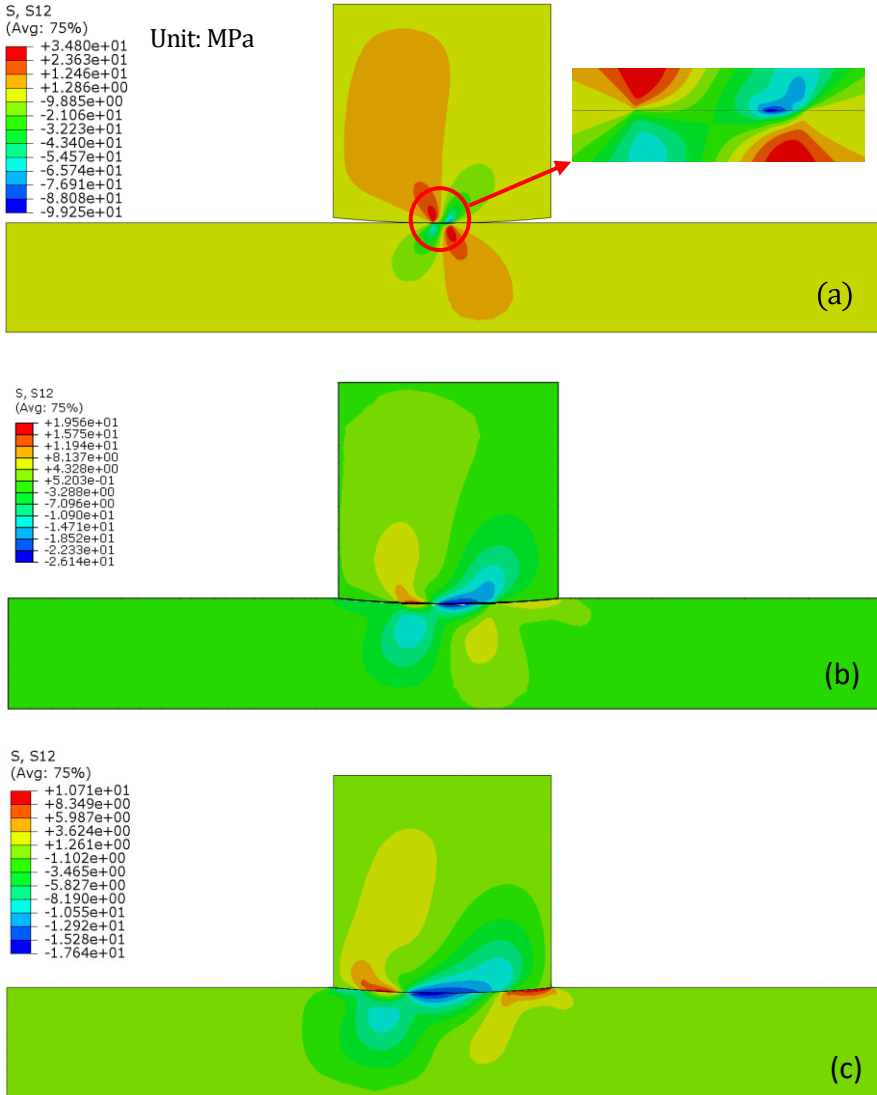


Figure 5.5. The shear stress distribution in the whole model when peak loading (a) type 1, (b) type 2 and (c) type 3

Although Figure 5.5 gives a macro comparison of three models, it is more important to care about the stress on the contact surface. Because it is known from previous scholars' experiments and numerical studies that crack usually appear first at the contact edge for type 1 model. This is similar for type 2 and 3 models because the stress at the contact surface is higher than below the surface.

Contact surface stress distribution comparison between each model is shown in Figure 5.6. Same as the result shown in Figure 5.6 (a), we can see that the tensile stress varies greatly along the contact surface. It reaches a maximum of 290.089 MPa at  $x = 0.45986$  mm for type 1. This point is very close to the theoretical contact radius (0.462 mm) of the type 1 model. This can also explain to some extent why cracks always initiation at contact edges.

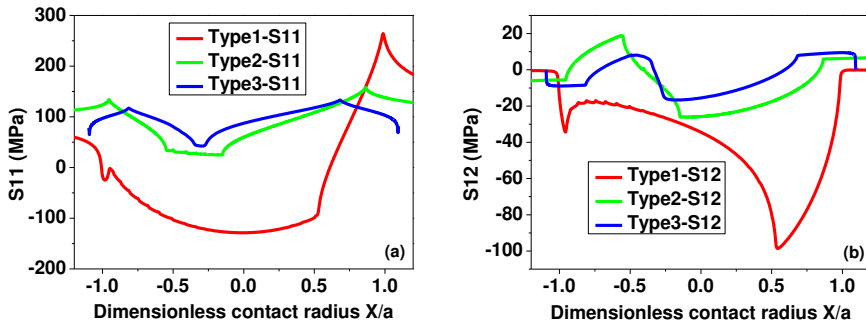


Figure 5.6. Contact surface stress distribution comparison between each model: (a) tensile stress and (b) shear stress

For the type 2 model, the maximum tensile stress is 157.992 MPa and located at  $x = 2.0402$  mm point as the theoretical contact radius is 2.36 mm. The peak point is farther away from the contact edge when it is compared with type 1. This also means that the initial position of the crack may change when the surface of the sample is treated by a pit. Moreover, for type 3 model, the maximum tensile stress (133.098 MPa) on the contact surface appears at  $x = 3.162$  mm point, which is smaller than the theoretical contact radius (4.645 mm). The peak value is just a little higher than the load (100 MPa) on the right side of the specimen. This shows that there is no particularly significant stress concentration in type 3 model. It also means that for type 3, the crack initiation position will be closer to the contact centre. Moreover, the peak value is less than half of type 1. The slope of tensile stress on the surface is also smaller than type 1. This indicates that type 3 model will have better fretting fatigue performance. From the result shown in Figure 5.6 (b), the maximum shear stress of type 1 model is  $-98.596$  MPa at  $x = 0.25$  mm point. This point is close to the boundary between the stick zone and the slip zone from the analytical result [107]. In addition, the shear stress changes very sharply around this point. For type 3 model, both positive and negative shear stresses appear at the contact surface, but because the contact area is relatively large, the resulting lateral friction is equal to that of type 1. This will inevitably lead to an absolute peak shear stress that will be much smaller than type 1. The value and position of peak point are

$-16.651$  MPa and  $x = -0.78795$  mm , respectively. This is likely to produce lower critical plane parameter values.

In general, specimen treated with pits (type 2 and type 3) have larger contact areas and smaller contact stress peaks. The stress distribution is completely different for the three models.

### 5.3.2 Critical Plane Parameter

The stress distribution is important in fretting fatigue analysis, but it just considers the peak load value. The critical plane criteria can take the stress and strain history of the specimen into account [147].

As shown in Figure 5.7, the three critical plane parameter values are larger near both contact edges and reach the peak value on the left side edge. For the convenience of comparison, all three parameters are presented in dimensionless form by dividing them by their maximum values. The maximum values of each critical plane parameter are listed in Table 5.1, including position, critical plane angle and the estimated initial life.

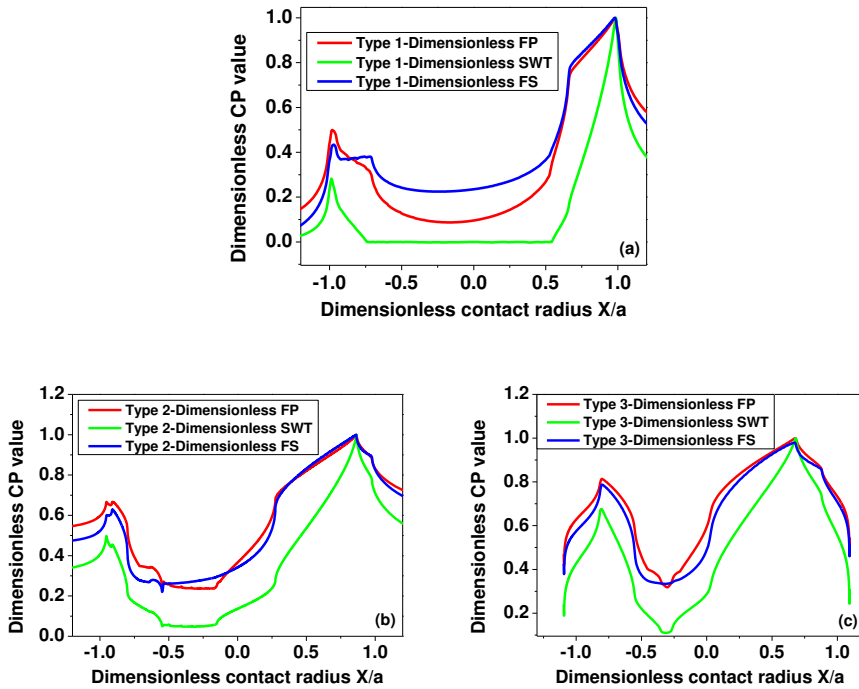


Figure 5.7. Dimensionless critical plane parameter distribution along the contact surface: (a) type 1 and (b) type 2 (c) type 3

Table 5.1: Detail results of the maximum critical plane parameter

Model	CP type	Peak_x (mm)	Peak_y (mm)	Peak CP value	CP angle ( $^{\circ}$ )	$N_i$
Type 1	FP	0.454	0	125.2543	34	625348
	SWT	0.454	0	0.67332	-3	552358
	FS	0.452	0	0.00437	39	919638
Type 2	FP	2.0382	-0.215	56.767	35	$2.378 \times 10^9$
	SWT	2.0382	-0.215	0.16725	0	$7.529 \times 10^8$
	FS	2.0342	-0.2152	0.00168	42	$8.958 \times 10^9$
Type 3	FP	3.1426	-0.15798	45.0121	35	$2.66655 \times 10^{10}$
	SWT	3.1426	-0.15678	0.10838	1	$7.20784 \times 10^9$
	FS	3.1426	-0.15798	0.00127	43	$1.42019 \times 10^{11}$

Although by comparing the three models, there has a large difference between each other, but for the same model, the peak positions of the three parameters are very close. It is around  $x = 0.453$  mm,  $x = 2.0363$  mm and  $x = 3.1426$  mm for type 1, type 2 and type 3 models, respectively. As mentioned in the previous section, the position of peak tensile stress on the contact surface is  $x = 0.45986$  mm,  $x = 2.04$  mm and  $x = 3.1684$  mm, respectively. It is clear that for all types of models, all damage parameters are dominated by tensile stress. In addition, because of the large difference in the stress and strain distribution of three models, the maximum value of the critical plane parameter also has a huge difference. The peak value of type 1 is more than two times larger than that of type 3. Therefore, the crack initiation lifetime also has a huge difference.

Regarding the critical plane angle, SWT parameter is mainly used for crack propagation under tensile load, so that the starting direction will be perpendicular to the direction of maximum tensile stress. However, the prediction of the other two kinds of parameters is reasonable compared with the previous experimental study [232]. When the specimen has been changed by adding pit on its surface, the predicted crack initiation life of type 2 and type 3 model will change a lot. These results mean that it will never fracture because the number of cycles to failure is more than  $10^7$  cycles [233].

5.3.3 Discussion

Type 2 and type 3 models have contact radius, which is several times larger than that of type 1. From the results above, it is clear that type 2 and type 3 models will be safer in accordance with the stress distribution and critical plane methods. On the other hand, it should be noted that the slip range of three models also has a huge difference as shown in Figure 5.8.

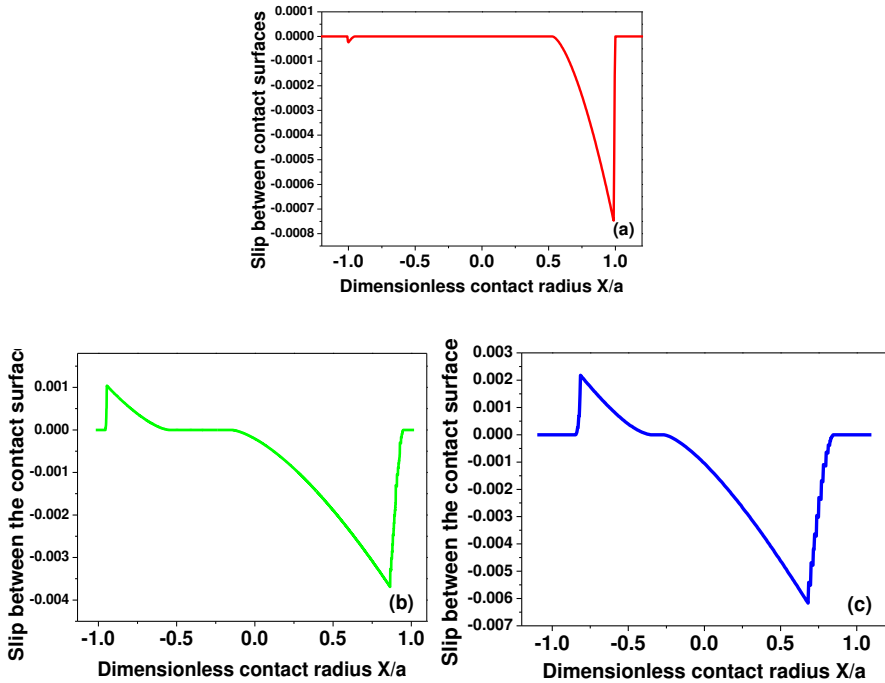


Figure 5.8. Slip range along the contact surface of both models: (a) type 1, (b) type 2 and (c) type 3

Even although, the amount of wear debris is not too much obvious in the partial slip situation [234], the effect of slip range also needs to be checked, because there are ten times differences between type 1 and type 3. Ruiz fatigue parameter that can take contact slip into account of initiation location is adopted [158]. As shown in Figure 5.9, the maximum absolute damage parameter value indicates the starting position of the crack. It can be seen that the critical plane method and the Ruiz rule have obtained very consistent predictions. However, although type 3 model has the smallest stress peak and the largest predicted crack initiation life, its absolute peak of Ruiz parameters is also the largest. Unfortunately, Ruiz's rule cannot predict life, but larger damage parameter values still indicate shorter life. It is worth noting that type 2 model has much less contact stress than type 1, and its Ruiz parameter is also smaller than type 1. Follow this idea, if it is possible to find a situation between those models to achieve the best performance of fretting fatigue and fretting wear. This will be the topic of our next study.

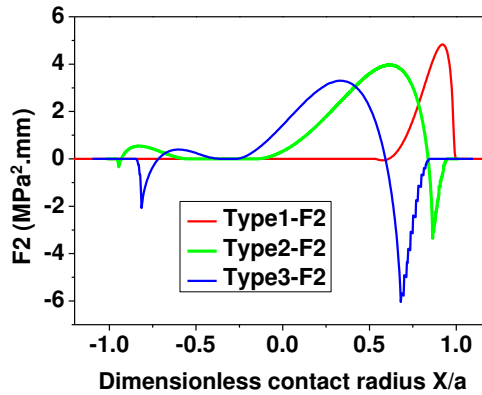


Figure 5.9. Ruiz F2 parameter along the contact surface

## 5.4 Summary

Based on the above results and discussion, we can draw the following conclusions.

Adding pits to the surface of the specimen can seriously affect the stress distribution of the specimen under the fretting fatigue loading condition and significantly reduce the stress concentration. Moreover, this effect is not linear, and different stress distributions are obtained with different pit radii.

Although the three critical plane parameters have a large difference in the prediction of life, the prediction of the crack initiation position is very consistent. The position of the peak point of CP parameter is very close to the location of peak tensile stress. For type 1 model (flat-specimen), the

---

crack will initial from the contact edge. However, for type 2 and type 3 model (pit- specimen), the crack position will shift inside contact area.

The critical plane method is acceptable for type 1 model (flat-specimen) compared with the experimental results. Moreover, FS parameter has the best prediction. The gradient of the SWT parameter is the largest. Furthermore, Ruiz parameter has a similar prediction initiation location compare with the critical plane method

## Chapter 6 The effect of stop hole

As introduced in chapter 2, many crack repair techniques are proposed to increase the crack propagation life time. In this chapter, a relatively simple and economical method called stop hole technology is applied to fretting fatigue specimens. There are three types of stop hole namely: tip hole, deflecting hole, and flank hole. Here the tip hole is considered, which is a drilling hole at the crack tip as shown in Figure 2.8 (a). Its main purpose is to reduce the stress concentration at the crack tip. As shown in Figure 6.1 (a), when a crack appears, it propagates with  $N_{p1}$  cycles. Then, a stop hole is drilled at the crack tip to initiate a second crack at  $N_{i2}$  cycles as shown in Figure 6.1 (b). Finally, the crack continues to propagate until the specimen breaks at  $N_{p2}$  cycles. In this way, the main crack needs to initiate again on the edge of the stop hole. So, the life time will extend obviously.

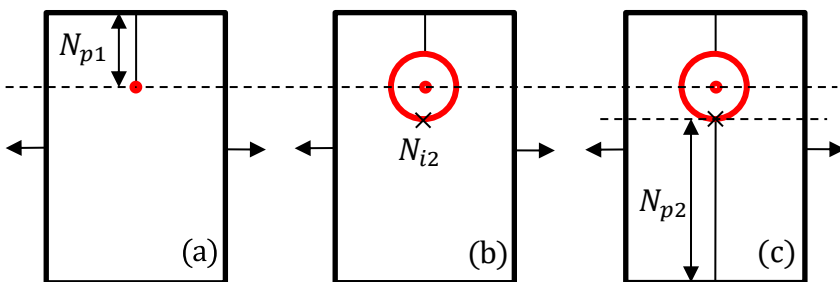


Figure 6.1. The process of drilling a stop hole and crack growth

In this chapter, the first crack initiation life  $N_i$  is not considered, because this has been discussed in previous chapters. Only the effect of stop hole on the propagation phase is studied. The propagation life is predicted by LEFM approach, which is the combination between Paris' law and numerical integration. The critical plane parameter and variable length TCD method are used to predict the second initiation lifetime.

## 6.1 Numerical model and Experimental validation

The literature review in chapter 2 has described all the involved numerical method used in this chapter. The framework of crack propagation life and path prediction is shown in Figure 2.16 and Figure 2.23. For the surface crack initiation phase, the validation part of chapter 4 has provided the prediction results as shown in Table 4.6. And here only the results obtained from the FS parameter are used as the initial condition of the FE crack propagation model. The initiation length for all cases is assumed to be equal to 50  $\mu\text{m}$  [45, 50]. As an example, for test 1, a short crack is inserted at the contact surface and  $x = 0.452$  mm. The initiation orientation is  $-51^\circ$  as shown in Table 4.6.

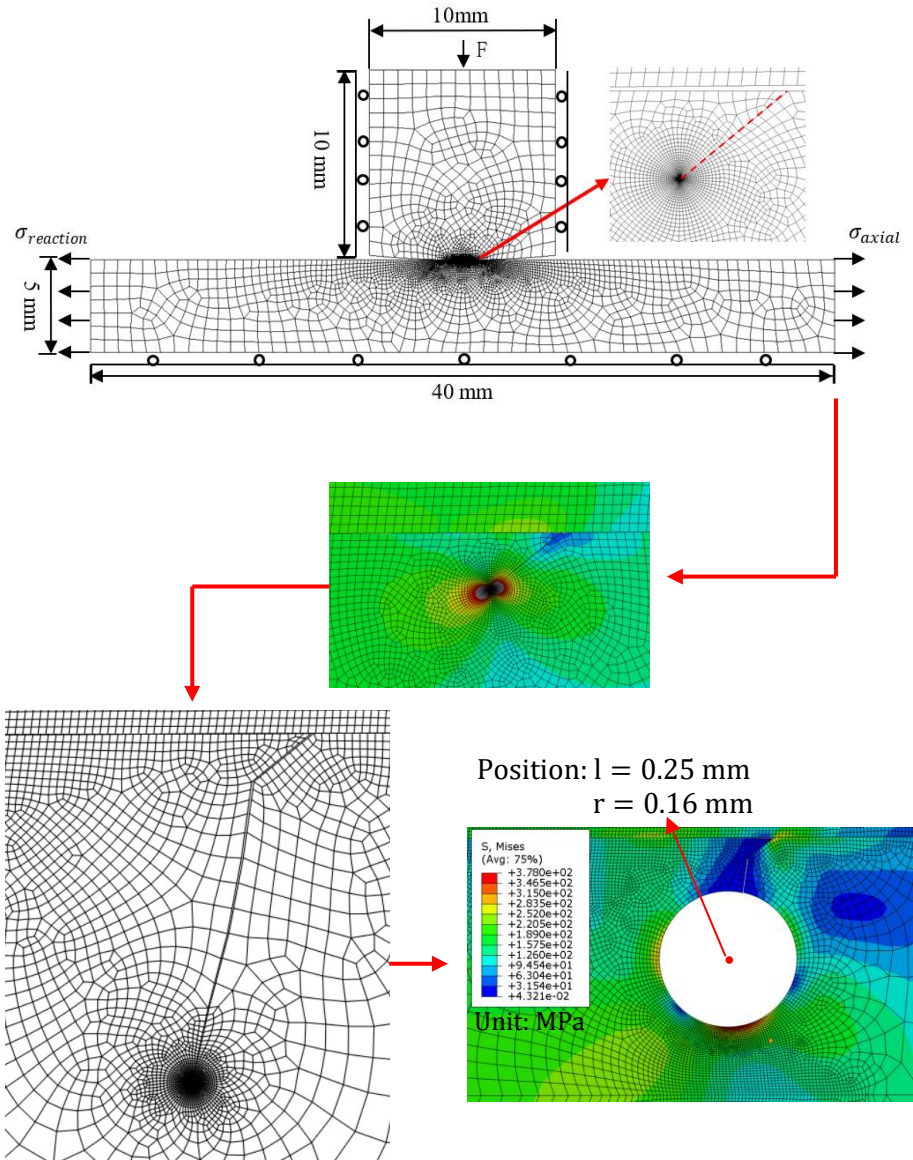


Figure 6.2. Crack propagation FE model

The conventional FEM with re-meshing technique is used to model the crack propagation phase as illustrated in Figure 6.2. The stress and strain fields around crack tip can be obtained by FEM. And the equivalent SIF range can be obtained from Eq. (2.34). The crack growth rate is calculated by Paris–Erdogan equation as shown in Eq. (2.32). And the integral form is shown in Eq. (2.33), which can be used to predict the fatigue life with crack length single iteration increment  $\Delta N$ . The maximum  $\Delta K_I^*(\theta)$  criteria is used to predict the crack growth orientation  $\theta_p$  as shown in Eq. (2.41). By selecting an appropriate crack increment  $da$ , the crack in the next iteration can be predicted using the stress state of the current crack tip. Here the length increment is set as 50  $\mu\text{m}$  for the first 25 increments. After that, the length increment is increased to 250  $\mu\text{m}$  until the final fracture. Then, stop holes of a specific location and size will be added to the crack tip as shown in Figure 6.2. The second crack initiates from the lower edge of the stop hole and propagates again.

### 6.1.1 Propagation path

The comparison between experimental observation and prediction is shown in Figure 6.3. It can be found that the crack path predicted by the maximum  $\Delta K_I^*(\theta)$  criteria is consistent with the experimental one.

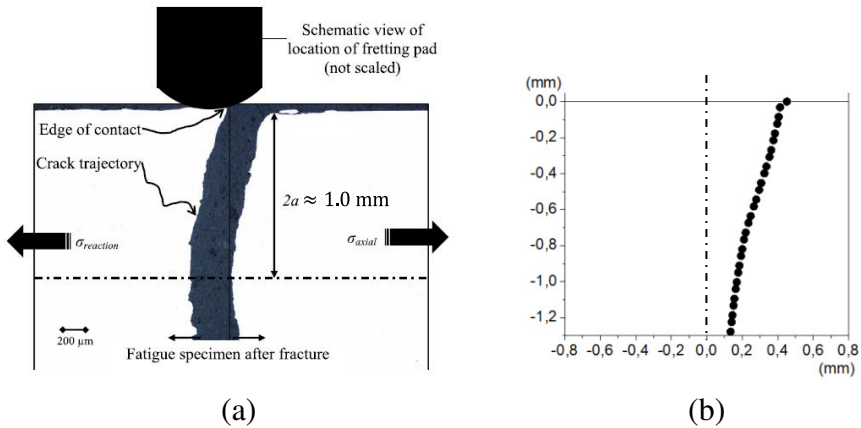


Figure 6.3. Crack propagation path of test 1 (a) experiment observation[45] and (b) prediction by our framework.

The crack is initiated at the contact edge, and due to the influence of contact surface friction, the crack deflects to the contact surface and propagates downward. As the crack propagates deeper and deeper, the effect decreases gradually. Finally, when the depth reaches twice the contact radius ( $2a \approx 1.0$  mm), the crack propagation orientation is almost vertical to the contact surface as shown in Figure 6.3.

### 6.1.2 Fatigue lifetime prediction

Another important index to verify the correctness of our code is the prediction of fatigue life. This includes crack propagation fatigue life and second crack initiation life as shown in Figure 6.1. In this chapter, the variable length TCD method (Eq. (2.25)) combined with FS parameter (Eq. (2.20)) is used to predict the second initiation lifetime  $N_{2i}$ . In order to

fit the parameters  $A$  and  $B$  in Eq. (2.25), we need to know the relationship between different initiation lives and critical distance. There are two methods to fit the two parameters  $A$  and  $B$ , which depend on material parameters and experimental data, respectively. Here the second method is adopted and the experimental data in Table 4.2 are used to reveal this relationship.

As introduced in chapter 2, total fatigue life includes two phases, initiation and propagation. It should be noted that the former refers to the initiation of cracks on the contact surface without considering the stop hole. And this initiation lifetime prediction has been presented in chapter 4. The predicted relationship between crack propagation life and crack length by our code is shown in Figure 6.4. It can be seen that when the crack length exceeds twice the contact radius ( $2a \approx 1.0$  mm), the propagation growth rate is very high until the specimen is completely fractured.

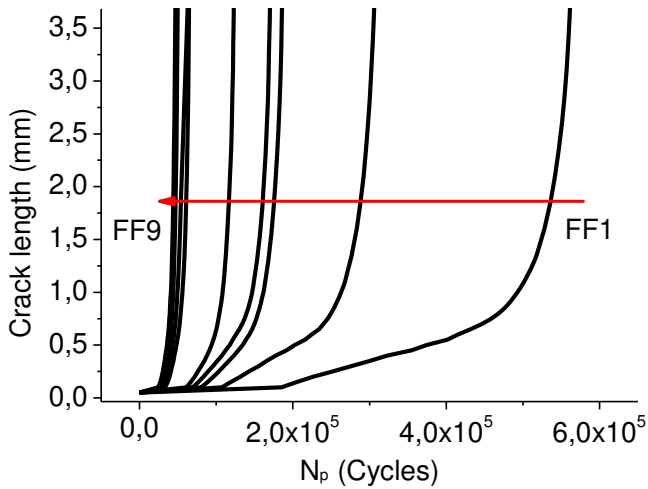


Figure 6.4. Variation of crack length with prediction crack propagation lifetime of FF 1 – FF 9

By combining the predicted crack propagation phase with the surface crack initiation in Chapter 4, we can compare the predicted total life and the experimental total life, as shown in Figure 6.5. It should be noted that the initial life is predicted by FS parameter. The averaging method is fixed length TCD ( $10 \mu\text{m}$ ).

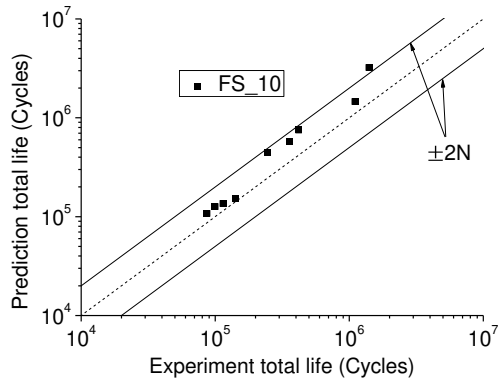


Figure 6.5. Comparison between the predicted and measured total life.

Two points can be observed in Figure 6.5. Firstly, the crack propagation life prediction method used in this chapter is good enough. Secondly, for the case of long fatigue life, the ratio between predicted and experimental data is high. In case 1, this ratio is even more than 2 times. In order to improve the prediction accuracy, here the variable length TCD is used. And the stress at a certain distance from the peak point on the critical plane is taken as the equivalent stress, which is called point method (PM). And the FS parameter gradient along the critical plane is shown in Figure 6.6.

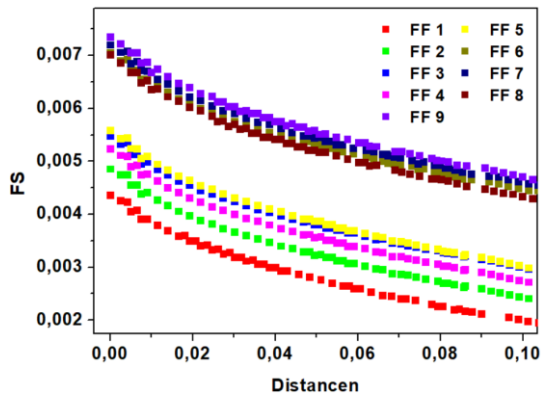


Figure 6.6. The FS parameter gradient along the critical plane.

The crack initiation life can be obtained by subtracting the propagation life predicted in this chapter from the total experimental life. According to the prediction performance of three critical plane parameters in Chapter 4, the FS parameter is used here. Calculating the initiation life from Eq. (2.20), the equivalent FS parameter is obtained. Then, combining the equivalent FS with Figure 6.6, the ideal critical distance under different conditions can be obtained. Finally, the relationship between the initiation life and the critical distance is obtained as shown in Figure 6.7.

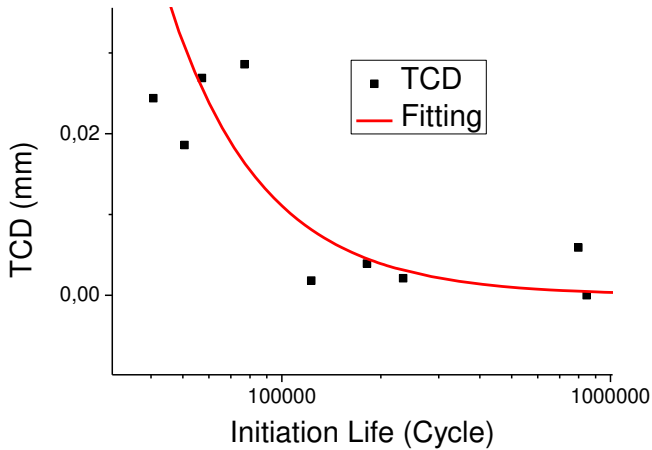


Figure 6.7. The relationship between TCD and initiation lifetime for Test 1 - Test 9.

It can be found that the larger the initiation life, the smaller the critical distance is. And the fitted line can express as:

$$l_c = 1 \times 10^6 N_i^{-1.5} \quad (6.1)$$

If the predicted initiation life using the variable length critical distance is added to the predicted total life, the comparison between the predicted and experimental results is shown in Figure 6.8. It shows that the new critical distance method is superior to the fixed length TCD in Chapter 4. The problem of large prediction error for high cycle fatigue for surface initiation is solved effectively.

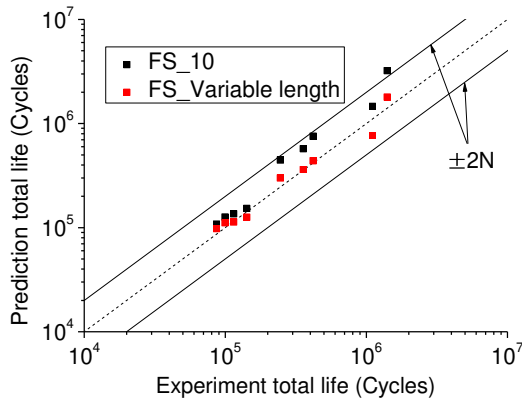


Figure 6.8. Comparison between the predicted and measured total life.

The parameters  $A$  and  $B$  in Eq. (2.25) are the material constants of different materials and different stress ratio [166]. In order to verify the accuracy of Eq. (6.1) used to predict the second initiation, here the experimental data reported in Nishimura [52] is used. Because their experimental material and stress ratio is AA2024-T3 and 0.1, respectively, which are the same as those in Table 4.2. If the fitting equation is correct, the variable length TCD in Eq. (6.1) is also applicable for this experiment. Their experiment depends on the centre cracked tension specimens (CCT) as shown in Figure 6.9.

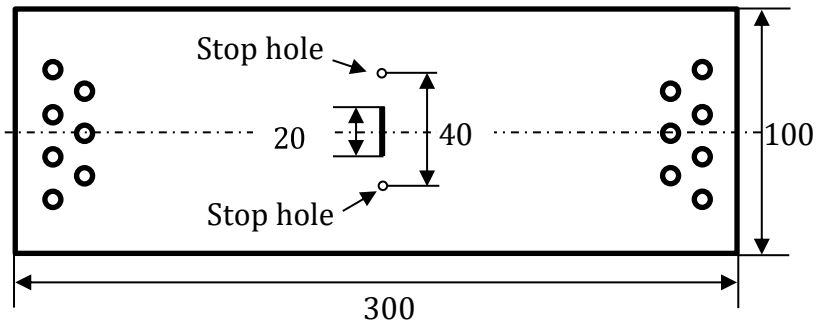


Figure 6.9. Configuration of crack growth test specimen [52].

The test conducted under maximum stress of 68.6 MPa with stress ratio  $R_s = 0.1$ . And the size of specimen is shown in Figure 6.9 and the thickness is 4.1 mm. So, the plane stress condition is assumed. A 20 mm length initial central crack is introduced by an electrical discharge machining. The diameter of stop hole is 4 mm. When the half crack length grows to 16 mm, the stop hole will be introduced at 4 mm ahead of the crack tip.

In practice, the FS parameter as shown in Eq. (2.20) combined with variable length TCD method as shown in Eq. (6.1) is adopted to predict the second initiation lifetime. The implementation method is presented in Figure 2.16 and Figure 2.23. And the prediction result using our code is shown in Figure 6.10.

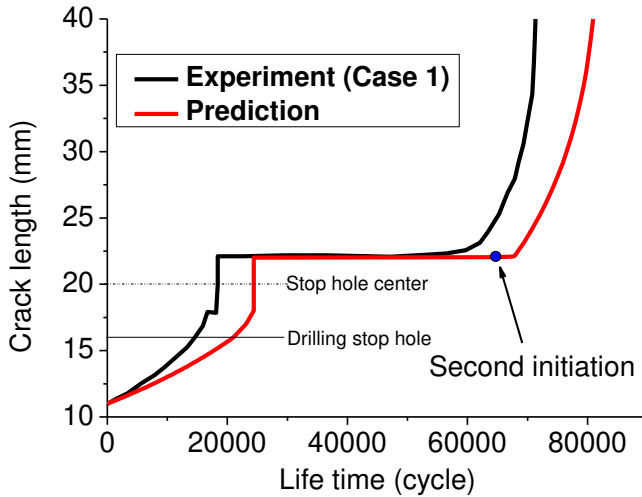


Figure 6.10. Comparison between the predicted and the experimental fatigue life for CCT case 1.

It shows that the difference in total fatigue life is less than 2 times. It is worth noting that the predicted value of the second initiation life is 40196, and the experimental value is about 41330. So, this means our code is suitable to predict the crack propagation and the second initiation in the stop hole case.

## 6.2 Results and discussion

The crack propagation stage of experiment Test 1 [45] is selected as the basic case of this study. When the crack propagates, the crack tip is drilled with different stop holes. As an example, a stop hole with radius  $r = 0.16$  mm is added at the crack tip when the crack length  $l = 0.30$  mm is

shown in Figure 6.11. The choice of crack length  $l$  depends on the increment step of Test 1 crack growth simulation.

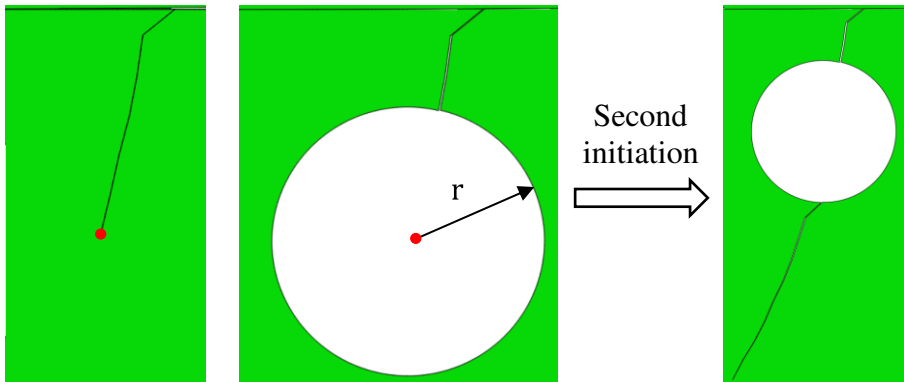


Figure 6.11. A stop hole with radius  $r = 0.16$  mm is added on the crack tip when the crack length  $l = 0.30$  mm.

So,  $l = 0.30$  mm corresponds to the sixth step of microcrack incremental iteration. As described in chapter 2, the crack increment length in the first is 25 iterations. The drilling positions considered in this thesis range from the crack tip in the third iteration to the crack tip in the 15<sup>th</sup> iteration. And the stop hole radius ranges  $r = 0.1$  mm from to  $r = 0.22$  mm.

### 6.2.1 Effect of drilling location

At first, in order to study the effect of drilling location,  $r = 0.16$  mm is considered. As shown in Figure 6.12, a stop hole with  $r = 0.16$  mm is drilled at three locations, when the crack length is equal to 0.25, 0.45 and 0.65 mm.

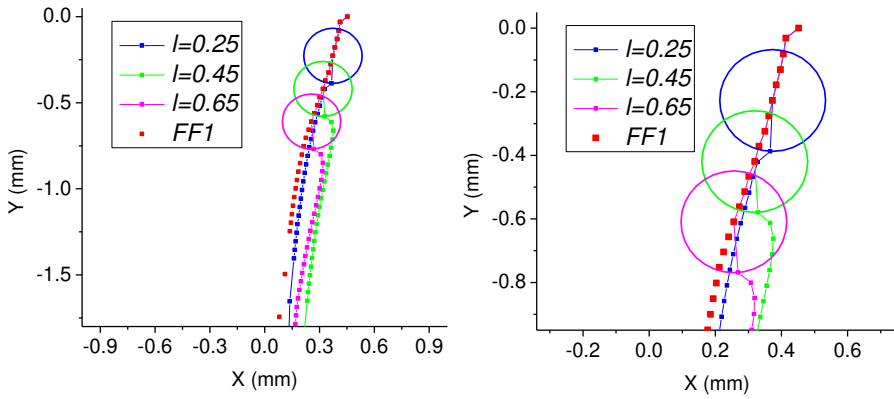


Figure 6.12. The effect of drilling location of stop hole on the crack propagation path.

It can be seen that the stop hole changes the crack propagation path. Especially after the second initiation, the crack starts at the lower edge of the hole again. And the relationship between propagation life and crack length is shown in Figure 6.13.

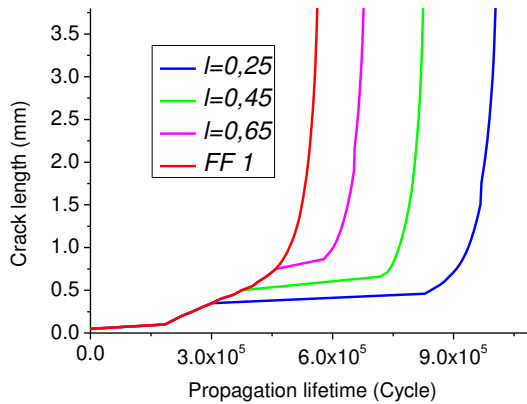


Figure 6.13. The effect of drilling location of stop hole on the crack propagation lifetime.

The closer the borehole to the contact surface, the longer the secondary initiation life is. Drilling the hole when the crack length is equal to 0.3, the ultimate propagation fatigue life is 1004805, which is almost two times that of Test 1 (562522). It can also be seen that when the secondary crack is long enough, the stop hole has little effect on the crack growth rate. Therefore, the increase of propagation life mainly comes from the secondary crack initiation.

In order to study the influence of drilling position on secondary initiation, two stop hole sizes are considered, i.e.  $r = 0.1$  mm and  $r = 0.16$  mm. As shown in Figure 6.14, when the size of the stop hole is constant, the second initiation life first increases and then decreases with the drilling position gradually under the contact surface.

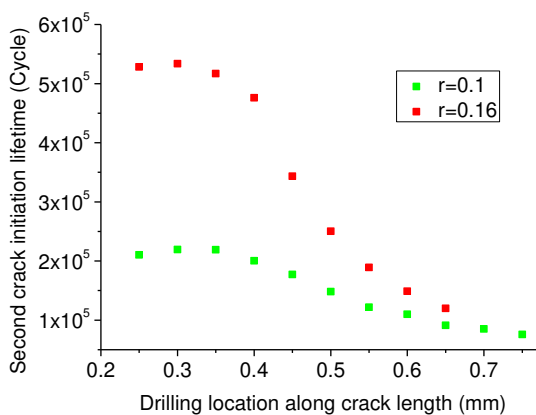


Figure 6.14. The effect of drilling location of stop hole on the second crack initiation lifetime.

And the initial increase ( $l = 0.25$  mm for  $r = 0.1$  mm and  $r = 0.16$  mm) and the final decrease (after  $l = 0.7$  mm) are not very obvious. In the beginning, because the hole is very close to the surface, the material above the hole is not thick, and the ability to share the axial tensile stress is limited. The case when the hole is too far away from the contact surface, which is the nonlocal plasticity case, is not considered in this thesis. The second initiation life is more sensitive to the position change when the stop hole lies between the two extreme cases.

### 6.2.2 Effect of stop hole size

In a proper range, the closer the drilling position to the contact surface, the more obvious the effect of the stop hole to prolong the service life is. And here the effect of hole size drilling at the same location on the fatigue life is also discussed. Five kinds of hole sizes range from 0.14 mm to 0.22 mm are considered at the tip when the crack length  $l = 0.30$  mm. As shown in Figure 6.15 (a), different hole sizes lead to different crack propagation path.

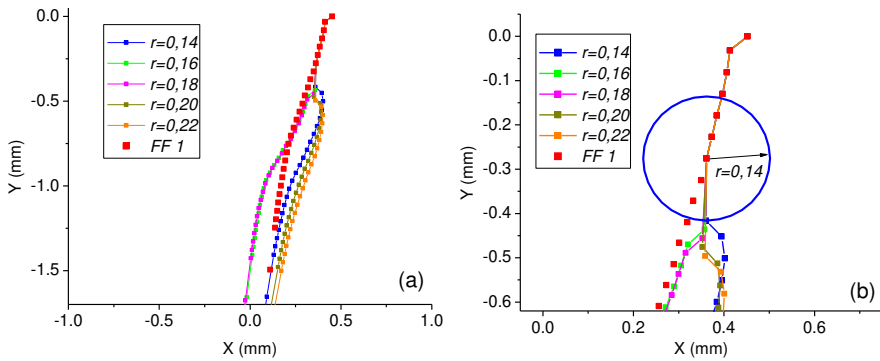


Figure 6.15. The effect of hole size on the crack propagation path.

As shown in Figure 6.15 (b), about  $r = 0.14$  mm case, because of the second crack initiation direction to the right, the crack will continue to the right and then gradually extend to the left. A similar growth path appears in the case of  $r = 0.20$  mm and  $r = 0.22$  mm. On the other hand, for case  $r = 0.16$  mm and  $r = 0.18$  mm, the second crack initiation to the left side. All those different crack propagation paths will affect the propagation lifetime.

The comparison of the total lifetime between stop hole cases and the homogeneous case is shown in Figure 6.16. The fatigue life can be effectively prolonged by adding stop hole at this position. Compared with Test 1, the life of  $r = 0.22$  mm case is increased 2.35 times. In general, the larger the size of the stop hole, the greater the fatigue life. However, comparing  $r = 0.18$  mm with  $r = 0.20$  mm, it is found that although the latter has a larger secondary crack initiation life, the former has a larger secondary crack propagation life, result in the total fatigue life of  $r =$

0.18 mm more than  $r = 0.20$  mm. Combined with the crack propagation path in Figure 6.15 (a) above, it can be found that when the crack extends to the left, the crack growth is slower, as  $r = 0.16$  mm and  $r = 0.18$  mm cases.

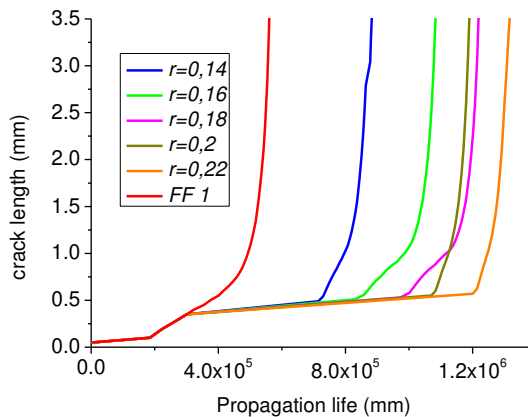


Figure 6.16. The effect of hole size of stop hole on the crack propagation lifetime.

The effect of hole size on the second crack initiation lifetime is shown in Figure 6.17. The larger the hole size, the smaller the stress concentration will be, so the second initiation life will be larger. Moreover, as shown in Figure 6.15 (b), the secondary cracks often initiate at the lower edge of the stop hole, so it is necessary to optimize the geometry of the hole, which will be our future research direction.

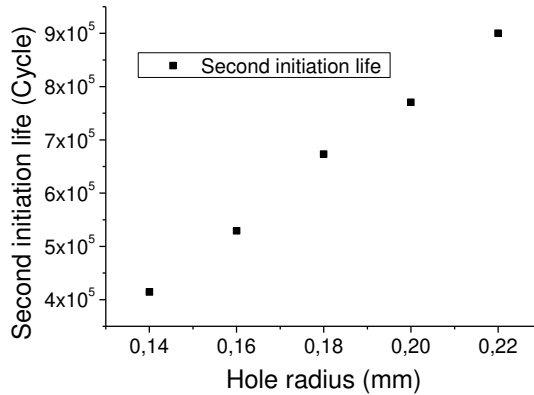


Figure 6.17. The effect of hole size on the second crack initiation.

### 6.3 Summary

From the above discussion, some conclusions can be drawn.

It can be seen that the stop hole changes the propagation path and initiation again from the lower edge of hole. And the increase of propagation life mainly comes from the second crack initiation. With the same hole diameter, the secondary initiation life increases slightly with the increase of the distance between the drilling position and the contact surface. Until it reaches the peak value, then the secondary initiation life will decrease rapidly with the increase of the drilling distance. When the drilling position is far enough from the contact surface, the influence of the change of the distance on the initiation life becomes not obvious. In general, the larger the size of the stop hole, the greater the fatigue life is. This is due to the smaller stress concentration at lower edge of hole, so the

---

optimization design of hole shape is a good future research direction. And it can be seen that when the crack extends to the left, the crack growth is slower. Therefore, the larger size of the stop hole case may also get a smaller total fatigue life due to the second crack initiation to the right side.

## **Chapter 7      Conclusion and Outlook**

In this thesis, the effects of some microstructure and macrostructure on fretting fatigue behaviour are discussed. Different stress distributions lead to different crack initiation and propagation responses. The appearance of stress concentration makes the fatigue life of structure uncertain. Some structures will cause greater stress concentration, while others will reduce this phenomenon. Through this thesis, the influence of typical microstructure and macrostructure on fretting fatigue is discussed.

### **7.1 Conclusion**

Firstly, the effect of random inclusions on the stress distribution in the specimen is studied in chapter 3. The RVE method is used to obtain macro material properties of specimen containing inclusions. And this macro property is used to replace the material property of the specimen far away from the contact area. The specimen is considered as a heterogeneous material with randomly distributed inclusions. Due to the randomness of inclusion distribution, fatigue crack nucleation depends on the most dangerous critical inclusion or other defects. And void will cause larger stress and more randomness of stress distribution than inclusion.

So, the effect of critical micro-void on the fretting fatigue initiation life of heterogeneous materials is studied in chapter 4. Critical micropores of different positions, sizes and shapes are considered. Three kind of critical plane parameters and critical distance method are combined to predict the crack initiation lifetime. It is shown that the presence of material heterogeneity (critical micro-void) has a strong influence on the distribution of damage parameters below the contact surface of the specimen. But for most heterogeneous materials, the crack initiation position and crack plane angle are similar to the homogeneous case. The existence of critical micro-void will cause the change of stress concentration and the decrease of crack initiation life. However, when the critical void is located below the left side of the contact edge or near the right side of the contact edge, the initiation life will increase. These two areas called enhancement zones. When the micro void is located in the enhancement region, the initiation life increases first and then decreases with the increase of void diameter. Otherwise, the larger the void, the shorter the initiation life will be..

In addition to the inclusions and micro void inside the specimen, the shape of the contact surface also affects the contact stress distribution. Chapter 5 analyses the effect of surface treatment on fretting fatigue specimen by numerical simulations using Finite Element Analysis. The processed specimen is a cylindrical pit added on its contact surface manually. Different pit diameters lead to different contact radii. Both

crack initiation life and angle are predicted by the critical plane approach. And the Ruiz parameter is used to consider the effect of the contact slip. The simulation shows that adding pit to the surface of the specimen can significantly reduce the stress concentration. The position of the peak point of CP parameter is close to the location of peak tensile stress. For the pitting specimen cases, the peak point shifts from the contact edge to the contact zone. Ruiz parameter has a similar prediction initiation location compare with the critical plane method. suitable pitting radius, the pit treatment can result in a lower peak value of CP and Ruiz parameter.

In order to prolong the service life of components, the crack propagation life can be extended in addition to the crack initiation stage. In chapter 6, a relatively simple and economical method called stop hole technology is applied to fretting fatigue problem. Generally, the fatigue process includes crack initiation and propagation. When the stop hole is considered, a second crack initiation will occur at the hole edge, which can prolong the fatigue life considerably. Remeshing technology and LEFM are used to predict crack propagation lifetime (Paris' law and numerical integration). The crack growth orientation is predicted by the maximum  $\Delta K_I^*(\theta)$  criterion. And the critical plane parameter and variable length TCD method are used to predict the second initiation lifetime. The result shows that the stop hole changes the propagation path and initiates another crack at the lower edge of hole. The increase of propagation life mainly comes from the secondary crack initiation. And the closer the borehole to

the contact surface, the longer the second initiation life is. In general, the larger the size of the stop hole, the greater the fatigue life is. This is due to the smaller stress concentration at the lower edge of the hole. However, when the crack extends to the left, the crack growth is slower. Therefore, the larger size of the stop hole case may also get a smaller total fatigue life due to the second crack initiation to the right side.

## 7.2 Outlook

This thesis focuses on the influence of microstructure and macrostructure on fretting fatigue. So it aims to find an effective way to avoid too fast fatigue failure, and even extend the fatigue life of crack initiation and propagation. Although some interesting conclusions have been obtained, there are still some directions worthy of further study.

In chapter 3, aiming at the inclusions with different sizes, shapes and properties, the influence of randomly distributed micro inclusions on the fretting fatigue properties of heterogeneous materials is analysed by finite element method. However, the grain boundaries have effect on the stress distribution. And in the materials science, the use crystal plastic theory combination with FEM simulation (CPFEM) to study both effects of inclusion and grain boundaries is required. Some researches used CPFEM to predict the crack initiation location and orientation without

---

considering inclusions. So, studying the combined effect is a very interesting and challenging direction.

Specimen with cylindrical pits on the surface are studied in Chapter 5. The fatigue life predicted by the critical plane method is consistent with the experimental results, but the existence of pits will increase the sliding range of the contact surface. Although the influence of relative sliding is also considered by Ruiz parameter, the method that can consider fretting wear to predict fatigue life needs to be established.

Finally, in Chapter 6, the stop hole technique is used to extend the crack propagation life. The location and size of the stop hole are very important for the secondary crack initiation. And the traditional drilling technology is often easier to achieve the round hole, but the hole shape optimization for specific loading is also a very effective way to extend the service life.



## Appendix

### List of A1 publications

1. Deng Q, Bhatti N, Yin X, Abdel Wahab M. Numerical modeling of the effect of randomly distributed inclusions on fretting fatigue-induced stress in metals[J]. *Metals*, 2018, 8(10): 836.
2. Deng Q, Bhatti N A, Yin X, Abdel Wahab M. The effect of a critical micro-void defect on fretting fatigue crack initiation in heterogeneous material using a multiscale approach[J]. *Tribology International*, 2020, 141: 105909.
3. Deng Q, Yin X, Abdel Wahab M. The Effect of Surface Pit Treatment on Fretting Fatigue Crack Initiation[J]. *Computers, Materials & Continua*, 2021, 66(1): 659-673.

## References

1. Ding, J., S. Leen, and I. McColl, *The effect of slip regime on fretting wear-induced stress evolution*. International journal of fatigue, 2004. **26**(5): p. 521-531.
2. Jeung, H.-K., J.-D. Kwon, and C.Y. Lee, *Crack initiation and propagation under fretting fatigue of inconel 600 alloy*. Journal of Mechanical Science and Technology, 2015. **29**(12): p. 5241-5244.
3. Nishioka, K. and K. Hirakawa, *Fundamental investigations of fretting fatigue: part 4, the effect of mean stress*. Bulletin of JSME, 1969. **12**(51): p. 408-414.
4. Wang, R., V. Jain, and S. Mall, *A non-uniform friction distribution model for partial slip fretting contact*. Wear, 2007. **262**(5): p. 607-616.
5. Tsai, C. and S. Mall, *Elasto-plastic finite element analysis of fretting stresses in pre-stressed strip in contact with cylindrical pad*. Finite elements in analysis and design, 2000. **36**(2): p. 171-187.
6. Goh, C.-H., et al., *Polycrystal plasticity simulations of fretting fatigue*. International Journal of Fatigue, 2001. **23**: p. 423-435.
7. Goh, C.-H., D. McDowell, and R. Neu, *Plasticity in polycrystalline fretting fatigue contacts*. Journal of the Mechanics and Physics of Solids, 2006. **54**(2): p. 340-367.
8. Shin, K.S., *Prediction of fretting fatigue behavior under elastic-plastic conditions*. Journal of mechanical science and technology, 2009. **23**(10): p. 2714-2721.
9. Talemi, R.H. and M.A. Wahab, *Finite element analysis of localized plasticity in Al 2024-T3 subjected to fretting fatigue*. Tribology transactions, 2012. **55**(6): p. 805-814.
10. Pereira, K., et al., *On the convergence of stresses in fretting fatigue*. Materials, 2016. **9**(8): p. 639.

11. Martínez, J.C., L.V. Vanegas Useche, and M.A. Wahab, *Numerical prediction of fretting fatigue crack trajectory in a railway axle using XFEM*. International Journal of Fatigue, 2017. **100, Part 1**: p. 32-49.
12. Ferjaoui, A., et al., *Prediction of fretting fatigue crack initiation in double lap bolted joint*. INTERNATIONAL JOURNAL OF FATIGUE, 2015. **73**: p. 66-76.
13. Nishikawa, H. and N. Maruyama, *Mechanical testing of metallic biomaterials*, in *Metals for Biomedical Devices*. 2019, Elsevier. p. 189-211.
14. Buciumeanu, M., et al., *Design improvement of an automotive-formed suspension component subjected to fretting fatigue*. Engineering Failure Analysis, 2007. **14(5)**: p. 810-821.
15. Hojjati-Talemi, R., A. Zahedi, and P. De Baets, *Fretting fatigue failure mechanism of automotive shock absorber valve*. International Journal of Fatigue, 2015. **73**: p. 58-65.
16. Jiménez-Peña, C., et al., *Investigations on the fretting fatigue failure mechanism of bolted joints in high strength steel subjected to different levels of pre-tension*. Tribology International, 2017. **108**: p. 128-140.
17. Mangardich, D., F. Abrari, and Z. Fawaz, *A fracture mechanics based approach for the fretting fatigue of aircraft engine fan dovetail attachments*. International Journal of Fatigue, 2019. **129**: p. 105213.
18. Guo, T., et al., *Experimental study on fretting-fatigue of bridge cable wires*. International Journal of Fatigue, 2020. **131**: p. 105321.
19. Ciavarella, M. and G. Demelio, *A review of analytical aspects of fretting fatigue, with extension to damage parameters, and application to dovetail joints*. International Journal of Solids and Structures, 2001. **38(10-13)**: p. 1791-1811.
20. Farris, T., M. Szolwinski, and G. Harish, *Fretting in aerospace structures and materials*, in *Fretting Fatigue: Current Technology and Practices*. 2000, ASTM International.
21. Hoepfner, D.W., *Fretting fatigue case studies of engineering components*. Tribology International, 2006. **39(10)**: p. 1271-1276.
22. Hills, D.A., *Mechanics of fretting fatigue*. Wear, 1994. **175(1-2)**: p. 107-113.

23. Vingsbo, O. and S. Söderberg, *On fretting maps*. Wear, 1988. **126**(2): p. 131-147.
24. Deng, Q., et al., *Numerical Modeling of the Effect of Randomly Distributed Inclusions on Fretting Fatigue-Induced Stress in Metals*. 2018. **8**(10): p. 836.
25. Hojjati-Talemi, R., et al., *Prediction of fretting fatigue crack initiation and propagation lifetime for cylindrical contact configuration*. 2014. **76**: p. 73-91.
26. Bhatti, N.A. and M.A. Wahab, *Fretting fatigue crack nucleation: A review*. Tribology International, 2018. **121**: p. 121-138.
27. Bhatti, N.A., K. Pereira, and M.A. Wahab, *A continuum damage mechanics approach for fretting fatigue under out of phase loading*. Tribology International, 2017. **117**.
28. Pereira, K. and M. Abdel Wahab, *Fretting fatigue crack propagation lifetime prediction in cylindrical contact using an extended MTS criterion for non-proportional loading*. Tribology International, 2017. **115**: p. 525-534.
29. Yang, B. and S. Mall, *Mechanics of two-stage crack growth in fretting fatigue*. Engineering fracture mechanics, 2008. **75**(6): p. 1507-1515.
30. Giner, E., et al., *Extended finite element method for fretting fatigue crack propagation*. International Journal of Solids and Structures, 2008. **45**(22-23): p. 5675-5687.
31. Yue, T. and M.A. Wahab, *Finite element analysis of fretting wear under variable coefficient of friction and different contact regimes*. Tribology International, 2017. **107**: p. 274-282.
32. Yue, T. and M. Abdel Wahab, *A numerical study on the effect of debris layer on fretting wear*. Materials, 2016. **9**(7): p. 597.
33. Bhatti, N.A. and M.A. Wahab, *Finite element analysis of fretting fatigue under out of phase loading conditions*. Tribology International, 2017. **109**: p. 552-562.
34. Yue, T. and M.A. Wahab, *Finite element analysis of stress singularity in partial slip and gross sliding regimes in fretting wear*. Wear, 2014. **321**: p. 53-63.
35. Tobi, A.M., W. Sun, and P. Shipway, *Investigation on the plasticity accumulation of Ti-6Al-4V fretting wear by decoupling the effects of*

- wear and surface profile in finite element modelling. *Tribology International*, 2017. **113**: p. 448-459.
36. Alfredsson, B. and A.J.I.j.o.f. Cadario, *A study on fretting friction evolution and fretting fatigue crack initiation for a spherical contact*. 2004. **26**(10): p. 1037-1052.
  37. Findley, W.N., J. Coleman, and B. Hanley, *Theory for combined bending and torsion fatigue with data for SAE4340 steel*. 1956: Division of Engineering, Brown University.
  38. Fatemi, A., et al., *A critical plane approach to multiaxial fatigue damage including out - of - phase loading*. 1988. **11**(3): p. 149-165.
  39. Bhatti, N.A. and M.A.J.T.I. Wahab, *Fretting fatigue crack nucleation: A review*. 2018. **121**: p. 121-138.
  40. Namjoshi, S.A., et al., *Fretting fatigue crack initiation mechanism in Ti-6Al-4V*. 2002. **25**(10): p. 955-964.
  41. Tanaka, K., *Fatigue crack propagation from a crack inclined to the cyclic tensile axis*. *Engineering Fracture Mechanics*, 1974. **6**(3): p. 493-507.
  42. Irwin, G.R., *Analysis of stresses and strains near the end of a crack transversing a plate*. *Trans. ASME, Ser. E, J. Appl. Mech.*, 1957. **24**: p. 361-364.
  43. Richard, H.A., et al. *2D-and 3D-mixed mode fracture criteria*. in *Key Engineering Materials*. 2003. Trans Tech Publ.
  44. Richard, H., B. Schramm, and N.-H. Schirmeisen, *Cracks on mixed mode loading—theories, experiments, simulations*. *International Journal of Fatigue*, 2014. **62**: p. 93-103.
  45. Hojjati-Talemi, R., et al., *Prediction of fretting fatigue crack initiation and propagation lifetime for cylindrical contact configuration*. *Tribology International*, 2014. **76**: p. 73-91.
  46. Boljanović, S. and S. Maksimović, *Analysis of the crack growth propagation process under mixed-mode loading*. *Engineering Fracture Mechanics*, 2011. **78**(8): p. 1565-1576.
  47. RICHARD, H.A., M. Fulland, and M. Sander, *Theoretical crack path prediction*. *Fatigue & fracture of engineering materials & structures*, 2005. **28**(1 - 2): p. 3-12.

48. Miranda, A., et al., *Fatigue life and crack path predictions in generic 2D structural components*. Engineering Fracture Mechanics, 2003. **70**(10): p. 1259-1279.
49. Hourlier, F., et al., *Fatigue crack path behavior under polymodal fatigue*, in *Multiaxial fatigue*. 1985, ASTM International.
50. Pereira, K. and M.A. Wahab, *Fretting fatigue crack propagation lifetime prediction in cylindrical contact using an extended MTS criterion for non-proportional loading*. Tribology International, 2017. **115**: p. 525-534.
51. Liu, K.K. and M.R. Hill, *The effects of laser peening and shot peening on fretting fatigue in Ti-6Al-4V coupons*. Tribology International, 2009. **42**(9): p. 1250-1262.
52. Nishimura, T., *Experimental and numerical evaluation of crack arresting capability due to a dimple*. J. Eng. Mater. Technol., 2005. **127**(2): p. 244-250.
53. Kumar, D., et al., *Fretting fatigue stress analysis in heterogeneous material using direct numerical simulations in solid mechanics*. Tribology International, 2017. **109**: p. 124-132.
54. Amuzuga, K.V., et al., *Fully Coupled Resolution of Heterogeneous Elastic-Plastic Contact Problem*. Journal of Tribology, 2016. **138**(2): p. 021403.
55. Beveridge, A.J., M. Wheel, and D. Nash, *A higher order control volume based finite element method to predict the deformation of heterogeneous materials*. Computers & Structures, 2013. **129**: p. 54-62.
56. Toro, S., et al., *A two - scale failure model for heterogeneous materials: numerical implementation based on the finite element method*. International Journal for Numerical Methods in Engineering, 2014. **97**(5): p. 313-351.
57. Roubin, E., et al., *Multi-scale failure of heterogeneous materials: A double kinematics enhancement for Embedded Finite Element Method*. International Journal of Solids and Structures, 2015. **52**: p. 180-196.

58. You, Y., X. Kou, and S. Tan, *Adaptive meshing for finite element analysis of heterogeneous materials*. Computer-Aided Design, 2015. **62**: p. 176-189.
59. Murakami, Y. and M. Endo, *Effects of defects, inclusions and inhomogeneities on fatigue strength*. International journal of fatigue, 1994. **16**(3): p. 163-182.
60. Maiti, S.N. and K.K. Sharma, *Studies on polypropylene composites filled with talc particles*. Journal of Materials Science, 1992. **27**(17): p. 4605-4613.
61. Zhu, Y. and H.A. Kishawy, *Influence of alumina particles on the mechanics of machining metal matrix composites*. International Journal of Machine Tools & Manufacture, 2005. **45**(4): p. 389-398.
62. Gall, K., et al., *On the driving force for fatigue crack formation from inclusions and voids in a cast A356 aluminum alloy*. International Journal of Fracture, 2001. **108**(3): p. 207-233.
63. Chan, L., X. Lu, and K. Yu, *Multiscale approach with RSM for stress-strain behaviour prediction of micro-void-considered metal alloy*. Materials & Design, 2015. **83**: p. 129-137.
64. Chan, K.S., *Roles of microstructure in fatigue crack initiation*. International Journal of Fatigue, 2010. **32**(9): p. 1428-1447.
65. Wang, Q., D. Apelian, and D.J.J.o.l.m. Lados, *Fatigue behavior of A356-T6 aluminum cast alloys. Part I. Effect of casting defects*. 2001. **1**(1): p. 73-84.
66. Matzenmiller, A., J. Lubliner, and R.L. Taylor, *A constitutive model for anisotropic damage in fiber-composites*. Mechanics of Materials, 1995. **20**(2): p. 125-152.
67. Jiménez, F.L. and S. Pellegrino, *Folding of fiber composites with a hyperelastic matrix*. International Journal of Solids and Structures, 2012. **49**(3-4): p. 395-407.
68. Sager, R., et al., *Effect of carbon nanotubes on the interfacial shear strength of T650 carbon fiber in an epoxy matrix*. Composites Science and Technology, 2009. **69**(7-8): p. 898-904.
69. Wood, C.D., et al., *Nanoscale structure and local mechanical properties of fiber-reinforced composites containing MWCNT-grafted*

- hybrid glass fibers*. Composites Science and Technology, 2012. **72**(14): p. 1705-1710.
70. López-Realpozo, J.C., et al., *Effective elastic shear stiffness of a periodic fibrous composite with non-uniform imperfect contact between the matrix and the fibers*. International Journal of Solids and Structures, 2014. **51**(6): p. 1253-1262.
71. Marshall, D.B., B.N. Cox, and A.G. Evans, *The mechanics of matrix cracking in brittle-matrix fiber composites*. Acta Metallurgica, 1985. **33**(11): p. 2013-2021.
72. Murakami, Y. and M.J.I.j.o.f. Endo, *Effects of defects, inclusions and inhomogeneities on fatigue strength*. 1994. **16**(3): p. 163-182.
73. Lados, D., D. Apelian, and A. De Figueredo. *Fatigue performance of high integrity cast aluminum components*. in *Proceedings of the 2 International Aluminum Casting Technology Symposium*. 2004.
74. Szolwinski, M.P. and T.N. Farris, *Observation, analysis and prediction of fretting fatigue in 2024-T351 aluminum alloy*. Wear, 1998. **221**(1): p. 24-36.
75. Johnson, K.L. and K.L. Johnson, *Contact mechanics*. 1987: Cambridge university press.
76. Hertz, H., *Ueber die Berührung fester elastischer Körper*. Journal für die reine und angewandte Mathematik, 1882. **1882**(92): p. 156-171.
77. Cao, J., et al., *Non-uniform virtual material modeling on contact interface of assembly structure with bolted joints*. Structural Engineering and Mechanics, 2019. **72**(5): p. 557-568.
78. Brake, M., *The role of epistemic uncertainty of contact models in the design and optimization of mechanical systems with aleatoric uncertainty*. Nonlinear Dynamics, 2014. **77**(3): p. 899-922.
79. Wang, H., et al., *Experimental and theoretical analyses of elastic-plastic repeated impacts by considering wave effects*. European Journal of Mechanics-A/Solids, 2017. **65**: p. 212-222.
80. Wang, H., et al., *The correlation of theoretical contact models for normal elastic-plastic impacts*. International Journal of Solids Structures, 2020. **182**: p. 15-33.
81. Alfredsson, B. and E. Nordin, *An elastic-plastic model for single shot-peening impacts*. Tribology letters, 2013. **52**(2): p. 231-251.

82. McCarthy, B., et al., *A dynamic model, including contact bounce, of an electrostatically actuated microswitch*. Journal of microelectromechanical systems, 2002. **11**(3): p. 276-283.
83. Sadeghi, F., et al., *A review of rolling contact fatigue*. Journal of tribology, 2009. **131**(4): p. 041403.
84. Ding, Y., W.-K. Yuan, and G.-F. Wang, *Spherical indentation on biological films with surface energy*. Journal of Physics D: Applied Physics, 2018. **51**(29): p. 295401.
85. Hertz, H., *Über die berührung fester elastische körper und über die harte (On the contact of rigid elastic solids and on hardness)*. Verhandlungen des Vereins zur Beförderung des Gewerbfleißes, Leipzig, 1882.
86. Cattaneo, C., *Sul contatto di due corpi elastici: distribuzione locale degli sforzi*. Rend. Accad. Naz. Lincei, 1938. **27**(6): p. 342-348.
87. Mindlin, R.D., *Elastic spheres in contact under varying oblique forces*. Trans. ASME, J. Appl. Mech., 1953. **20**: p. 327-344.
88. Mutoh, Y., *Mechanisms of fretting fatigue*. JSME international journal. Ser. A, Mechanics and material engineering, 1995. **38**(4): p. 405-415.
89. Namjoshi, S.A., et al., *Fretting fatigue crack initiation mechanism in Ti-6Al-4V*. Fatigue & Fracture of Engineering Materials & Structures, 2002. **25**(10): p. 955-964.
90. Lykins, C.D., S. Mall, and V. Jain, *An evaluation of parameters for predicting fretting fatigue crack initiation*. International Journal of Fatigue, 2000. **22**(8): p. 703-716.
91. McVeigh, P. and T. Farris, *Finite element analysis of fretting stresses*. 1997.
92. Merati, A., *A study of nucleation and fatigue behavior of an aerospace aluminum alloy 2024-T3*. International Journal of Fatigue, 2005. **27**(1): p. 33-44.
93. Majzoobi, G. and F. Abbasi, *On the effect of contact geometry on fretting fatigue life under cyclic contact loading*. Tribology Letters, 2017. **65**(4): p. 125.
94. Ayatollahi, M.R., S.M.J. Razavi, and M.Y. Yahya, *Mixed mode fatigue crack initiation and growth in a CT specimen repaired by stop*

- hole technique*. Engineering Fracture Mechanics, 2015. **145**: p. 115-127.
95. Huda, Z., N.I. Taib, and T. Zaharinie, *Characterization of 2024-T3: an aerospace aluminum alloy*. Materials Chemistry and Physics, 2009. **113**(2-3): p. 515-517.
96. Simensen, C. and G. Berg, *A survey of inclusions in aluminum*. Aluminium, 1980. **56**(5): p. 335-338.
97. Razaz, G. and T. Carlberg, *Casting Practices Influencing Inclusion Distributions in Billets*, in *Light Metals 2013*. 2016, Springer. p. 987-991.
98. Murakami, Y., *Metal fatigue: effects of small defects and nonmetallic inclusions*. 2002: Elsevier.
99. Frost, N., *Alternating stress required to propagate edge cracks in copper and nickel-chromium alloy steel plates*. Journal of Mechanical Engineering Science, 1963. **5**(1): p. 15-22.
100. Murakami, Y., T. Nomoto, and T. Ueda, *Factors influencing the mechanism of superlong fatigue failure in steels*. Fatigue & fracture of engineering materials & structures, 1999. **22**(7): p. 581-590.
101. Bathias, C., *There is no infinite fatigue life in metallic materials*. Fatigue and fracture of engineering materials and structures, 1999. **22**(7): p. 559-566.
102. Yang, Z., et al., *The fatigue behaviors of zero-inclusion and commercial 42CrMo steels in the super-long fatigue life regime*. Acta Materialia, 2004. **52**(18): p. 5235-5241.
103. Yang, Z., et al., *On the critical inclusion size of high strength steels under ultra-high cycle fatigue*. Materials Science and Engineering: A, 2006. **427**(1): p. 167-174.
104. Yang, Z., et al., *Estimation of the size of GBF area on fracture surface for high strength steels in very high cycle fatigue regime*. International Journal of Fatigue, 2008. **30**(6): p. 1016-1023.
105. Merati, A.J.I.J.o.F., *A study of nucleation and fatigue behavior of an aerospace aluminum alloy 2024-T3*. 2005. **27**(1): p. 33-44.
106. Talemi, R.H. and M.A.J.T.t. Wahab, *Finite element analysis of localized plasticity in Al 2024-T3 subjected to fretting fatigue*. Tribology transactions, 2012. **55**(6): p. 805-814.

107. Deng, Q., et al., *Numerical Modeling of the Effect of Randomly Distributed Inclusions on Fretting Fatigue-Induced Stress in Metals*. Metals, 2018. **8**(10): p. 836.
108. Majzoobi, G. and F.J.T.L. Abbasi, *On the effect of contact geometry on fretting fatigue life under cyclic contact loading*. Tribology Letters, 2017. **65**(4): p. 125.
109. Bhatti, N.A., K. Pereira, and M.A.J.T.I. Wahab, *Effect of stress gradient and quadrant averaging on fretting fatigue crack initiation angle and life*. Tribology International, 2019. **131**: p. 212-221.
110. Juoksukangas, J., A. Lehtovaara, and A. M?Ntyl?, *The effect of contact edge geometry on fretting fatigue behavior in complete contacts*. Wear, 2013. **308**(1-2): p. 206-212.
111. Navarro, C., S. Muñoz, and J.J.I.J.o.f. Dominguez, *On the use of multiaxial fatigue criteria for fretting fatigue life assessment*. International Journal of fatigue, 2008. **30**(1): p. 32-44.
112. Hojjati-Talemi, R., M.A. Wahab, and P.D. Baets, *Numerical investigation into the effect of contact geometry on fretting fatigue crack propagation lifetime*. Tribology Transactions, 2012. **55**(3): p. 365-375.
113. Hojjati-Talemi, R., et al., *Numerical estimation of fretting fatigue lifetime using damage and fracture mechanics*. Tribology Letters, 2013. **52**(1): p. 11-25.
114. Sabsabi, M., E. Giner, and F. Fuenmayor, *Experimental fatigue testing of a fretting complete contact and numerical life correlation using X-FEM*. International Journal of Fatigue, 2011. **33**(6): p. 811-822.
115. Lu, Y.-c., F.-p. Yang, and T. Chen, *Effect of single overload on fatigue crack growth in QSTE340TM steel and retardation model modification*. Engineering Fracture Mechanics, 2019. **212**: p. 81-94.
116. Albedah, A., et al., *Fractographic analysis of the overload effect on fatigue crack growth in 2024-T3 and 7075-T6 Al alloys*. International Journal of Minerals, Metallurgy and Materials, 2020. **27**(1): p. 83-90.
117. Lu, Y.-c., et al., *The retardation effect of combined application of stop-hole and overload on sheet steel*. International Journal of Fatigue, 2020. **132**: p. 105414.

118. Ghfiri, R., et al., *Fatigue life estimation after crack repair in 6005 A - T6 aluminium alloy using the cold expansion hole technique*. Fatigue & Fracture of Engineering Materials & Structures, 2000. **23**(11): p. 911-916.
119. Amrouche, A., et al., *Cold expansion effect on the initiation and the propagation of the fatigue crack*. International Journal of Fatigue, 2003. **25**(9-11): p. 949-954.
120. Su, M., et al., *Numerical study of double cold expansion of the hole at crack tip and the influence on the residual stresses field*. Computational materials science, 2008. **41**(3): p. 350-355.
121. Rana, M.S., C. Makabe, and G. Fujiwara, *The effect of hole shape on the extent of fatigue life improvement by cold expansions*. Engineering Failure Analysis, 2009. **16**(7): p. 2081-2090.
122. Růžek, R., J. Pavlas, and R. Doubrava, *Application of indentation as a retardation mechanism for fatigue crack growth*. International journal of fatigue, 2012. **37**: p. 92-99.
123. Razavi, S.M.J., et al., *Effects of different indentation methods on fatigue life extension of cracked specimens*. Fatigue & Fracture of Engineering Materials & Structures, 2018. **41**(2): p. 287-299.
124. Wu, H., et al., *On the prediction of the residual fatigue life of cracked structures repaired by the stop-hole method*. International Journal of Fatigue, 2010. **32**(4): p. 670-677.
125. Kim, W.B. *Effect of stop hole on stress intensity factor in crack propagation path*. in *AIP Conference Proceedings*. 2018. AIP Publishing LLC.
126. Song, P. and Y. Shieh, *Stop drilling procedure for fatigue life improvement*. International Journal of Fatigue, 2004. **26**(12): p. 1333-1339.
127. Hu, Y., et al., *Effects of stop hole on crack turning, residual fatigue life and crack tip stress field*. Journal of the Brazilian Society of Mechanical Sciences and Engineering, 2020. **42**(5).
128. Fanni, M., et al., *New crack stop hole shape using structural optimizing technique*. Ain Shams Engineering Journal, 2015. **6**(3): p. 987-999.

129. Arora, P.R., et al., *Experimental evaluation of fretting fatigue test apparatus*. International journal of fatigue, 2007. **29**(5): p. 941-952.
130. Majzoobi, G., et al., *A new device for fretting fatigue testing*. Transactions of the indian institute of metals, 2010. **63**(2-3): p. 493-497.
131. Lykins, C.D., S. Mall, and V.K. Jain, *Combined experimental–numerical investigation of fretting fatigue crack initiation*. International journal of fatigue, 2001. **23**(8): p. 703-711.
132. Tu, S.-T. and X.-C. Zhang, *Fatigue crack initiation mechanisms*. Reference Module in Materials Science and Materials Engineering, 2016: p. 1-23.
133. Lu, Y., et al., *Experimental and numerical study of the effects of porosity on fatigue crack initiation of HPDC magnesium AM60B alloy*. Journal of alloys and compounds, 2009. **470**(1-2): p. 202-213.
134. Yi, J., et al., *Scatter in fatigue life due to effects of porosity in cast A356-T6 aluminum-silicon alloys*. 2003. **34**(9): p. 1879.
135. Chan, L., et al., *Multiscale approach with RSM for stress–strain behaviour prediction of micro-void-considered metal alloy*. 2015. **83**: p. 129-137.
136. Digimat, A., *Software for the Linear and Nonlinear Multi-Scale Modeling of Heterogeneous Materials; e-Xstream Engineering: Louvain-la-Neuve*. 2011, Belgium.
137. Li, L., et al., *Strain localization and fatigue cracking behaviors of Cu bicrystal with an inclined twin boundary*. Acta materialia, 2014. **73**: p. 167-176.
138. Thompson, N., N. Wadsworth, and N. Louat, *Xi. The origin of fatigue fracture in copper*. Philosophical Magazine, 1956. **1**(2): p. 113-126.
139. Walvekar, A.A., et al., *An experimental study and fatigue damage model for fretting fatigue*. Tribology International, 2014. **79**: p. 183-196.
140. Vázquez, J., C. Navarro, and J. Domínguez, *Analysis of fretting fatigue initial crack path in Al7075-T651 using cylindrical contact*. Tribology International, 2017. **108**: p. 87-94.

141. Socie, D., *Critical plane approaches for multiaxial fatigue damage assessment*, in *Advances in multiaxial fatigue*. 1993, ASTM International.
142. Navarro, C., M. Garcia, and J. Dominguez, *A procedure for estimating the total life in fretting fatigue*. *Fatigue & Fracture of Engineering Materials & Structures*, 2003. **26**(5): p. 459-468.
143. Navarro, C., S. Muñoz, and J. Domínguez, *On the use of multiaxial fatigue criteria for fretting fatigue life assessment*. *International Journal of fatigue*, 2008. **30**(1): p. 32-44.
144. Navarro, C. and J. Domínguez, *Initiation criteria in fretting fatigue with spherical contact*. *International journal of fatigue*, 2004. **26**(12): p. 1253-1262.
145. El Haddad, M., et al., *J integral applications for short fatigue cracks at notches*. 1980. **16**(1): p. 15-30.
146. Bhatti, N.A. and M.A.J.T.I. Wahab, *A numerical investigation on critical plane orientation and initiation lifetimes in fretting fatigue under out of phase loading conditions*. *Tribology International*, 2017. **115**: p. 307-318.
147. Bhatti, N.A. and M.A.J.T.I. Wahab, *Fretting fatigue crack nucleation: A review*. *Tribology International*, 2018. **121**: p. 121-138.
148. Kumar, D., et al., *Fretting fatigue stress analysis in heterogeneous material using direct numerical simulations in solid mechanics*. *Tribology International*, 2017. **109**: p. 124-132.
149. Deng, Q., et al., *The effect of a critical micro-void defect on fretting fatigue crack initiation in heterogeneous material using a multiscale approach*. *Tribology International*, 2020. **141**: p. 105909.
150. Findley, W.N., *A Theory for the Effect of Mean Stress on Fatigue of Metals Under Combined Torsion and Axial Load or Bending*. *Journal of Engineering for Industry*, 1959. **81**(4): p. 301-305.
151. Fatemi, A., et al., *A critical plane approach to multiaxial fatigue damage including out - of - phase loading*. *Fatigue of Engineering Materials Ltd*, 1988. **11**(3): p. 149-165.
152. Socie, D., *Multiaxial Fatigue Damage Models*. *Journal of Engineering Materials and Technology*, 1987. **109**(4): p. 293-298.

153. Fatemi, A., et al., *Application of bi-linear log-log S-N model to strain-controlled fatigue data of aluminum alloys and its effect on life predictions*. 2005. **27**(9): p. 1040-1050.
154. Park, J. and D.J.I.J.o.F. Nelson, *Evaluation of an energy-based approach and a critical plane approach for predicting constant amplitude multiaxial fatigue life*. 2000. **22**(1): p. 23-39.
155. Bhatti, N.A. and M.A.J.T.I. Wahab, *A numerical investigation on critical plane orientation and initiation lifetimes in fretting fatigue under out of phase loading conditions*. 2017. **115**: p. 307-318.
156. SMITH, K.N., T.H. Topper, and P. Watson, *A Stress-strain Function for the Fatigue of Metals*. 1969: Defense Technical Information Center.
157. Socie, D.J.J.o.E.M. and Technology, *Multiaxial fatigue damage models*. 1987. **109**(4): p. 293-298.
158. Ruiz, C., P. Boddington, and K.J.E.m. Chen, *An investigation of fatigue and fretting in a dovetail joint*. *Experimental mechanics*, 1984. **24**(3): p. 208-217.
159. Luo, P., et al., *A notch critical plane approach of multiaxial fatigue life prediction for metallic notched specimens*. 2019. **42**(4): p. 854-870.
160. Bhatti, N.A., K. Pereira, and M.A.J.T.I. Wahab, *Effect of stress gradient and quadrant averaging on fretting fatigue crack initiation angle and life*. 2019. **131**: p. 212-221.
161. Taylor, D.J.I.J.o.F., *Geometrical effects in fatigue: a unifying theoretical model*. 1999. **21**(5): p. 413-420.
162. Taylor, D., *The theory of critical distances*. *Engineering Fracture Mechanics*, 2008. **75**(7): p. 1696-1705.
163. Susmel, L., *The theory of critical distances: a review of its applications in fatigue*. *Engineering Fracture Mechanics*, 2008. **75**(7): p. 1706-1724.
164. Forman, R., et al., *Fatigue crack growth database for damage tolerance analysis*. 2005.
165. Dini, D., D. Nowell, and I.N. Dyson, *The use of notch and short crack approaches to fretting fatigue threshold prediction: Theory and experimental validation*. *Tribology International*, 2006. **39**(10): p. 1158-1165.

166. Susmel, L. and D. Taylor, *A novel formulation of the theory of critical distances to estimate lifetime of notched components in the medium - cycle fatigue regime*. *Fatigue & Fracture of Engineering Materials & Structures*, 2010. **30**(7): p. 567-581.
167. Hattori, T., et al., *Fretting fatigue life estimations based on the critical distance stress theory*. 2011. **10**: p. 3134-3139.
168. Hattori, T., V.T. Kien, and M.J.T.I. Yamashita, *Fretting fatigue life estimations based on fretting mechanisms*. 2011. **44**(11): p. 1389-1393.
169. Araújo, J., et al., *On the use of the Theory of Critical Distances and the Modified Wöhler Curve Method to estimate fretting fatigue strength of cylindrical contacts*. 2007. **29**(1): p. 95-107.
170. Vázquez, J., C. Navarro, and J. Domínguez, *Analysis of fretting fatigue initial crack path in Al7075-T651 using cylindrical contact*. *Tribology International*, 2016: p. S0301679X16303310.
171. Araújo, J.A. and D. Nowell, *The effect of rapidly varying contact stress fields on fretting fatigue*. *International Journal of Fatigue*, 2002. **24**(7): p. 763-775.
172. Bhatti, N.A., K. Pereira, and M.A. Wahab, *Effect of stress gradient and averaging on fretting fatigue crack initiation angle and life*. *Tribology International*, 2018. **131**.
173. Taylor, D., P. Cornetti, and N. Pugno, *The fracture mechanics of finite crack extension*. *Engineering Fracture Mechanics*, 2005. **72**(7): p. 1021-1038.
174. Taylor, D., *Predicting the fracture strength of ceramic materials using the theory of critical distances*. *Engineering Fracture Mechanics*, 2004. **71**(16-17): p. 2407-2416.
175. Araújo, J.A., et al., *Life prediction in multiaxial high cycle fretting fatigue*. *International Journal of Fatigue*, 2020. **134**: p. 105504.
176. Giner, E., et al., *Direction of crack propagation in a complete contact fretting-fatigue problem*. *International Journal of Fatigue*, 2014. **58**: p. 172-180.
177. Hudson, C.M., *Effect of stress ratio on fatigue-crack growth in 7075-T6 and 2024-T3 aluminum-alloy specimens*. 1969: National Aeronautics and Space Administration.

178. Paris, P. and F. Erdogan, *A critical analysis of crack propagation laws*. 1963.
179. Xiang, Y., Z. Lu, and Y. Liu, *Crack growth-based fatigue life prediction using an equivalent initial flaw model. Part I: Uniaxial loading*. International Journal of Fatigue, 2010. **32**(2): p. 341-349.
180. Liu, L., *Modeling of mixed-mode fatigue crack propagation*. 2008.
181. Weertman, J., *Rate of growth of fatigue cracks calculated from the theory of infinitesimal dislocations distributed on a plane*. International Journal of Fracture Mechanics, 1966. **2**(2): p. 460-467.
182. Pook, L. *The Significance of Mode I Branch Cracks for Mixed Mode Fatigue Crack Growth Threshold Behaviour*. 2013.
183. Rozumek, D. and E. Macha, *A survey of failure criteria and parameters in mixed-mode fatigue crack growth*. Materials science, 2009. **45**(2): p. 190.
184. Erdogan, F. and G. Sih, *On the crack extension in plates under plane loading and transverse shear*. 1963.
185. Sih, G.C., *Strain-energy-density factor applied to mixed mode crack problems*. International Journal of fracture, 1974. **10**(3): p. 305-321.
186. Hussain, M., S. Pu, and J. Underwood. *Strain energy release rate for a crack under combined mode I and mode II*. in *Fracture analysis: Proceedings of the 1973 national symposium on fracture mechanics, part II*. 1974. ASTM International.
187. Chang, K.J., *On the maximum strain criterion—a new approach to the angled crack problem*. Engineering Fracture Mechanics, 1981. **14**(1): p. 107-124.
188. Cotterell, B. and J. Rice, *Slightly curved or kinked cracks*. International journal of fracture, 1980. **16**(2): p. 155-169.
189. Williams, M., *On the stress distribution at the base of a stationary crack. I. appl.* 1957, Mech.
190. Gdoutos, E.E., *Problems of mixed mode crack propagation*. Vol. 2. 2012: Springer Science & Business Media.
191. Yokobori Jr, A.T., et al., *Fatigue crack growth under mixed modes I and II*. Fatigue & Fracture of Engineering Materials & Structures, 1985. **8**(4): p. 315-325.

192. Mageed, A.A. and R. Pandey, *Studies on cyclic crack path and the mixed-mode crack closure behaviour in Al alloy*. International Journal of Fatigue, 1992. **14**(1): p. 21-29.
193. Lamacq, V., M. Dubourg, and L. Vincent, *Crack path prediction under fretting fatigue—a theoretical and experimental approach*. 1996.
194. Amestoy, M., H.D. BUI, and K.D. VAN, *Déviations infinitésimales d'une fissure dans une direction arbitraire*. 1979.
195. Ribeaucourt, R., M.-C. Baidetto-Dubourg, and A. Gravouil, *A new fatigue frictional contact crack propagation model with the coupled X-FEM/LATIN method*. Computer Methods in Applied Mechanics and Engineering, 2007. **196**(33-34): p. 3230-3247.
196. Dubourg, M. and V. Lamacq, *A predictive rolling contact fatigue crack growth model: onset of branching, direction, and growth—role of dry and lubricated conditions on crack patterns*. J. Trib., 2002. **124**(4): p. 680-688.
197. Zhang, M., D. McDowell, and R. Neu, *Microstructure sensitivity of fretting fatigue based on computational crystal plasticity*. Tribology International, 2009. **42**(9): p. 1286-1296.
198. Mall, S., S. Namjoshi, and W. Porter, *Effects of microstructure on fretting fatigue crack initiation behavior of Ti-6Al-4V*. Materials Science and Engineering: A, 2004. **383**(2): p. 334-340.
199. Hojjati-Talemi, R. and M.A. Wahab, *Fretting fatigue crack initiation lifetime predictor tool: Using damage mechanics approach*. Tribology International, 2013. **60**: p. 176-186.
200. Shedbale, A.S., I.V. Singh, and B.K. Mishra, *Heterogeneous and homogenized models for predicting the indentation response of particle reinforced metal matrix composites*. International Journal of Mechanics & Materials in Design, 2017. **13**(4): p. 531-552.
201. Mirkhalaf, S.M., R. Simoes, and R. Simoes, *Determination of the size of the Representative Volume Element (RVE) for the simulation of heterogeneous polymers at finite strains*. Finite Elements in Analysis & Design, 2016. **119**(C): p. 30-44.
202. Heinrich, C., et al., *The influence of the representative volume element (RVE) size on the homogenized response of cured fiber composites*.

- Modelling & Simulation in Materials Science & Engineering, 2012. **20**(7): p. 75007-75031(25).
203. Yu, Y., et al., *Stress transfer analysis of unidirectional composites with randomly distributed fibers using finite element method*. Composites Part B, 2015. **69**: p. 278-285.
204. Liu, Z.R., et al., *The structure and the properties of S-phase in AlCuMg alloys*. Acta Materialia, 2011. **59**(19): p. 7396-7405.
205. Prasannavenkatesan, R., et al., *Simulated extreme value fatigue sensitivity to inclusions and pores in martensitic gear steels*. Engineering Fracture Mechanics, 2011. **78**(6): p. 1140-1155.
206. Hashimoto, T., et al., *Investigation of dealloying of S phase (Al 2 CuMg) in AA 2024-T3 aluminium alloy using high resolution 2D and 3D electron imaging*. Corrosion Science, 2016. **103**: p. 157-164.
207. Qiu, Y. and G. Weng, *The influence of inclusion shape on the overall elastoplastic behavior of a two-phase isotropic composite*. International Journal of Solids and Structures, 1991. **27**(12): p. 1537-1550.
208. Cho, J., M. Joshi, and C. Sun, *Effect of inclusion size on mechanical properties of polymeric composites with micro and nano particles*. Composites Science and Technology, 2006. **66**(13): p. 1941-1952.
209. Hibbett, K. and Sorensen, *ABAQUS/Standard: User's Manual*. 1997: Hibbett, Karlsson & Sorensen.
210. Lykins, C.D., *An investigation of fretting fatigue crack initiation behavior of the titanium alloy Ti-6Al-4V*. 1999.
211. Iyer, K. and S. Mall, *Analyses of contact pressure and stress amplitude effects on fretting fatigue life*. Journal of engineering materials and technology, 2001. **123**(1): p. 85-93.
212. Lu, Y., et al., *Experimental and numerical study of the effects of porosity on fatigue crack initiation of HPDC magnesium AM60B alloy*. Journal of Alloys & Compounds, 2009. **470**(1): p. 202-213.
213. Liu, Z., et al., *The structure and the properties of S-phase in AlCuMg alloys*. 2011. **59**(19): p. 7396-7405.
214. Prasannavenkatesan, R., et al., *Simulated extreme value fatigue sensitivity to inclusions and pores in martensitic gear steels*. 2011. **78**(6): p. 1140-1155.

215. Lu, Y., et al., *Experimental and numerical study of the effects of porosity on fatigue crack initiation of HPDC magnesium AM60B alloy*. 2009. **470**(1-2): p. 202-213.
216. Gall, K., et al., *On the driving force for fatigue crack formation from inclusions and voids in a cast A356 aluminum alloy*. 2001. **108**(3): p. 207-233.
217. Xu, Z., et al., *Effects of pore position in depth on stress/strain concentration and fatigue crack initiation*. 2012. **43**(8): p. 2763-2770.
218. Huda, Z., et al., *Characterization of 2024-T3: an aerospace aluminum alloy*. 2009. **113**(2-3): p. 515-517.
219. Li, P., *Through process modelling of aluminium alloy castings to predict fatigue performance*. 2007.
220. Yang, Z., et al., *On the critical inclusion size of high strength steels under ultra-high cycle fatigue*. 2006. **427**(1-2): p. 167-174.
221. Murakami, Y.J.J.i.j.S., Solid mechanics, strength of materials, *Effects of small defects and nonmetallic inclusions on the fatigue strength of metals*. 1989. **32**(2): p. 167-180.
222. Hibbett, Karlsson, and Sorensen, *ABAQUS/standard: User's Manual*. Vol. 1. 1998: Hibbett, Karlsson & Sorensen.
223. Pereira, K., N. Bhatti, and M.A.J.T.I. Wahab, *Prediction of fretting fatigue crack initiation location and direction using cohesive zone model*. 2018. **127**: p. 245-254.
224. Lykins, C.D., S. Mall, and V.K.J.I.j.o.f. Jain, *Combined experimental–numerical investigation of fretting fatigue crack initiation*. 2001. **23**(8): p. 703-711.
225. Proudhon, H., S. Fouvry, and J.-Y.J.I.J.o.f. Buffière, *A fretting crack initiation prediction taking into account the surface roughness and the crack nucleation process volume*. 2005. **27**(5): p. 569-579.
226. Almajali, M., *Effects of Phase Difference Between Axial and Contact loads on Fretting Fatigue Behavior of Titanium Alloy*. 2006, AIR FORCE INST OF TECH WRIGHT-PATTERSON AFB OH SCHOOL OF ENGINEERING AND ....
227. Szolwinski, M.P. and T.N.J.W. Farris, *Observation, analysis and prediction of fretting fatigue in 2024-T351 aluminum alloy*. 1998. **221**(1): p. 24-36.

228. Pereira, K. and M.A.J.T.I. Wahab, *Fretting fatigue crack propagation lifetime prediction in cylindrical contact using an extended MTS criterion for non-proportional loading*. 2017. **115**: p. 525-534.
229. Araujo, J. and D.J.I.J.o.F. Nowell, *The effect of rapidly varying contact stress fields on fretting fatigue*. 2002. **24**(7): p. 763-775.
230. Moghaddam, S.M., et al., *A damage mechanics approach to simulate butterfly wing formation around nonmetallic inclusions*. 2015. **137**(1): p. 011404.
231. Hojjati-Talemi, R., et al., *Prediction of fretting fatigue crack initiation and propagation lifetime for cylindrical contact configuration*. Tribology International, 2014. **76**: p. 73-91.
232. Pereira, K., N. Bhatti, and M.A.J.T.I. Wahab, *Prediction of fretting fatigue crack initiation location and direction using cohesive zone model*. Tribology International, 2018. **127**: p. 245-254.
233. Araujo, J. and D.J.I.J.o.F. Nowell, *The effect of rapidly varying contact stress fields on fretting fatigue*. International Journal of Fatigue, 2002. **24**(7): p. 763-775.
234. Vingsbo, O. and S.J.W. Söderberg, *On fretting maps*. Wear, 1988. **126**(2): p. 131-147.



Structure and fatigue.